universität wien

DIPLOMARBEIT / DIPLOMA THESIS

Titel der Diplomarbeit / Title of the Diploma Thesis

"Combining antibiotic loaded nanocarriers with golden nanoparticles for light-triggered release and biofilm disruption“

verfasst von / submitted by

Julia Anna Maria Kaufmann

angestrebter akademischer Grad / in partial fulfilment of the requirements for the degree of

Magistra der Pharmazie (Mag.pharm.)

Wien, 2017 / Vienna, 2017

Studienkennzahl lt. Studienblatt /degree programme code as it appears on the student record sheet:	A 449
Studienrichtung lt. Studienblatt /degree programme as it appears on the student record sheet:	Diplomstudium Pharmazie
Betreut von / Supervisor:	Ao. Univ.-Prof. Mag. Dr. Franz Gabor

Acknowledgement

First of all, I would like to thank my supervisor in Vienna, Ao. Univ.-Prof. Mag. Dr. Franz Gabor, who gave me this great opportunity to write my diploma thesis abroad.

Furthermore, I would like to send a huge ‘dank u wel’ to my supervisors at the University of Ghent, Prof. Dr. Kevin Braeckmans and Prof. Dr. Stefaan De Smedt, together with everyone from the ‘Laboratory of General Biochemistry and Physical Pharmacy’.

My deepest gratitude goes to my daily supervisor Apr. Eline Teirlinck, who not only introduced me into the most interesting field of vapour nanobubbles but also answered all my numerous questions. Thanks for making the daily routine in the lab an experience I won’t forget.

I would like to say ‘dank je wel’ not only to all my lab colleagues (‘stockroom crew’), who made Ghent to one of the best experiences of my life, but also to my colleagues in Vienna, who always supported me.

Some very special thanks go to my family, my boyfriend and my friends, who always believed in me and encouraged me to never give up.

My deepest gratitude goes to my mother Margarete, who was always there for me. Without her I wouldn’t be where I am today. Danke Mama.

Thank you all so much!

Table of contents

1 Introduction

Antibiotic drug resistance is an emerging problem in modern society. One of the reasons for antibiotic failure is the fact that bacteria often organize themselves in biofilms, a conglomeration of bacteria surrounded by a protecting polymer matrix. Different mechanisms account for the increased survival of biofilm infections, and one major factor is a reduced antibiotic drug penetration throughout the thick clusters of biofilms. The limited diffusion through biofilms can be attributed to 2 reasons: (1) formation of thick cell clusters of several µms in size and (2) physicochemical interactions between the antimicrobial drug and matrix components. To overcome these issues, liposomes that incorporate antibiotics are often used and therefore help reducing these physicochemical interactions. However, the release of the drug near the target bacterial cells remains uncontrollable without any modification.

The main aim of this diploma thesis was to investigate the use of so-called vapour nanobubbles to highly-controllably trigger antibiotic drug release out of liposomes and subsequently enhance bacteria's susceptibility towards antibiotics. In this diploma thesis, the following parameters related to VNB formation are evaluated: calcein encapsulation efficiency inside differently charged liposomes, functionalization of liposomes with golden nanoparticles as light-sensitive particles, laser pulse energy threshold and liposomal release of compounds. A second objective was to determine how these liposomes penetrate biofilms, hence determine the liposomal location inside biofilms via advanced microscopy methods.

Since surface charge is a crucial parameter for physicochemical interactions, we tested differently charged liposomes in terms of their location inside a biofilm. Next, we prepared calcein-loaded liposomes and triggered the release of a self-quenching fluorophore via VNBs. In a further experiment, we investigated the release of an antibiotic encapsulated in liposomes.

2 Einleitung

Steigende Antibiotikaresistenz und somit vermehrte Therapiefehlschläge stellen unsere Gesellschaft vor eine schwierige Herausforderung. Häufig sind Biofilme am Versagen der Antibiotikatherapie beteiligt. Biofilme, eine Konglomeration von Bakterien, umgeben von einer schützenden, selbstproduzierten Polymermatrix, weisen verschiedene Resistenzmechanismen auf, die für das Überleben von Biofilmbakterien verantwortlich sind. Einer der Resistenzmechanismen ist dabei eine reduzierte Penetration in dichte Bakteriencluster. Die limitierte Diffusion durch den Biofilm ist einerseits bedingt durch die mehreren µm dicken Zellcluster und andererseits durch die physikochemischen Interaktionen zwischen Antibiotikum und Matrixkomponente. Aus diesem Grund werden häufig Liposomen eingesetzt, die das Antibiotikum im Inneren gespeichert halten und somit die physikochemischen Interaktionen reduzieren. Trotzdem bleibt die Freisetzung nahe den bakteriellen Zellen ohne jegliche Modifikation unkontrollierbar.

Das Hauptziel meiner Diplomarbeit ist es, sogenannte Nanodampfblasen als Auslöser für gezielte Antibiotikafreisetzung aus Liposomen zu verwenden und somit die Empfindlichkeit von Bakterien gegenüber Antibiotika zu erhöhen. Folgende Parameter, die in Zusammenhang mit Dampfnanoblasenbildung stehen, werden in der Arbeit untersucht: Effizienz der Calceinbeladung in verschieden geladenen Liposomen, Funktionalisierung von Liposomen mit Goldnanopartikel als licht-sensitive Partikel, Schwellenwert der Laserenergie, die zur Dampfnanoblasenformation benötigt wird und die Freisetzung der liposomalen Beladung. Ein weiteres Ziel ist es, die Liposomen hinsichtlich ihrer Penetration und ihrer Lage innerhalb des Biofilms mit Hilfe von fortgeschrittener Mikroskopiertechnik zu untersuchen.

Da Oberflächenladung ein kritischer Parameter für physikochemische Interaktionen ist, werden verschieden geladene Liposomen im Biofilm untersucht. Des Weiteren werden Calcein beladene Liposomen hergestellt und die Freisetzung des Fluorophores mit Dampfnanoblasen gesteuert. In einem weiteren Experiment wird die Freisetzung von Antibiotika aus Liposomen untersucht.

3 Background

3.1 Nanoparticles and drug delivery

It is estimated that 95 % of newly found drugs have insufficient effects due to their pharmacokinetics.[1] Major problems of new therapeutics concerning the difficulty in reaching their target throughout the human body are the reason for the decrease of the approval of big breakthrough drugs as there is an emerging gap between the discovery of drugs and their delivery.[2] Another major problem are side effects such as nausea or allergic reactions that are often caused by non-specific distribution inside the body. One approach might be to use drug targeting mediated via highly-controllable nanoparticles.[3]

The idea of drug targeting is not new. About 100 years ago, the concept of a so-called “magic bullet” that delivered drugs directly to the target was introduced by Paul Ehrlich.[4] Nowadays, numerous studies are conducted to nanocarrier design and characterization, as they can improve the delivery of various agents into the body due to their favourable high surface to mass ratio, as well as the ability to carry both hydrophobic and hydrophilic drug compounds.[5] By this means, it has been shown that it is possible to increase the amount of drug delivered to the target, while simultaneously avoiding side effects off target. With drug targeting it is also possible to reduce the dosage as the drug is directly delivered to the target cell.[6] A number of nanoformulations are found to be successful in the aforementioned aims and have been introduced in the pharmaceutical market, such as Griseofulvin[7], Doxorubicin (Doxil®)[8] and Paclitaxel[9,10].

Nanocarriers can be composed of different compounds such as lipids, polymers, silica, or metals. This broad availability of possible key stones translates in numerous types of nanoparticles such as liposomes, nano-emulsions[11], drug-polymer-conjugates[12], drug-antibody conjugates[13], quantum dots[14], dendrimers[15] or nano-goldshells[16]. Several key points like a good biocompatibility, stability in target environment, high loading capacity for both therapeutic and diagnostic molecules and low toxicity are important when evaluating nanocarriers.[17] Characteristics of nanoparticles like size and shape are very important, as they influence the drug delivery property. Nanoformulations generally have a size between 10 and 1000 nm.[18] Nanoparticles with sizes below 1 nm can pass the blood-brain-barrier. 200 nm is the size limit for biofilm penetration[19], whereas 40-60 nm sized nanoparticles are able to quit fenestrated capillaries in liver, spleen, intestines and newly built capillaries as found in tumors.[20] This is a good example of how the nanoparticle can be designed in order to reach a certain intended tissue by tuning its size. But also the shape impacts the effect as rods or worms outperform spherical nanoparticles.[21] Nanoparticles in tumour sites seize the enhanced permeation and retention (EPR)-effect as new capillaries are more

permeable and lymphatic systems are not perfected yet.[22] However, the EPR-effect has lately been the subject of many debates as the studies that claimed EPR-effects in tumour sites were only performed in animals, and no proof can be given that this is also translatable to human settings[23–25].

Although nanoparticle encapsulation can offer a lot of benefits, one should carefully select the correct type of nanoparticle for the intended application in order to obtain an ideal carrier in clinical settings. Hereby, toxicity of the nanoparticle itself, and stability in biological tissue are two important characteristics to keep in mind.

Besides the advantages of nanoparticles, it is difficult to approve them via a central agency as toxicity, detection and stability of some nanoparticles remain a challenge.[6] It is difficult to trace nanoparticles inside the human body, as they can be taken up by several organs. Furthermore, nanoparticles tend to self-aggregate, which leads to instability of a therapeutic system.[26] A possible way to circumvent this problem is to modify the surfaces of nanoparticles with polyethylene glycol (PEG) chains. PEGylation can prolong their presence in the human circulation due to the inhibition of recognition and phagocytosis by the mononuclear phagocytic system. A lot of research is also conducted about the protein corona, which is formed around nanoparticles in biological tissues.[27] The protein corona consists of proteins in numerous types, conformations and amounts, which influence the fate of the nanoparticle in a biological system. Therefore it is important to characterize it well.[27]

3.2 Liposomes

Bangham et al[28] discovered the liposomes in the 1960s. Since then, it has become a promising platform of drug delivery. In the 1970s, liposomes were first used as a drug delivery carrier.[29]

Liposomes are spherical vesicles composed of phospholipids as depicted in *Figure 1*.[30] One of their advantages is their easy fabrication process as they are formed instantly by self-assembly of phospholipids. As the lipid film swells, several bilayers are formed.[31] Liposomes can be separated into different groups, determined by size, surface charge, composing groups and lamellarity.[32] There are for instance small unilamellar vesicles (SUV) with a size around 100 nm, large unilamellar vesicles (LUV) with a size between 200 and 800 nm or large multilamellar vesicles (LMV) with a size range of 500 to 5000 nm.[30,33] The liposomal surface charge depends on the composition of the lipids, it can be positively, negatively or neutrally charged.[33] The rigidity of the liposomal bilayer can be influenced by inclusion of non-toxic lipids like cholesterol due to their planar structure.[33] Cholesterol is often added as a stabilizer as permeability for electrolyte and non-electrolyte solvents is reduced, packing of phospholipid molecules is increased and fluidity inside liposomal bilayer is changed in terms of an improved rigidity.[34]

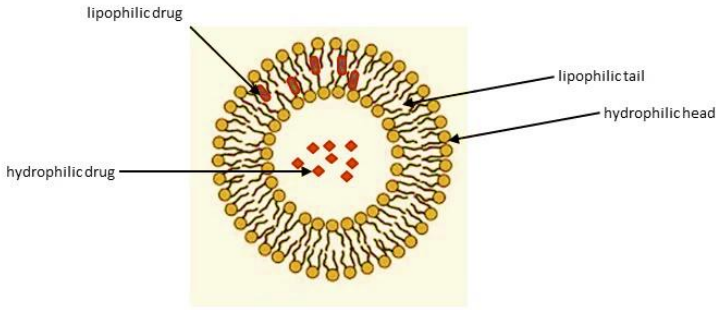

Figure 1: Scheme of a liposome formed by phospholipids in an aqueous medium

Liposomes are a popular means of drug targeting as they can entrap both water-soluble drugs in their aqueous core as well as hydrophobic drugs in their membrane.[30] By entrapping hydrophobic and hydrophilic drugs, initially poor pharmacokinetics of drugs can be improved.[2,35] Furthermore, liposomes, as small and flexible nanoparticles, have been extensively studied in the past few years and already successfully brought into clinical use.[8] Due to their similar phospholipid composition, as in biological membranes, they are highly biocompatible.

However, intravenously administered liposomes have to face multiple biological barriers that can decrease the accumulation at the target site and therefore limit their effect.[36] First of all, the mere interaction with proteins of the blood, a phospholipid bilayer, serum components[37] or biological cell walls[38] can destabilize the formulation. The Reticulo-Endothelial-System (RES-System)[6], opsonisation, high pressure inside tumors, being trapped inside a lysosome or drug efflux pumps that reduce the drug concentration inside the cell are other typical biological barriers.

To protect liposomes from being captured by the RES, it is possible to cover the hydrophilic heads of the lipids with polyethylene glycol (PEG)-chains, as they shield the surface of the liposomes and offer steric hindrance. They can also reduce the recognition via opsonine[20] or target specific cells[2].

Liposomes can be taken up by cells via endocytosis, adsorption or fusion.[2,39] Endocytosis is accomplished via endosomal uptake[2], however in most cases the drug needs to be released again to exert its effect. Adsorbing liposomes associate with the cell wall without damaging their own lipid bilayer[2]. Liposomal fusion with the cell wall yields a drug release in the cytoplasm.

As already mentioned, once the nanoparticles reach their intended target site, they should release their cargo in order to obtain a therapeutic response. Release can be guaranteed by trans-bilayer diffusion or pore formation.[2] In comparison to trans-bilayer diffusion, which describes the diffusion of a drug through the intact bilayer without any carrier[40], pore formation can be caused by bilayer disruption or phase separation.[2] Phase separation is dependent on the phase transition temperature of each lipid. Below their phase transition temperature lipids are rigid and gel-like.[41] Above phase

transition temperature however lipids melt and are in a fluid phase.[41] The temperature at which phase transition occurs can be manipulated by the selection of different lipids and the inclusion of cholesterol. It is often added to a formulation to reduce the fluidity of the bilayer above the phase transition temperature.[2,33]

An interesting feature of liposomes is their ability to carry other nanoparticles as shown in *Figure 2*. Nanoparticles can either be entrapped in the aqueous core, installed in the phosphobilayer or conjugated to the surface employing electrostatic interactions or covalent binding.[2]

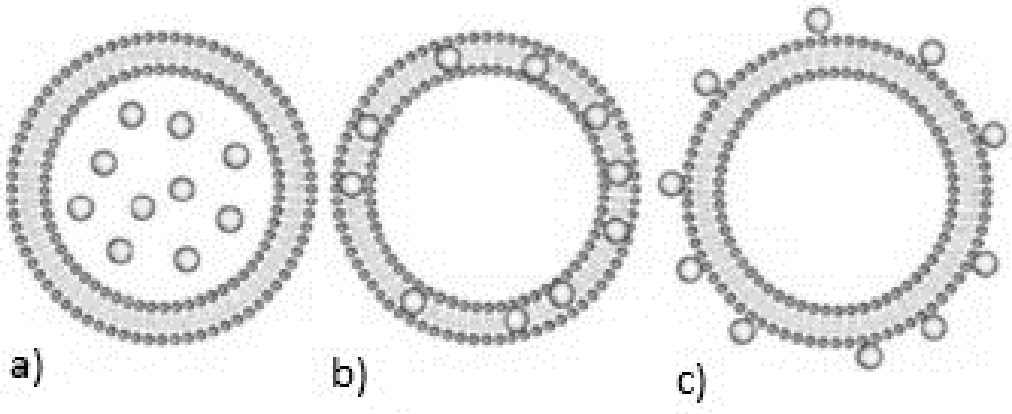

Figure 2: Scheme of drugs incorporated in liposomes: a) hydrophilic drugs are incorporated inside the aqueous core, b) drugs are installed in the liposomal bilayer or c) the surface of liposomes is decorated with other nanoparticles[42]

Entrapping molecules inside the phosphobilayer is challenging, as it is only few nm thick in average.[2] So-called liposome-nanoparticle-assemblies (LNA)[2] can be of use in the exciting emerging field of theranostics, where therapeutic agents are combined with diagnostic markers in a single particle treatment.

3.3 Liposomal delivery on demand: triggered release

3.3.1 Triggering mechanism

When reaching the intended target tissue, the drug still needs to be released in order to be effective. A great challenge for scientists is to find a right balance between the protection of the incorporated drug and the release of it at the target site.[17] To address this problem, remotely triggerable drug systems are designed, that aim to control drug delivery in terms of time, duration and location.[43]

Nanoparticles can be composed of biodegradable compounds or materials only that break down upon a trigger. Numerous mechanisms are found to be able to break down nanoparticle materials, and one can differentiate between external and internal triggers. External triggers are for example light, heat, ultrasound or magnetic fields, whereas low endosomal pH, enzymes or redox-potentials are classified as internal

triggers.[38] Systems with magnetic particles can be triggered via magnetic forces[6,44], whereas ultrasound can generate microbubbles[45]. Light-responsive systems can be triggered by light of different wavelengths depending on the composition.[46] When golden nanoparticles or polyNIPAM (poly-N-isopropylacrylamide) is included in the liposome formulation, triggering can occur via NEAR IR-light (650-900 nm). It has also been reported that UV/vis light can be used for photo-cleavage or photoisomerization.[46]

3.3.2 Light-triggered liposomal release

Light-responsive liposomes have been the focus of many research groups for more than 30 years.[38] Photoactivation can be easily used to trigger drug release as it has many adjustable parameters like wavelength, intensity or duration.[47]

In many cases, a photo-responsive element, which can be organic or inorganic, is introduced into the liposome. Potential sites are the fatty acid chain, the hydrophilic head or the glycerol backbone.[5] The photo-responsive element leads to drug release mediated via photo-oxidation, cis-trans isomerisation, photo-cleavage or photopolymerization.[47] Photo-oxidation is ensured via vinyl ether linkages in the molecules that can absorb IR- light hence lead to leakage.[47] Cis-trans isomerisation induced by azobenzen is reversible whereas photo-cleavage remains irreversible. Both methods use membrane perturbations mechanisms.[5] Intermolecular crosslinking substances like bis-sorbyl phosphatidylcholine (bisSorbBPC) and 1,2-bis(tricosa-10,12-diynoyl-sn-glycero-3-phosphocholine (DC8,9,PC) lead to photopolymerization.[5]

Generally, one can distinguish between photodynamic and photothermal effects. Photodynamic effects rely on the production of reactive oxygen species (ROS).[48] Photothermal effects however depend on photothermal-responsive elements, whose electrons get excited, generate heat and relax through non-radiative decay.[49]

An important bottleneck of photo-activated liposomes in an *in vivo* setting is the insufficient radiation of liposomes in biological tissues. This can be due to the fact that the human body embodies many barriers for efficient radiation penetration. Wavelengths below 700 nm are absorbed by tissue chromophores such as haemoglobin or melanin which yields a low penetration.[50] Water prevents wavelengths above 900 nm to penetrate.[51] Many interesting molecules are triggerable via UV light (200-400 nm), but most promising in tissue is Infrared light (700-2500 nm), as it reaches up to 1 cm depth in human tissue.[52]

A possible solution for this problem is the functionalization of the drug delivery system with golden nanoparticles (Au-NPs). Golden nanoparticles, having generally a size range between 10 and 100 nm[53], show several unique features such as inertness, biocompatibility, tunable size and surface modification.[54] Another advantage is their

easy synthesis and their flexibility as they can be designed with numerous sizes and shapes. The most important feature of golden nanoparticles are their optical properties hence their surface plasmon effect. When a metal nanoparticle is irradiated with light, the electromagnetic field induces the free electrons of the metal to oscillate.[55] Due to the oscillation of the particles performing a charge separation, a dipole oscillation in the direction of the electromagnetic field is formed.[55] Its maximum amplitude is called surface plasmon resonance, which occurs when the frequency of incoming photons goes along with the resonant oscillation frequency of surface electrons.[49,56] SPR bands of gold nanoparticles scatter and absorb electromagnetic waves strongly resulting in local heat hence a conversion from light to heat in picoseconds.[53,57]

By functionalizing liposomes with golden nanoparticles, one can not only exploit the unique plasmonic properties of Au-NPs efficiently absorbing light energy but also use drug targeting via liposomes resulting in a highly-controllable, triggerable system due to their capability of absorbing light of different wavelengths. Nanorods e.g., absorb efficiently near infrared light[58], which is a promising trigger in biological tissues as explained earlier.

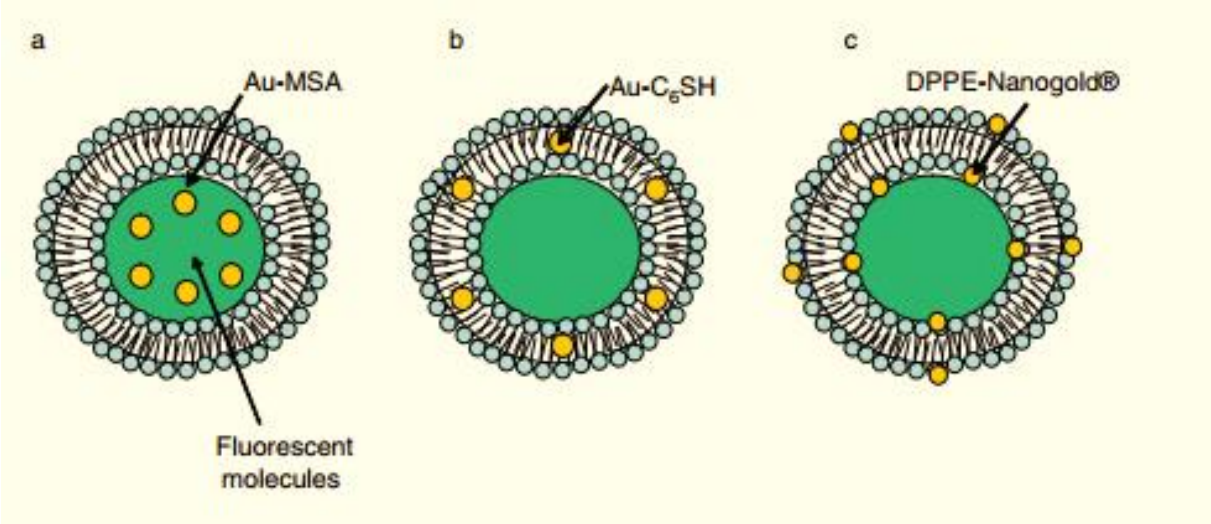

Figure 3: Liposomes functionalized with different golden nanoparticles: a) Au-MSA is encapsulated in the aqueous core, b) Au-C6-SH is embedded in the liposomal bilayer and c) DPPE-Nanogold is included in the liposomal construct [47]

Liposomes can be functionalized with golden nanoparticles in several ways as depicted in *Figure 3***.** Paasonen et al.[59] investigated encapsulation of hydrophilic mercaptosuccinic acid-coated gold nanoparticles (Au-MSA) in the core of liposomes as well as embedding of hydrophobic hexanethiol-coated gold nanoparticles (Au-C6SH) in the liposomal bilayer. Chithrani et al.[60] investigated DPPE-Nanogold®, a 1,4 nm Au-nanoparticle attached to a dipalmitoyl-phosphatidyl-ethanolamine molecule, embedded in the liposomal bilayer. Kojima et al.[42] examined golden nanoparticles that were attached non-covalently to a liposomal surface. This functionalization is

dependent on electrostatic interactions between the golden nanoparticles and the liposomal lipids.

Paasonen et al.[61] proved for the first time that it is possible to release calcein of neutrally charged liposomes functionalized with golden NPs (Au-MSA, Au-C6SH and DPPE-Nanogold®, shown in *Figure 3*) once irradiated with light. The authors suggest that the release is mediated via phase separation, which can be ameliorated with golden nanoparticles that are covalently conjugated to a lipid, as heat can then be conducted more efficiently towards the liposomal bilayer.

3.3.2.1 *Vapour Nanobubbles*

Recently, it has been discovered by Lapotko et al.[62] that pulsed laser irradiation of plasmonic nanoparticles can generate so-called “vapour nanobubbles”, shown in *Figure 4.*

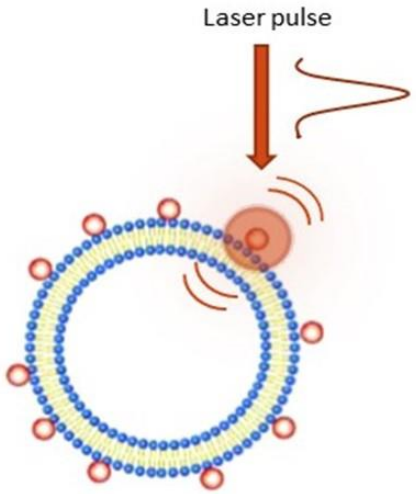

Figure 4: Scheme of the generation of a vapour nanobubble (VNB)

Irradiation by short laser pulses increases the temperature of plasmonic nanoparticles up to several hundred degrees[46] in 1 picosecond due to their unique optical property.[63] As discussed earlier, plasmonic nanoparticles can efficiently convert light energy into heat via the SPR effect. An increased temperature of the golden nanoparticle causes surrounding medium to heat up and thus to vaporise.[62] A thin vapour layer is built around the nanoparticle forming a nucleus. Having enough input of energy to overcome surface tension and viscosity, a bubble expands until reaching its maximal diameter. The bubble expansion hence vaporization is followed by shockwaves and acoustic waves as the bubble collapses violently.[62] The local high-pressure shockwave can lead to local damage.

VNBs only occur when irradiated with short (ns) laser pulses of sufficient high energy because the thermal field is localized around the Au-NP. By creating a bubble, the thermal and mechanical field is kept around the nanoparticle controlled by the bubble lifetime (5-500 ns) and its diameter (50-1000 nm) that in turn are dependent on the

laser pulse duration[64] as well as the thermal energy that is converted from optical energy rendering them highly controllable in time and space. Due to their high optical scattering, nanosized bubbles are detectable optically. The acoustical detection method of bubbles remains unfavourable due to poor spatial and temporal resolution[65].

Long or continuous laser irradiation show no VNBs due to thermal diffusion as the thermal field spreads over a large area. Ultra-short pulses induce the thermal field inside the nanoparticles, leading to shock waves that spread likewise over a large area. This makes both methods unfavourable as the distribution of the thermal and the mechanical field over a large area always includes damage to non-target cells leading to increased cytotoxicity, decreased cell viability and off target drug delivery.

VNBs as a newly discovered phenomenon have lately been tested in a variety of biomedical and biophysical applications.[66–68]

Efficient disruption of liposomes releasing quickly their contents[66] on the one hand and cell-specific intracellular delivery[69] on the other hand was established via VNBs. Those small, highly tunable and localized VNBs have been evoked by a single laser pulse irradiation without killing cells. Xiong et al[67] compared VNBs with thermal treatment in order to deliver agents intracellularly. VNBs were found to be more favourable than heating as they reduce non-specific cell-toxicity and enhance cell viability. It was also proven that it is possible to tune the pore sizes[67] by changing the laser fluence. In this way, the amount and the size of delivered macromolecules could be monitored.

Also in the field of cancer research, investigations have been conducted towards the use of VNBs. One major problem of drug targeting remains the difficulty of releasing drugs from the endosomes, leading to an insufficient concentration of chemotherapeutics in the cytosol. VNBs are found to facilitate the endosomal escape by disrupting the endosomal membrane, rendering a high therapeutic efficacy and a low non-specific toxicity compared to non-targeted chemotherapy.[70]

Another field of research investigates VNBs as in their potential as theranostics[71,72] , which combines diagnostic and therapeutic features. VNBs can detect cancer cells while providing a local high concentration of the cytostatics.[68] That, in turn, ameliorates on the one hand the precision and the rapidity of the treatment and reduces on the other hand non-specific toxicity, which has been proven in vitro and in vivo.[73]

Not only noble metals but also other particles such as hemozoin show VNB formation when irradiated with a high energy laser. Malaria blood parasites digest haemoglobin resulting in the formation of a nanoparticle called hemozoin. Due to its small size and its high optical absorbance, short laser pulses with high energy can generate vapour nanobubbles around the hemozoin molecules, that can be detected acoustically. This in turn provides a fast, safe and transdermal hence non-invasive way to detect malaria-

specific hemozoin rendering a promising, high-throughput diagnostic method to detect malaria.

3.4 Use of liposomes in biofilm-related infections

3.4.1 Antibiotic multidrug resistance

One of the most important developments of the 20th century was the antibiotic therapy. Back then acute bacterial infections were the reason for many people to suffer or to die. Ameliorations concerning the hygiene, vaccines and the antibiotic therapy had a great impact on modern medicine.[74] However, pathogens have also evolved over time in terms of surviving antibiotic treatment.[75] Nowadays, physicians have to face antibiotic-resistant strains of bacteria and chronic infections that are difficult to eradicate[76], which results not only in limitations for patients with severe infections, but also in an enormous economic burden for the health system.[77]

Due to over- and misuse of antibiotics, the number of antibiotic-resistant bacteria seems on the rise in the past few years.[78] Microorganisms have developed several mechanisms[79] to survive different classes of antibiotic agents. Firstly, resistance can be caused by mutations.[80] Bacteria have the ability to either inherit genes or to transfer them via plasmids to each other, which is called a horizontal gene transfer.[80] Secondly, bacteria can produce enzymes as a response to the presence of antibiotics that can break down these antibiotics, e.g. β-lactam antibiotics that are degraded by beta-lactamases. Moreover, channels in the bacterial cell wall can be closed, which results in a cell wall that is no longer permeable. Furthermore, some bacteria can upregulate efflux pumps responsible of clearing antibiotics, leading to extrusion of antibiotics out of the cell.

3.4.2 Biofilm-related resistance

Bacteria can grow in a planktonic and a sessile mode.[81,82] Planktonic bacteria are free floating, whereas sessile bacteria are bacteria embedded in a so-called biofilm. A biofilm is a consortia of bacteria enclosed in a self-produced extracellular polymer matrix containing polysaccharides, peptides, proteins, DNAs etc.[83] Bacteria within a biofilm build clusters and work together as a group.[84]

Biofilms or bacterial aggregates evolved over hundreds of years. Protecting themselves against natural antibiotics, they have first been observed by Anthony van Leeuwenhoek (1632-1723).[85] Arthur T. Henrici described these aggregates in 1933 as water organisms that grow on surfaces instead of floating freely around.[86] The term “biofilm” was introduced in the 1970s[87], associated with medicine by Costerton in 1985.[88]

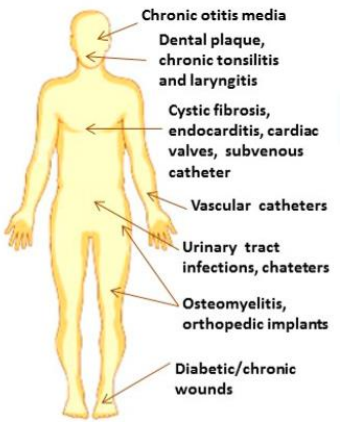

Figure 5: Scheme of biofilm-mediated infections[89]

Bacteria in biofilms can cause severe, long-lasting infections with damage to tissues and persistent inflammation as shown in *Figure 5*. They can grow on biotic surfaces such as teeth, heart valves and in lungs of CF patients, but also on abiotic surfaces such as catheters, prosthetic joints and artificial heart valves.[90] However, the impact of biofilms in infections has long been neglected. Nowadays, scientists estimate that 65-80% of all infections are biofilm-related.[91] A major problem with biofilm-related infections is that conventional antibiotic agents cannot eradicate these infections.[74] Also, sometimes, the immune system has difficulties recognizing and hence clearing biofilm infections.[92,93]

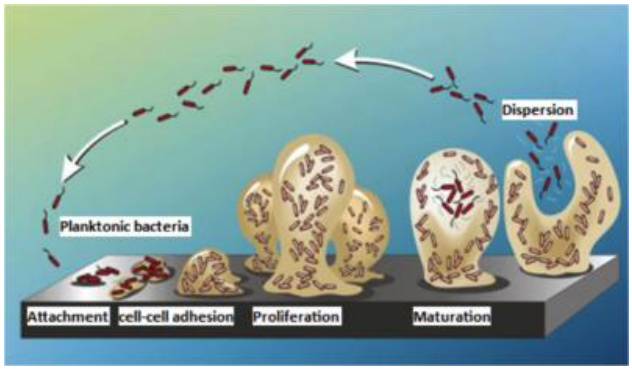

Figure 6: The life cycle of a biofilm[94]

In the first step of biofilm formation planktonic cells attach to the host's surface.[95] Bacteria use their pili and the secretion of sticky polymers in order to attach to the host's surface.[96] If they are attached irreversibly to the surface, they start multiplying yielding a micro-colony. As the biofilm grows, it gains in thickness and rearranges in a mushroom-like structure.[96] This is when biofilms are most tolerant to antibiotics.[96] Due to the self-produced extracellular matrix bacteria are stuck in the biofilm. After a certain time, bacteria can spread to other areas of the host, thereby re-infecting another location in the human body. The formation of a biofilm is depicted in *Figure 6*.[96]

Bacteria count 5 to 35% of a biofilm matrix.[97] The rest is a heterogeneous mixture of polysaccharides, proteins, eDNA, nutrients and essential minerals trapped from the environment.

Biofilm cells are less susceptible to antibiotic agents than planktonic cells.[90,98] Typically, one should increase antibiotic concentrations up to 1000 times to eradicate biofilm bacteria, in comparison with their free-floating planktonic counterparts.[99] This effect is dependent on the class of antibiotic agents used. Long known resistance mechanisms like target alterations, low cell permeability, efflux pumps and modifying enzymes - as mentioned above - only play a minor role in the susceptibility of biofilms.[83,90]

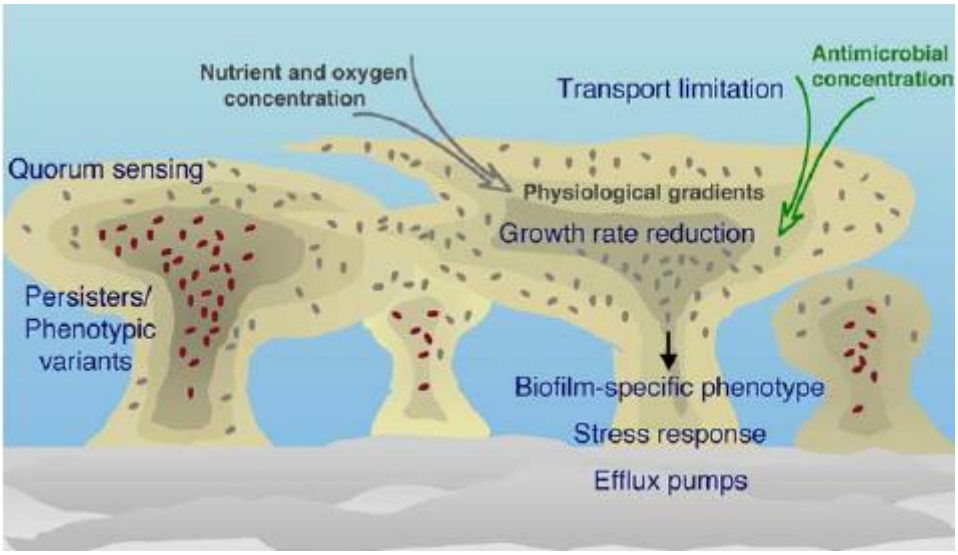

Figure 7: Mechanism of antimicrobial resistance in a biofilm[100]

The first reason for the high tolerance of biofilms is their typical “microenvironment”, characterized with regions of less O_2, lower pH and less metabolism.[96] Furthermore, it is observed that nutrients inside the biofilm are limited. Therefore, the growth rate is 5-15 times lower than in planktonic cells.[95,101]

Secondly, the biofilm matrix is often regarded as a barrier for penetration.[102] Bacterial cells are clustered together into dense clusters, which hampers penetration of molecules towards the deeper cell layers. Physicochemical interactions can occur between antibiotic molecules and biofilm matrix constituents, which also affects and inhibits antibiotic penetration. It has been reported that some antibiotics like aminoglycosides can be trapped inside biofilms by chelation with other polymeric structures such as alginates or DNAs present in biofilms[103]. Beta-lactam antibiotics can be inactivated by enzymes like β-lactamase present in the biofilms, which also affects their penetration through the biofilm.[90,104] Electrostatic interactions between a positively charged antibiotic and a negatively charged matrix compound might also contribute to a slow penetration.[102,105] The slower an antibiotic agent penetrates the

biofilm, the more time microorganisms are exposed to sub-inhibitory concentrations, which can lead to upregulation of defence mechanisms.[102]

Thirdly, bacteria can upregulate stress responses to antibiotics.[74,106] Oxidative stress responses such as OH^- are said to result in biochemical changes. It starts with the formation of ROS and leads to building of hydroxyl anion, which can cause severe tissue damage and cell death.[102,107] The OH^- level is dependent on nutrients and oxygen levels.[102,107]

Quorum sensing is another mechanism that bacterial biofilms use to protect their community. It is a common term used for bacteria that perform all biological activities as a group and hence communicate via species-specific extracellular chemicals.[84,108] N-Acylhomoserine lactones produced by biofilms of *Pseudomonas aeruginosa* can interact with transcriptional activators and enhance therefore the microbial resistance.[97,109] This expression of proteins is a response to an elevated population density[99] and to environmental changes[110].

Subspecies of cells called persisters also play a major role in the recalcitrance of biofilm bacteria.[83,111] They contribute largely to the grand resistance of a biofilm although their number is rather small (1%).[112] Persisters live in biofilms in a dormant mode, they are hidden from the host defence system and are able to reinflammate.[110] All those mechanisms[113], as depicted in *Figure 7,* may act synergistically, thus there is an urgent need for innovative strategies that can combat antimicrobial resistance.

3.4.3 Nanotechnology meets microbiology: liposomes in biofilm context

Using liposomes in the context of treating biofilm infections might have several benefits: firstly, they shield antibiotics from the extracellular matrix and from degrading enzymes inside the matrix[114] as well as prevent electrostatic and steric interactions. Examples of such unwanted interactions are for instance positively charged aminoglycosides, which are prone to interact with the negatively charged alginate matrix produced by biofilm cells or beta-lactam antibiotics that are inactivated by beta lactamases inside the matrix[115]. By loading liposomes with antibiotics a higher antimicrobial activity can be achieved compared to free antibiotics[116].

Secondly, liposomes can bind to the bacterial cell wall and deliver the drugs directly to the target site. So-called fusogenic liposomes are composed of a fluid phospholipid bilayer which enables them to fuse with biological membranes hence to deliver their cargo directly into the target cell.[3] The fluidity of membranes is highly dependent on the choice of phospholipids and their phase transition temperature rendering liposomes with unsaturated lipids a low Tc hence more fluid.[89] Fluidosomes ™, consisting of 1,2-dipalmitoyl-sn-glycero-3-phosphocholine (DPPC) and 1,2-

dimyristoyl-sn-glycero-3-phospho-(1'-rac-glycerol) (sodium salt) (DMPG) lipids, showed in several experiments a decreased viability of biofilm cells hence an increased antimicrobial effect[117–119]

Thirdly, using liposomes with an opposite surface charge compared to bacterial cells can prolong the contact time hence increase antimicrobial activity[3]. Positively, neutrally and negatively charged liposomes loaded with Clarithromycin were tested in terms of antimicrobial activity. Due to greater binding to the bacterial cells, positively charged liposomes showed the greatest antimicrobial effect, whereas negatively and neutrally charged liposomes were less active.[120]

Furthermore, by drug targeting, antibiotics can be directed to the biofilm, therefore adverse drug effects can be minimalised and MBIC can be lowered[116]. Omri et al[121] showed that, when tobramycin loaded liposomes were directed specifically to the lung, a high localized concentration of the antibiotic agent could be obtained, whereas no tobramycin was detected outside the lungs.[121]

Additionally, liposomes can either be targeted non-specifically or specifically to bacteria. E.g. by incorporating phosphatidylinositol (PI) into the liposomal bilayer targeting to a variety of biofilm-enclosed bacteria such as *Staphylococcus epidermidis*[122], *Proteus vulgaris*[122], *Streptococcus gordonii*[123,124], *Streptococcus sanguis*[125] and *Streptococcus mutans*[125] could be demonstrated. Due to hydrogen bonding between the hydroxyl groups of PI and polymers present on the bacteria, targeting can be obtained. The disadvantage of this method is its lower specificity, as many components can form hydrogen bonds.[3] Inclusion of lectins or antibodies can increase specificity that can bind to EPS molecules and/or sessile bacteria.[3]

Finally, by using liposomes, the release of the antibiotic load can be triggered close to bacterial cells ensuring high local concentrations of the antibiotic agent. External triggered systems such as liposomes with golden nanoparticles hence the effect of vapour nanobubbles have been discussed earlier. The local mechanical damage can be used to disrupt the liposomes as well as to loosen up the biofilm.[67] By disrupting the liposomes a local high concentration of antibiotics is ensured and the force of the VNBs can also be used to disrupt the dense clusters of bacteria rendering them more susceptible to antibiotics.[90,126] An internal trigger in context of biofilm infections has been reported by Meers et al.[127], who showed that rhamnolipids, a virulence factor present in *Pseudomonas aeruginosa* infections, could trigger the release of different agents due to their surfactant-like structure. As more rhamnolipids are present in close proximity to the biofilm, more drug will be released at the target site.[127]

Currently, there are no liposomal antibiotic drugs on the market.[127] Arikace (Amikacin encapsulated into DPPC/Chol liposomes) has reached phase III clinical trial, but was withdrawn prior to enrolment[127,128].

4 Materials and Methods

4.1 Materials

Lipids

DOTAP [1,2-dioleoyl-3-trimethylammonium-propane (chloride salt)] was bought from Avanti Polar Lipids, Inc. (Alabaster,AL). Its molecular weight is 698.542 g/mol and its phase transition temperature is below 5°C. DOTAP is a positively charged lipid. A stocksolution of 25 mg/mL was prepared in chloroform ($CHCl_3$).

DOPE [1,2-dioleoyl-sn-glycero-3-phosphoethanolamine] was bought from Avanti Polar Lipids, Inc. (Alabaster, AL). Its molecular weight is 744.034 g/mol and its phase transition temperature is -16°C. DOPE is a neutrally charged lipid. A stock solution of 25 mg/mL was prepared in chloroform.

DPPC [1,2-dipalmitoyl-sn-glycero-3-phosphocholine] was bought from Avanti Polar Lipids, Inc. (Alabaster, AL). Its molecular weight is 734.039 g/mol and its phase transition temperature is 41°C. DPPC is a neutrally charged lipid. A stock solution of 25 mg/mL was prepared in chloroform.

Cholesterol was bought from Sigma-Aldrich, Co. (St. Louis, USA). Its molecular weight is 386.7 g/mol. Cholesterol is a naturally neutrally charged lipid. A stock solution of 20 mg/mL was prepared in chloroform.

DOPC [1,2-dioleoyl-sn-glycero-3-phosphocholine] was bought from Avanti Polar Lipids, Inc. (Alabaster,AL). Its molecular weight is 786.113 g/mol and its phase transition temperature is -17°C. DOPC is a neutrally charged lipid. A stock solution of 25 mg/mL was prepared in chloroform.

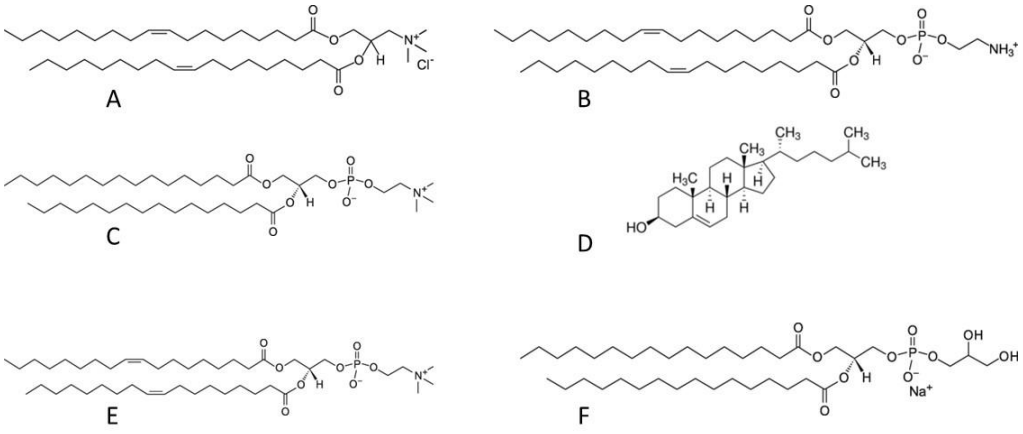

Figure 8 Molecular structures of lipids used in this diploma thesis: A) DOTAP, B) DOPE, C) DPPC, D) Cholesterol, E) DOPC and F) DPPG

DPPG [1,2-dipalmitoyl-sn-glycero-3-phospho-(1'-rac-glycerol) (sodium salt)] was bought from Avanti Polar Lipids, Inc. (Alabaster, AL). Its molecular weight is 744.952 g/mol and its phase transition temperature is 41°C. DPPG is a negatively charged lipid. A stock solution of 25 mg/mL was prepared in chloroform.

DiD

In order to visualize liposomes with fluorescence single particle tracking or confocal microscopy, fluorescent labelling of liposomes is required. DiD [1,1' dioctadecyl-3,3,3',3'-tetramethylindodicarbocyanine, 4-chlorobenzensulfonate salt) is a cationic, hydrophobic indocarbocyanide fluorophore (λ_{abs} = 644 nm and λ_{emm} = 665 nm). DiD is known to be little phototoxic and once applied to bilayers of lipids, it diffuses laterally, which results in a good uniformity.[129] DiD is commonly used to stain membranes for fluorescent imaging purposes.[129]

DiD was bought from Molecular Probes, Inc. (Eugene, OR). Its molecular weight is 1052,0753 g/mol. A stock solution of 2 mg/mL was prepared in chloroform.

DSPE-PEG 2000

DSPE-PEG 2000 [1,2-distearoyl-sn-glycero-3-phosphoethanolamine-N-[methoxy (polyethylene glycol)-2000](ammonium salt)] was bought from Avanti Polar Lipids, Inc. (Alabaster, AL). Its molecular weight amounts to 2805,497 g/mol and its phase transition temperature is 12,8 °C. A stock solution of 25 mg/mL was prepared in chloroform.

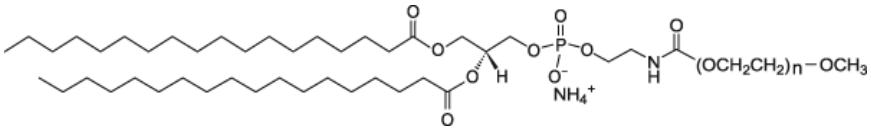

Figure 9: Molecular structure of DSPE-PEG 2000

C8 PEG 2000 ceramide

C8 PEG2000 ceramide [N-octanoyl-sphingosine-1-[succinyl(methoxy(polyethylene glycol)2000)] was bought from Avanti Polar Lipids, Inc. (Alabaster, AL). Its molecular weight is 2522,153 g/mol. A stock solution of 25 mg/mL was prepared in chloroform.

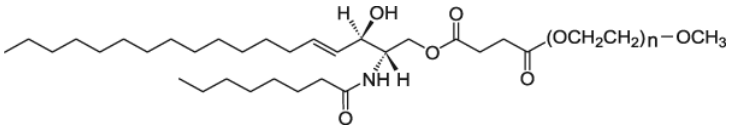

Figure 10: Molecular structure of C8 PEG 2000 ceramide

HEPES

HEPES [N-(2-Hydroxyethyl)piperazine-N'-(2-ethanesulfonic acid) is a commonly used buffer in biological experiments. HEPES was bought from Sigma-Aldrich, Co. (St.

Louis, USA). Its molecular weight is 238,30 g/mol. A 20 mM HEPES solution was prepared in ultra pure water type 1. The pH of the buffer solution was adjusted to 7,20 by adding the appropriate amount of 0,1 M NaOH while measuring the pH via a pH-meter (Multi-channel analyser, CONSORT, Belgium).

Calcein

Calcein (Bis[*N*,*N*−bis(carboxymethyl)aminomethyl]fluorescein) is a commonly used fluorophore in studies that invest new triggers for liposomal release (Λ_{abs}= 490 nm, Λ_{emm} = 520 nm).

In this thesis, a 100 mM calcein solution was encapsulated inside DOPC/DPPG liposomes to quench its fluorescence. It has been reported that calcein fluorescence is quenched[130] above a concentration of 70 mM.[131] Triggered release of calcein in the surrounding solvent results in a dilution of the calcein solution, which results in an increase in calcein fluorescence.

Calcein was bought from Sigma-Aldrich, Co. (St. Louis, USA). The molecular weight is 622,55 g/mol.[132] A stock solution of 100 mM was made in ultra pure water type 1.

In order to completely dissolve calcein, the sample was sonicated for 1 hour in a sonicator bath (Ultrasonic cleaner Branson 2510, BRANSONIC, Danbury, USA). As the solubility is also dependent on the pH of the solution, the pH was adjusted with 0,1 M NaOH to 7,2 with a pH-meter (Multi-channel analyser, CONSORT, Belgium).

Golden Nanoparticles

Golden nanoparticles (Au-NPs) were prepared in-house (Laboratory of General Biochemistry and Physical Pharmacy, Ghent) via the Turkevich Method[133,134]. Small Au-NPs of two distinct sizes were synthesized: 10 nm and 40 nm Au-NPs.

Chloroauric acid (HAuCl4) (Acros Organics N.V, Belgium), Sodium Citrate (Sigma-Aldrich, Co. St. Louis, USA), 4-(Dimethylamino)pyridine (DMAP) (Sigma-Aldrich, Co. St. Louis, USA), tetraoctylammonium bromide (Sigma-Aldrich, Co. St. Louis, USA), Toluene (Sigma-Aldrich, Co. St. Louis, USA), Sodium Borohydride ($NaBH_4$) (Sigma-Aldrich, Co. St. Louis, USA), Sodium Hydroxide (NaOH) (Sigma-Aldrich, Co. St. Louis, USA) and Sulfuric acid (H_2SO_4) were used to synthesize the golden NPs.

For the synthesis of 40 nm Au-NPs, 150 mL 0,2 mM $HAuCl_4$ and 0,5 mL 0,01 M citrate solution (1:1 $HAuCl_4$/Citrate molar ratio) were stirred under heat for 30 min. For the preparation of 10 nm Au-NPs coated with DMAP, a tetraoctylammonium bromide solution in toluene was mixed with an aqueous solution of $HAuCl_4$ under gentle stirring. An aqueous solution of $NaBH_4$ was then added to the dual phase mixture in order to create Au-NPs. After 30 min, the phase separation between organic toluene phase and aqueous phase was completed. Next, a washing step with H_2SO_4, NaOH and ultrapure

water respectively was performed. To induce ligand exchange from tetraoctyl-ammoniumbromide to DMAP, an aqueous solution of DMAP was added to the solution of Au-NPs in toluene in equal volumes. After equilibration of 1 hour, spontaneous transfer of Au-NPs to aqueous phase occurred, resulting in DMAP-decorated Au-NPs as endproduct.

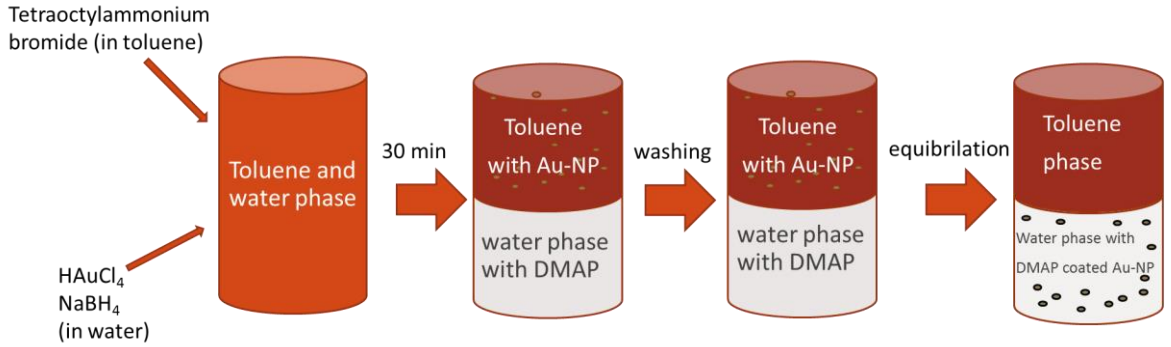

Figure 11: Schematic presentation of the reaction coating of nanoparticles with DMAP

4.2 Methods

4.2.1 Preparation of liposomes

There are different ways of preparing liposomes, all of them include four main stages: obtaining dried lipids, dispersion of the lipids, purification of the liposomes and finally analysis of the final product.[33] In this diploma thesis TFH[2] (thin film hydration) method followed by sonication was used. In this technique, lipids are mixed in an appropriate solvent, which will afterwards be evaporated yielding a dry lipid film. Next, this film is rehydrated with an aqueous medium and afterwards sonicated.

4.2.1.1 *TFH method*

As the liposomes were composed of different lipids, one must first dissolve the lipids in chloroform and mix them in the appropriate ratio in a round bottomed flask. To ensure sufficient mixing of the small lipid quantities, 1 mL chloroform was added to obtain a higher volume. Next, chloroform was rotary evaporated at <100 mbar (Vaccubrand PC 2001, Germany). In order to obtain a film containing a homogenous mixture of lipids, the evaporation was performed at a constant rotation speed of 180 rpm by connecting the round bottomed flask to a rotating unit (IKA, RV 10 digital, Staufen, Germany). During the evaporation process, a constant temperature above the phase transition temperature of the lipids was ensured by positioning the round bottomed flask in a warm water bath (IKA, HB 10,Staufen, Germany). In the next step, the dry lipid film was rehydrated with an aqueous solution containing the components that needed to be encapsulated inside the core of the liposomes. *Table 1-4* enlist the precise composition of the different liposomal constructions made during this master thesis. A small amount of 2 mm glass pearls (Glass Beads, MerckGaA, Germany) was added to the aqueous solution to ensure maximal encapsulation of the components inside the liposomes. Rehydration took place for 30 min at a specific temperature (IKA HB10, Staufen, Germany), which was specified by the phase transition temperature of the lipids.

In order to obtain a monodisperse sample consisting of small sized liposomes, the sample was then sonicated with a pulsed tip sonicator (BRANSON digital sonifier, Danbury, USA) for 1 min at 10% amplitude. In order to prevent overheating of particles every 10 seconds of sonication was followed by a 15 seconds pause (total sonication time = 1 min).

Sonication is a common means to reduce the size of liposomal constructions by using sonic energy.[135] Ultrasonic waves agitate multilamellar vesicles and result in their disruption yielding small unilamellar vesicles.[136] The lipids were stored at 4°C until further use.

4.2.1.1 *Preparation of fluorescently-tagged liposomes*

Sample name	Molar ratio of lipids	DOTAP (µL)	DOPE (µL)	DPPC (µL)	Chole-sterol (µL)	DiD (µL)	HEPES buffer (µL)	PEG 2000 (µL)	Cer-PEG (µL)
CAT-lipo	49,5:49,5:1	76	81			29	200		
CAT-PEG-lipo	42:42:15	45	48			20	200	65	
CAT-Cer-PEG-lipo	42:42:15	47	50			21	200		61
NEU-lipo	49,5:49,5:1			103	68	37	200		
NEU-PEG-lipo	52:32:15			65	26	22	200	72	
NEU-Cer-PEG-lipo	52:32:15			68	28	24	200		68

Table 1: Volumes of lipids used in the preparations of liposomes for visualization experiments. Liposomes consisted of lipids with a final concentration of 20 mg/mL: CAT-lipo= DOTAP/DOPE/DiD liposomes non pegylated, CAT-PEG-lipo=DOTAP/DOPE/DiD liposomes pegylated with DSPE-PEG2000, CAT-Cer-PEG-lipo= DOTAP/DOPE/DiD liposomes pegylated with C8 PEG2000 Ceramide, NEU-lipo= DPPC/Chol/DiD liposomes non pegylated, NEU-PEG-lipo= DPPC/Chol/DiD liposomes pegylated with DSPE-PEG 2000, NEU-Cer-PEG-lipo= DPPC/Chol/DiD liposomes pegylated with C8 PEG2000 Ceramide

Table 1 enlists the composition of the different types of liposomes tested in the visualization experiment. The rehydration temperature for CAT-lipo, CAT-PEG-lipo and CAT-Cer-PEG-lipo was held above 40 °C. NEU-lipo, NEU-PEG-lipo and NEU-Cer-PEG-lipo were rehydrated at 60 °C. In order to fluorescently label the liposomes, 1 mol% of DiD was added to the formulation. PEGylation takes place during or after liposomal formation. Volumes of *Table 1* refer to the pegylation during liposomal formation. In this diploma thesis two different PEG-chains were used: DSPE-PEG2000 and C8 PEG2000 Ceramide. DSPE-PEG2000 is a PEGylated lipid where the PEG-chain is covalently attached to the lipid molecule. In C8 PEG2000 Ceramide, often referred to as Cer-PEG, the PEG-chains are linked to a ceramide molecule, which has interesting properties. In contrast to DSPE-PEG2000, ceramide can diffuse out of the liposomal bilayer after interaction with biological membranes leaving a sheddable PEG coat. Initially it provides good penetration properties, but after interaction with bacterial cells liposomes get immobilized becoming a local depot.[137] We also tested a second series of liposomes that were PEGylated after liposome preparation, the so-called 'POST-PEGylated liposomes' (results not shown). For the POST-PEGylation, liposomes were prepared as described above, but without the inclusion of PEG-molecules. After sonication, 40 µL chloroform dissolved PEG-chains were evaporated under nitrogen flow. The dried PEG-film was rehydrated with the appropriate amount of ultra pure water type 1. Then, 6 µL of water-dissolved PEG-chains were added to 30 µL of positively and slightly negatively charged, diluted liposomes (1:2,5) (10 mol%

lipids = PEG). Finally, the liposomes were incubated for 1 h at 200 rpm in an orbital shaking incubator to ensure complete penetration of PEG-molecules in the liposomal bilayers.

To calculate the appropriate amount of ultra pure water type 1, firstly the dilution of the initial liposomal concentration (10 mM) in 200 µL to 4000 µM / l was taken into account. As 6 µL of PEG-solution was added to 30 µL liposomal suspension (30 µL liposomal suspension + 6 µL PEG-solution = 36 µL diluted liposomal suspension), a dilution factor of 1,2 was calculated for the diluted liposomal sample ((30 µL liposomal suspension + 6 µL PEG-solution) / 30 µL liposomal suspension = 1,2 dilution factor) yielding a final lipid concentration in the Eppendorf of 3333 µM (4000 µM / 1,2 = 3333 µM liposomal sample after PEG addition).

To ensure a PEG-concentration of 10 mol% (3333 µM * 0,1 = 333 µM) the concentration of the re-dissolved PEG-solution had to be recalculated.

As a PEG-concentration of 333 µM in 36 µL was required, the required PEG-concentration in 6 µL was 1998 µM ((36 µL * 333 µM) / 6 µL = 1998 µM).

As 40 µL of the initial PEG-stock was used, the calculated volume of ultra pure water type 1 for DSPE-PEG was 178 µL ((8900 µM initial PEG-concentration * 40 µL) / 1998 µM = 178 µL ultra pure water), whereas C8-PEG2000 required 198 µL of ultra pure water type 1 ((9912 µM initial PEG-concentration * 40 µL) / 1998 µM = 198 µL ultra pure water).

4.2.1.2 *Preparation of fluorescent liposomes for triggered drug release experiments*

In order to obtain fluorescent liposomes, 100 mM calcein was encapsulated inside liposomes via the TFH method as described before. Both positively and negatively charged liposomes were made by incorporating the lipids DOTAP and DOPE or DOPC and DPPG in the formulation respectively. The lipids were hydrated with calcein or HEPES-buffer at a constant temperature of 45 °C.

Sample name	Molar ratio of lipids	DOPC (µL)	DPPG (µL)	DPPC (µL)	Cholesterol (µL)	Calcein solution (µL)	HEPES buffer (µL)
AN-CAL-lipo	80:20	162	96			250	
AN-HEP-lipo	80:20	162	96				250
AN-CAL-lipo	80:20	323	191			500	
AN-HEP-lipo	80:20	323	191				500
CAT-CAL-lipo	1:1			187,5	210	500	
CAT-HEP-lipo	1:1			187,5	210		500

Table 2: Volumes of lipids used for the preparation of fluorescent liposomes for triggered liposomal release. Liposomes were made with final lipid concentration of 20 mg/mL. AN-CAL-lipo= DOPC/DPPG liposomes with encapsulated calcein, AN-HEP-lipo= HEPES loaded DOPC/DPPG liposomes, CAT-CAL-lipo = Calcein loaded DOTAP/DOPE liposomes, CAT-HEP-lipo= HEPES loaded DOTAP/DOPE liposomes

Glass beads ensured a higher encapsulation of the fluorophore. *Table 2* enlists the volumes of lipids and solvents used to synthesize the fluorescent liposomes. Liposomes described in *Table 2* and *Table 4* were prepared via the TFH method. AN-CAL-lipo, AN-HEP-lipo, CAL-Au-lipo and HEPES-Au-lipo were rehydrated at 45 °C whereas CAT-CAL-lipo and CAT-HEP-lipo were rehydrated at 40 °C.

In order to make the liposomes light sensitive, Au-NPs were included in the liposomal formulations. Detailed description of the preparation can be found in section *4.2.6.1.Functionalization of liposomes with Au-NPs.*

4.2.1.3 *Preparation of tobramycin loaded liposomes*

Liposomes described in *Table 3* were prepared via TFH method. AN-TOBRA-lipo and AN-HEP-lipo were rehydrated at 45 °C, whereas NEU-TOBRA-lipo and NEU-HEP-lipo were rehydrated at 60 °C.

Sample name	Molar ratio of lipids	DOPC (µL)	DPPG (µL)	DPPC (µL)	Cholesterol (µL)	80 mg/mL tobramycin solution (0,9 % NaCl (w/v)) (µL)	HEPES buffer (µL)
AN-TOBRA-lipo	80:20	162	96			250	
AN-HEP-lipo	80:20	162	96				250
NEU-TOBRA-lipo	55:45			140	75	250	
NEU-HEP-lipo	55:45			140	75		250

Table 3: Volumes of lipids used for the preparation of antibiotic loaded liposomes. Liposomes were made with a final lipid concentration of 20 mg/mL TOBRA-lipo= DOPC/DPPG liposomes with tobramycin encapsulated. AN-HEP-lipo= DOPC/DPPG rehydrated with HEPES; NEU-TOBRA-lipo= Tobramycin loaded DPPC/Chol liposomes; NEU-HEP-lipo= HEPES loaded DPPC/Chol liposomes.

4.2.2 Purification of liposomes

4.2.2.1 *Ultracentrifugation*

Ultracentrifugation is a common means to separate loaded liposomes from non-encapsulated loading material. It is based on the sedimentation rate of a particle as larger particles have a faster sedimentation rate than smaller particles.

$$v = \frac{d^2(\rho - L) \times g}{18\eta}$$

v=sedimentation rate or velocity of the sphere
d= Diameter of the sphere (m)
p= particle density(kg/ m^3)
L=medium density(kg/m^3)
n= viscosity of medium(kg/m.s)
g= gravitational force(N.m^2/kg^2)

Equation 1: The Stokes Equation[138]

The sedimentation of particles is calculated by the Stokes Equation[138]. The sedimentation rate of a particle is faster when the diameter of a particle is increased or the gravitational force is elevated. Moreover, low viscosity of the medium has a positive impact on the sedimentation rate. In order to achieve a complete separation, suspensions are exposed to a high gravitational force. The heavier parts are then found as a pellet on the bottom of the centrifuge tube and can be easily collected.[138]

4.2.2.2 *Size exclusion chromatography*

Size exclusion chromatography, also known as Gel filtration, is another common method to separate drug loaded liposomes from non-encapsulated drugs. The crucial parameter is particle size, more precisely the hydrodynamic volume[139]. The stationary phase consists of a packed bed with porous gel. The mobile phase with the liposome-encapsulated and non-encapsulated drug flows through the packed column. This separation technique depends on the ratio between pore size and molecular size.[140] Large particles have less access to the pores than small particles, therefore the retention time for small particles inside the pores of the gel is longer than for large particles.[141] For this reason it is suitable to separate drug loaded liposomes and free, non-encapsulated drugs.

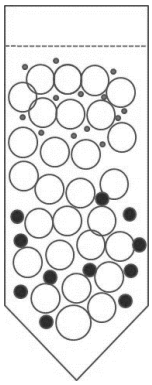

Figure 12: Scheme of Size exclusion chromatography; smaller particles have a longer retention time whereas large particles flow faster through the column. That is why this method is used to separate encapsulated liposomes (large dots) from free floating calcein (small dots).

In this diploma thesis Spin-columns for liposome purification (Liposomics, USA) were used to separate drug-encapsulated liposomes from free floating drugs. These columns were specifically designed for the removal of free floating drugs in liposomal samples as the separation is based on absorbance and size exclusion.[142] The advantage of using these columns instead of other commercially available or self-produced Sephadex columns are that (1) the liposomal samples do not need to be diluted, (2) the procedure is very quick (few minutes) and (3) only a small negligible amount of liposomal sample may bind to the column.[142]

Figure 13: Picture of the Spin-column with calcein-loaded liposomes flowing through the column.

For the column preparation, columns without bottom tip were inserted in 1,5 mL Eppendorfs and centrifuged two times at 1000 rpm for 1 min. Afterwards, 150 µL of 20 mM HEPES buffer (pH 7,2) was added on top of the column and centrifuged for 2 min at 1000 rpm. After a final centrifugation for 4 minutes at 1000 rpm, the columns were ready to use. 100 µL of the vortexed sample was added on the column and centrifuged for 4 minutes at 1000 rpm. The liposomal sample could then be collected and stored at 4 °C until further use, whereas the column was discarded.

4.2.3 Characterization of liposomes

4.2.3.1 *DLS*

Dynamic Light Scattering[143] (DLS) is used to measure the size of nanoparticles in suspension based upon their diffusion caused by Brownian Motion. Brownian Motion, dependent on the particle size, is a random movement caused by collision of particles with solvent molecules.[144] Monochromatic laser light will be scattered at the boundary between particle and solvent molecule. A detector collects all the scattered light and the total intensity is measured. Due to Brownian motion this intensity changes over time. The analysis of these intensity fluctuations yields the movements of the particles. Larger particles diffuse slower than smaller particles depicted by *Figure 14*. The Stokes-Einstein-Equation converts the diffusion of particles into size and size distribution. This conversion is limited to spherical particles.

$$dH = \frac{kT}{3\pi\eta D}$$

dH= hydrodynamic diameter (m)
k= Boltzmann's constant (m^2.kg/K.s^2)
T=absolute temperature (K)
η = viscosity of the medium (kg/m.s)
D= diffusion coefficient (m^2/s)

Equation 2: Stokes-Einstein-Equation[145]

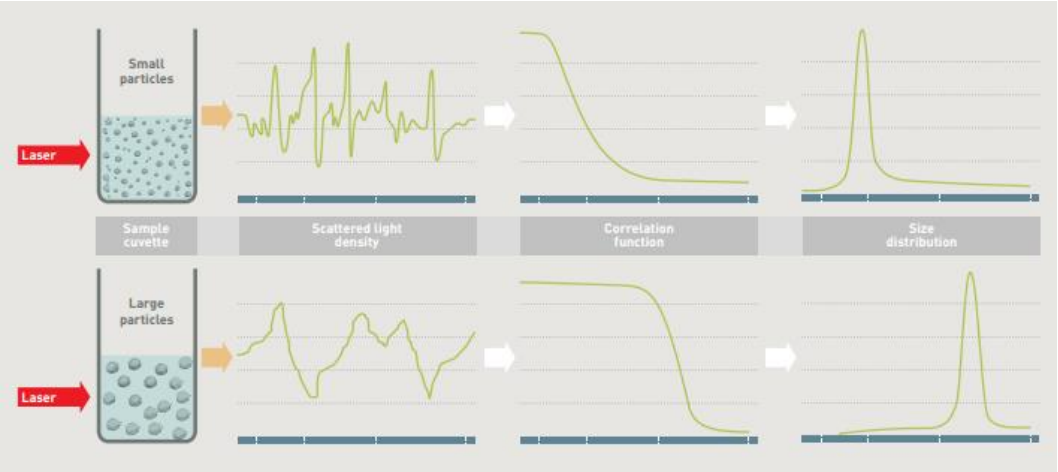

Figure 14: Scheme of the principle behind Dynamic Light Scattering[143]

With DLS, it is also possible to assess the polydispersity of the sample. Whether the sample consists of a single population with a uniform size or multiple populations with different sizes is depicted in the polydispersity index (PDI). The PDI, is a dimensionless parameter between 0 and 1, representing a monodisperse population when its value is <0,3, while a polydisperse sample is depicted by a PDI >0,7.

Besides the ability to measure the size of nanoparticles, it is also common to determine the surface charge of particles, the so-called “zeta potential”.[146] Counterions in the solvent are affected by the net surface charge of nanoparticles. These counterions built up the stern layer. Surrounding the stern layer, there is a diffusion layer with less strongly bound counterions, as visualized in *Figure 15*.[146]

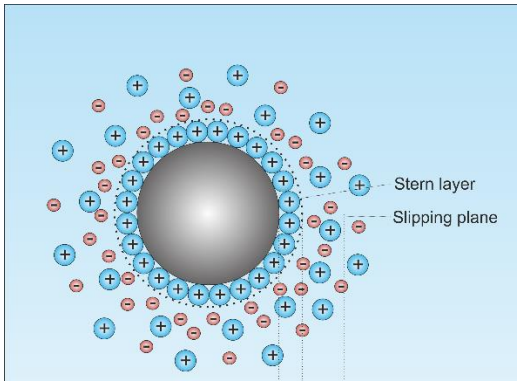

Figure 15: Location of zeta potential[147]

Through friction, some of these counter ions can get lost, resulting in the slipping plane. The zeta potential is measured at this slipping plane. When an electric field is applied across the solution, particles are attracted to the counter electrode. They scatter monochromatic laser light, which is collected by a detector and interpreted in terms of the zeta potential. The frequency of the fluctuation is proportional to the migrating particles.[143] The electrophoretic mobility is correlated to the zeta-potential by using *Equation 3.*

$$\zeta = \frac{3\mu\eta}{2\varepsilon f(Ka)}$$

μ=electrophoretic mobility (m^2/V.s)
η= viscosity of the medium (kg/m.s)
ε=dielectric constant
f(Ka)= Henry's function

Equation 3: Henry's equation[148]

Following each critical step during liposome preparation, the hydrodynamic size and zeta-potential of the liposomes were measured by DLS. Therefore, the samples were diluted 1:100 in HEPES-buffer (10 µL liposomes and 990 µL 20 mM HEPES- buffer, pH=7,2). The sample was measured in a disposable folded capillary cuvet (Malvern Instruments Ltd., Worcestershire, UK) with the Malvern Zetasizer nano ZS (Malvern Instruments Ltd., Worcestershire, UK). Each sample was measured in triplicate at 25 °C and analysed with the Zetasizer Software.

4.2.3.2 *Fluorescence Single Particle Tracking*

Fluorescence single particle tracking[149] (fSPT) is a method to measure the movement of particles based on fluorescence microscopy. Laser light irradiating fluorescent labelled nanoparticles and a sensitive electron multiplying charge coupled device (EMCCD)-camera allow to record the movement of particles below the resolution of the microscope. The movies are analysed with a special software, that enables to track the trajectories of every particles.[150]

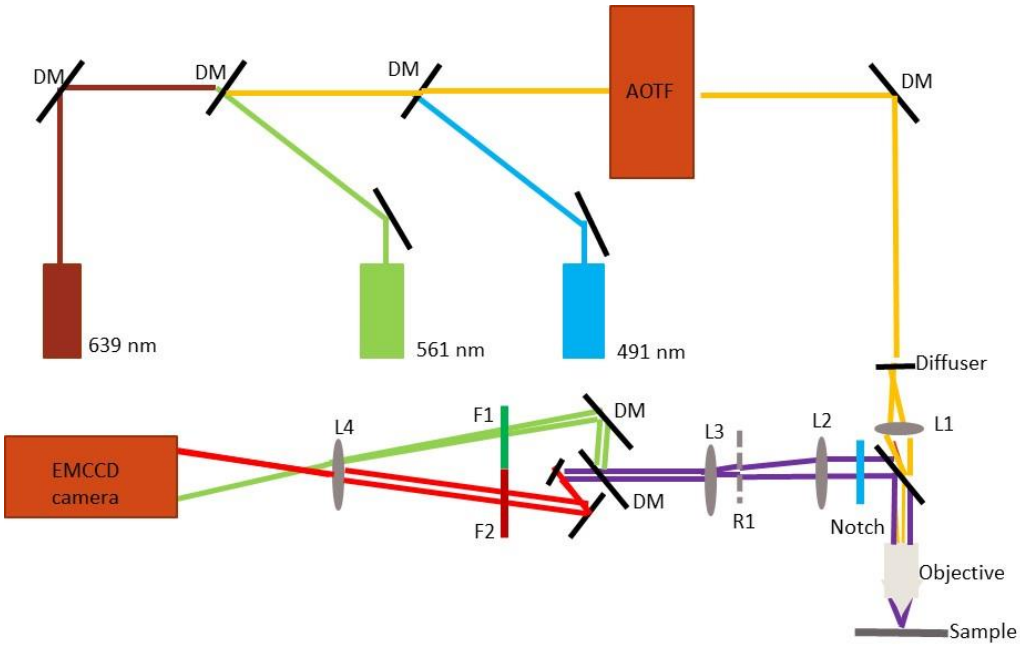

Figure 16: Optical set-up of fluorescence single particle tracking. DM= dichroic mirror, AOTF= acustico optico tunable filter, L1= lens 1, Notch= Notch filter, L2= lens 2, L3= lens 4, F1, F2= focal length, L4= lens 4, EMCCD camera= electron multiplying charge coupled device(adapted from [150])

The optical set-up used for this diploma thesis is displayed in *Figure 17*. In general one can distinguish between three different parts: the excitation path, the microscope and the emission path as depicted by *Figure 16*.[150]

The first part of the excitation path are three lasers with different wavelengths (100 mW Calypso 491 nm (Cobolt, Solna, Sweden), 75 mW Jive 561 nm (Cobolt) and 100 mW Spectra Physics Excelsior 646 nm (Newport, Irvine CA, USA)), which ensure illumination for a broad range of fluorophores. Dichroic mirrors ensure that all three laserlines are aligned right before the AOTF (acusto-optical tunable filter), which ensures regulation of the intensity. The AOTF is connected to the EMCCD-camera, in order to prevent photobleaching. A diffuser (5° Light Shaping Diffuser (Physical Optics Corporation, Torrance, CA)) and an achromatic lens are the last parts of the excitation path, which provides a widefield illumination with parallel bundels.

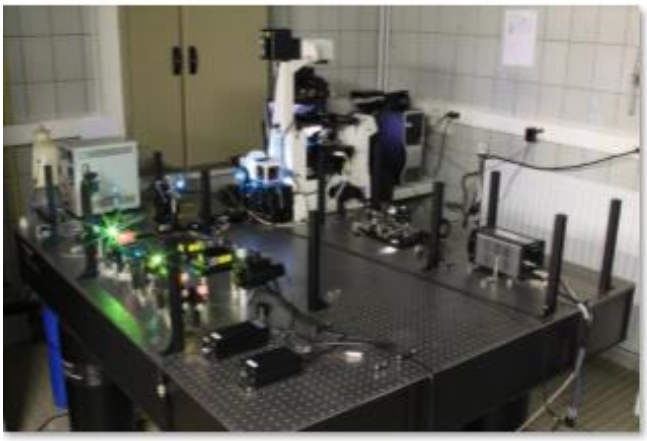

Figure 17: Home-made set-up of fSPT in the laboratory

The microscope is an epifluorescent microscope (Nikon TE2000-E (Nikon BeNeLux, Brussels, Belgium)) used with a Plan Apo VC100x 1,4 NA oil immersion objective lens.

Emitted fluorescent light from the sample is collected by the objective lens. A dichroic mirror separates emitted light from excitation light. The laser notch filter (AHF Analysentechnik, Tübingen,Germany) ensures that only emitted light from the sample is directed towards the EMCCD camera, which makes it possible to take movies of small, fast and faint particles. These movies are taken with NIS Elements software (Nikon).

Fluorescent single particle tracking should only be performed with highly diluted samples[150], as particles should not overlap during a movie. In this diploma thesis, the liposomes were diluted 1:4000 in HEPES-buffer (20 mM, pH=7,2). 50 µL of this liposomal dilution was transferred into a 96-well Sensoplate (SensoPlate (Greiner Bio-One). As DiD was used as a fluorophore (excitation wavelength = 644 nm) the 100 mW Spectra Physics Excelsior 646 nm was used as an excitation light. To ensure a representative measurement, 20 movies in different locations of the well were

captured with the EMCCD-camera. A movie duration of 5,27 seconds was ensured for each measurement and the frames per second were 20,69. Each measurement was performed in triplicate. The resulting 60 movies were analysed afterwards via MATLAB.

Image processing consisted of two parts: firstly, the particles' coordinates needed to be identified while removing the background signal.[150] In a second step, the software recreated the trajectories of the particles via the nearest neighbour algorithm.[150]

Finally, the trajectories were used to calculate the concentrations of the liposomes via a method, developed by Magnus Röding.[151]

4.2.4 Localization of liposomes inside biofilms

4.2.4.1 *Fluorescence Microscopy*

Fluorescence microscopy is based upon the fact, that some molecules can absorb excitation light of a certain wavelength emitting a longer wavelength.[152] Fluorophores mostly attach specifically to certain structures and have a significant quantum yield, which is defined by the number of emitted photons per absorbed photon.

With fluorescent labelling, it is possible to irradiate specimen with a defined wavelength. In *Figure 18*, the excitation path is indicated in blue. A dichroic mirror ensures that all excitation light reaches the sample. The much weaker emitted fluorescent light, represented in red is then separated from the excitation light by a filter. The filter ensures that only weak emitted fluorescent light reaches the detector.[152]

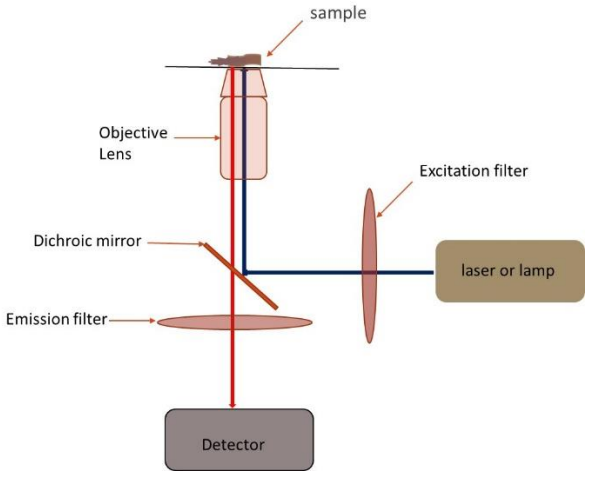

Figure 18: Schematic illustration of the set-up of a fluorescence microscope

4.2.4.2 *Confocal Microscopy*

Confocal Microscopy is also based upon fluorescent microscopy. As fluorescent light moves to all directions, out of focus light affects the image quality.[153]

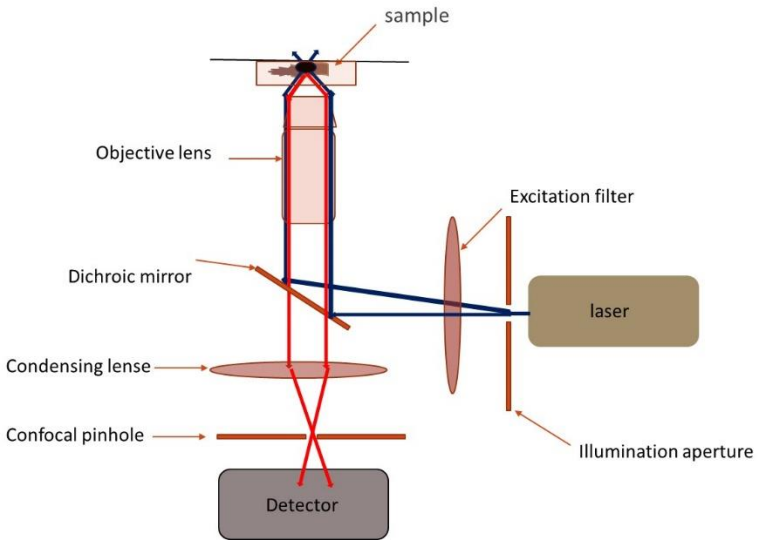

Figure 19: Schematic illustration of the set-up of a confocal microscope

Therefore, the set-up of confocal microscope is complemented by a light source pinhole and a detector pinhole. Confocal microscopy combines point detection with point illumination. It is therefore guaranteed that only light of a certain layer is collected. The laser is scanning the sample point by point having only small areas of the sample in focus at once. Afterwards, the output of the photomultiplier is translated into a picture.[153]

In *Figure 19* the set-up of a confocal microscope is shown. The confocal principle is shown in *Figure 20*.

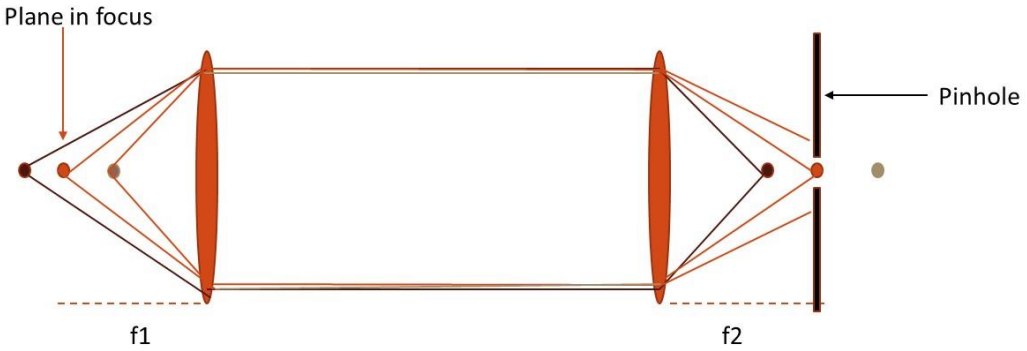

Figure 20: The confocal principle; Light in focus plane is directed through the pinhole (orange beam); light of out-of-focus-planes are stopped by the pinhole (red and grey beam)

4.2.5 Experimental set-up for visualization experiment

The first question we wanted to answer in this thesis was whether positively and negatively charged liposomes were differently located inside biofilms. Besides the impact of surface charge, we also wanted to investigate if inclusion of PEG-chains in the liposomal bilayer composition would affect their distribution in bacterial biofilms. Two types of bacterial strains were selected for cultivation of bacterial biofilms:

Burkholderia multivorans LMG18825 and *Pseudomonas aeruginosa* LESB58, both clinical isolates from a cystic fibrosis patient. Biofilms were cultured in 96-well SensoPlates™ (Greiner Bio-One) with microscopy grade bottom for 24 hours at 37 °C. Briefly, a pure culture of *Burkholderia multivorans* was grown on a Mueller Hinton Agar plate and incubated at 37 °C. After 24 hours, the bacteria were suspended in Mueller Hinton Broth and incubated overnight in an orbital shaking incubator at 250 rpm at 37 °C. Then, the bacterial suspension was diluted in order to obtain a working solution of approximately 5 x 10^7 colony forming units by adjusting the optical density to 0.05 at a wavelength of 595 nm. The wells of the 96-well SensoPlate were filled with 100 µL of the diluted bacterial suspension, and incubated at 37 °C. After 4 hours, the adhered cells were washed with 0.9 % NaCl (w/v), covered with medium and incubated for another 20 h at 37 °C. The same culture procedure was used to grow *Pseudomonas aeruginosa* biofilms, with the use of Lysogeny Agar/Broth as culture medium instead of Mueller Hinton Agar/Broth.

24 hours old biofilms of *B. multivorans* and *P. aeruginosa* were stained with 100 µL of a 20 µM SYTO 9 solution (Invitrogen). SYTO stains are able to stain DNA as well as RNA. It targets nucleic acids in live or death cells as well as gram-positive and gram-negative bacteria.[154] The plate was incubated at room temperature (25 °C) and protected from light for 30 minutes. The biofilms were rinsed with 100 µL 0.9 % NaCl (w/v) to wash away the free fluorophores. Next, the liposomal formulations (given in *Table* 1) were diluted 1:1000 in HEPES-buffer to ensure a good image quality and avoid oversaturation of the detector of the microscope. The biofilms were covered with 100 µL of the diluted liposome suspensions and incubated for 15 minutes at room temperature to allow complete penetration inside the biofilm architecture. After 15 minutes the supernatant was removed and the biofilms were washed once more to remove any free-floating liposomes that did not have the capability to penetrate the biofilms.

To visualize the nanoparticles and the biofilm at the same time, a swept-field confocal microscope (Nikon Benelux, Brussels, Belgium) was used with a Plan Apo VC 60 x 1.4 NA water immersion objective lens (Nikon). A 488 nm laser was used to illuminate the SYTO 9-stained bacteria, the liposomes were visualized by illuminating the sample with a 647 nm laser. The 488 nm laser was used at 7 % intensity and the 647 nm laser at 23 % intensity. The software to capture the images was the NIS Elements Advanced Research package (Nikon).

4.2.6 Functionalization of liposomes

4.2.6.1 *Functionalization of liposomes with Au-NPs*

To render liposomes light-sensitive, a photosensitive group had to be introduced in the liposomal formulation. In this diploma thesis, 2 types of liposomes were made:

(1) liposomes containing Au-NPs inside their lumen, and (2) liposomes with Au-NPs attached on the liposomal surface. The first set of liposomes is composed of DOPC and DPPG as compromising lipids. Au-NPs were entrapped in the lumen by hydrating the DOPC/DPPG lipid film with 10 nm Au-NPs and calcein (2.4 % Au-NPs/calcein (v/v) and 25 % Au-NPs/ calcein (v/v)). The exact volumes used to prepare this kind of liposomes are displayed in *Table 4.*

Hydrodynamic size and zeta potential of both calcein loaded and HEPES-buffer loaded liposomes were measured by DLS.

Sample name	Molar ratio of lipids	DOPC (µL)	DPPG (µL)	Calcein solution (µL)	HEPES buffer (µL)	Au-NPS (10 nm) (µL)
AN-CAL-low Au-lipo	80:20	323	191	488		12
AN-HEP-Au-lipo	80:20	323	191		488	12
AN-CAL-high Au-lipo	80:20	323	191	400		100

Table 4: Volumes of lipids used for the construction of liposomes containing Au-NPs inside their lumen. Liposomes consist of volumes with 20 mg/mL. AN-CAL-Au-lipo = DOPC/DPPG liposomes with calcein and golden NPs encapsulated. AN-HEP-Au-lipo = DOPC/DPPG rehydrated with HEPES and Au-NPs.

A second series of liposomes was made by attaching either 40 nm or 10 nm Au-NPs on the surface of DOPC/DPPG liposomes. DOPC/DPPG liposomes were made as before *Table 2.* Golden nanoparticles were synthesized as described in *4.1 Materials*. The functionalization is based on electrostatic interactions as AN-CAL-lipo and AN-HEP-lipo are negatively charged and the golden nanoparticles showed a positive surface charge. Different ratios of golden nanoparticles, displayed in *Table 5* and *Table 6* were added to AN-CAL-lipo suspended in HEPES buffer. Prior to the functionalization step, 40 nm Au-NPs were centrifuged at 7000 rpm for 5 min in order to get rid of the excipients.

For every type of Au-liposome construct, the hydrodynamic size and zeta potential was measured by DLS.

For the second batch of liposomes (Au-NPs attached to the liposomal surface), a detailed study was done to determine the laser pulse energy needed to create vapour nanobubbles for every type of liposome (section *4.2.7.1 Generation and detection of VNBs around liposomes).* Next, calcein release was measured with the optimized laser illumination parameters (see *4.2.9 Calcein release via pulsed laser trigger)*

10 nm Au-NPs			
Sample name	**AN-CAL-lipo (1:100 dil) (µL)**	**10 nm Au-NPs (1:10) (µL)**	**Ultra pure water type 1 (µL)**
*10Au-lipo-10	10	10	980
*10Au-lipo-50	10	50	940
10Au-lipo-100	10	100	890
*10Au-lipo-150	10	150	840
*10-Au-lipo-200	10	200	790
10Au-lipo-300	10	300	690

Table 5: AN-CAL-lipo functionalized with different ratios of 10 nm golden nanoparticles, samples marked with a * were used for the threshold experiment.10 nm Au-NPs were measured in Type 1 ultrapure water, instead of HEPES-buffer, due to the unfavourable salt concentration of HEPES-buffer.

40 nm Au-NPs			
Sample name	**AN-CAL-lipo(µL)**	**40 nm Au-NPs (µL)**	**HEPES- buffer (µL)**
40Au-lipo-2	10	2	988
40Au-lipo-5	10	5	985
*40Au-lipo-10	10	10	980
40Au-lipo-20	10	20	970
40Au-lipo-30	10	30	960
40Au-lipo-40	10	40	950
*40Au-lipo-50	10	50	940
40Au-lipo-60	10	60	930
40Au-lipo-70	10	70	920
40Au-lipo-100	10	100	890
*40Au-lipo-200	10	200	790
*40Au-lipo-300	10	300	690

Table 6: Different ratios of 40 nm golden nanoparticles functionalized with AN-CAL-lipo; samples marked with a (*) were used for the threshold experiment

4.2.7 Generation and detection of VNBs associated to liposomes

4.2.7.1 *Generation and detection of VNBs around liposomes*

Generating VNBs might be used as a trigger for liposomal calcein release. Plasmonic NPs can convert light energy into heat energy efficiently as explained in *3.3.2 Light-triggered liposomal release*.

The energy absorbed by the NP that goes into a heating regime is determined by the heating efficiency (ϕheat, defined as the fraction of absorption over the total extinction - energy that is absorbed goes into a heating regime as particles are not efficient emitters). 10 nm Au-NPs show in terms of heating efficiency a better performance than 40 nm Au-NPs since the scattering component to the total extinction is almost

negligible for small NPs. However, studies showed that in terms of vapour nanobubble generation bigger nanoparticles outperform small NPs, which show a higher heat diffusion to the surrounding environment. Moreover, bigger NPs show a higher absorbed cross-section (σabs), which increases with the size of the NP until approximately 80-90 nm, regime in which the σabs is proportional to the volume of the NP. Therefore, for studies based in nanobubble generation, the effective energy absorbed and the volume of NPs must be considered. Theoretical calculations of the newly defined parameter absorbed energy per volume unit (W m-3) shows that 40 nm NPs depict a better performance than 10 nm NPs.

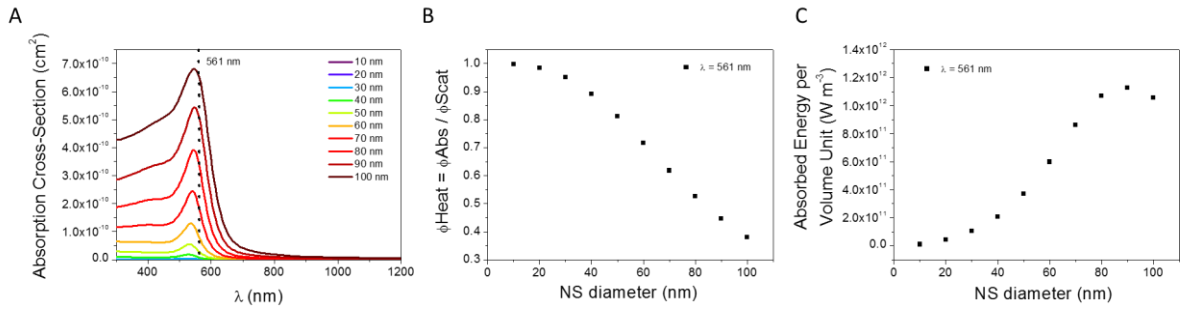

Figure 21: Theoretical calculations of (A) σabs, (B) ϕheat and (C) S(t) as a function of NP diameter for nanospheres (not published).

To investigate at which energy VNBs are formed around liposomes, different amounts of golden nanoparticles were added to AN-CAL-lipo as explained in *4.2.6.1 Functionalization of liposomes with Au-NPs*. The aim is to create liposomes with high and low coverage of Au-NPs, hence to obtain low decorated and high decorated Au-functionalized liposomes. For each batch, given in *Table 5* and *Table 6* the hydrodynamic size and the zeta potential were measured via DLS.

For both 10 nm as well as 40 nm Au-NP functionalized liposomes, four ratios (Au:liposome), marked with a (*) in *Table 5* and *Table 6* were selected corresponding to a sample with low and high coverage of Au-NPs on the liposomal surface. 10Au-lipo10 and 40Au-lipo10 correlate to the lowest coverage, 10Au-lipo50 and 40Au-lipo50 to low coverage, whereas 10Au-lipo100 and 40Au-lipo200 correspond to high coverage and 10Au-lipo150 and 40Au-lipo300 to highest surface coverage.

Next, the potential of these constructs to generate vapour nanobubbles was investigated. A home-made optical set-up was used to generate and detect vapour nanobubbles, according to the design shown in *Figure 22*.

The set-up is built around a fully automated epi-fluorescence microscope. The Optical Parametric Oscillator (OPO) laser produces laser pulses of 7 ns at a repetition rate of 10 Hz. The laser wavelength can be continuously tuned from 400 nm to 2000 nm in order to match the plasmonic absorption peak of the various Au-NPs. The laser pulse energy can be adjusted in order to obtain the optimal laser pulse fluence to generate

VNBs (2.5 J / cm²). An electronic sample stage (3000 µm / s) allows to scan the sample automatically across the pulsed laser beam.

The generation of VNBs was visually confirmed by dark-field microscopy as scattered light of VNBs can be seen. Dark field microscopy is a common method to visualize structure with similar refractive values as the background.[155] By using a dark field condenser direct light is blocked hence only scattered light reaches the specimen, which appears bright on a dark background.[156]

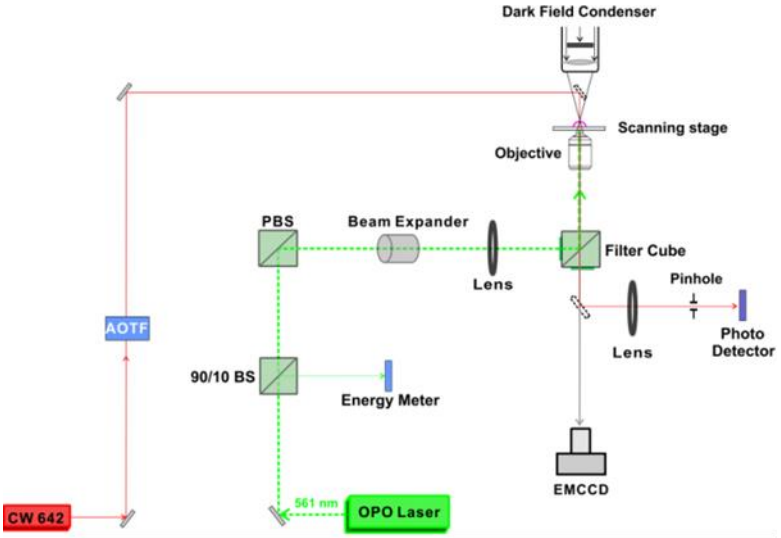

Figure 22: Optical set-up to generate and detect VNBs

Liposomal samples were prepared under the laminar air flow as follows: Liposomes were diluted in HEPES-buffer until a particle concentration of 10^9 particles/mL so that a good image quality was ensured. Next, a Secure-Seal spacer with a diameter of 20 mm was attached to dust-free microscopy slides. After vortexing, 40 µL of the samples was added to the microscopy slides. A coverslip (#1,5 thickness) was carefully added to cover the sample. The microscopy slides were stored upside down at 4°C overnight to ensure that the liposomes would sediment.

The vapour nanobubble generation was checked at a range of laser pulse fluences for each sample. Movies of the formation of VNBs were acquired with the software package NIS-elements (Nikon) by imaging the sample with an EMCCD camera (Cascade II:512; Roper Scientifc, Tucson, AZ, USA). At the same time, the laser energies were recorded in order to match vapour nanobubble formation with applied laser energies. For every type of liposome and laser pulse energy, the recorded movies were analysed in terms of the amount of VNBs created. Next, the number of VNBs were plotted against laser pulse fluence for each type of liposome.

4.2.8 Determination of calcein encapsulation efficiency

4.2.8.1 *Calcein calibration curve*

Prior to measure the fluorescence intensity of calcein loaded liposomes, one must ensure that the detection method used for calcein measurement is applicable in terms of detection limit and sensitivity. Therefore, a calibration curve of the encapsulated fluorophore calcein was made where the fluorescence intensity was plotted against the calcein concentration. As described earlier, calcein shows self-quenching at higher concentrations (> 70 mM), whereas its fluorescence at lower concentrations is dequenched.[132] In this thesis, fluorescence intensities were measured with a fluorescence microplate reader (EnVision, PerkinElmer, Waltham, MA). Laserlight of a defined wavelength excites the sample. An excitation filter ensures, that only a monochromatic laserline reaches the sample. Fluorescence, emitted by the sample, is detected. An emission filter guarantees, that only emitted light is detected.[130]

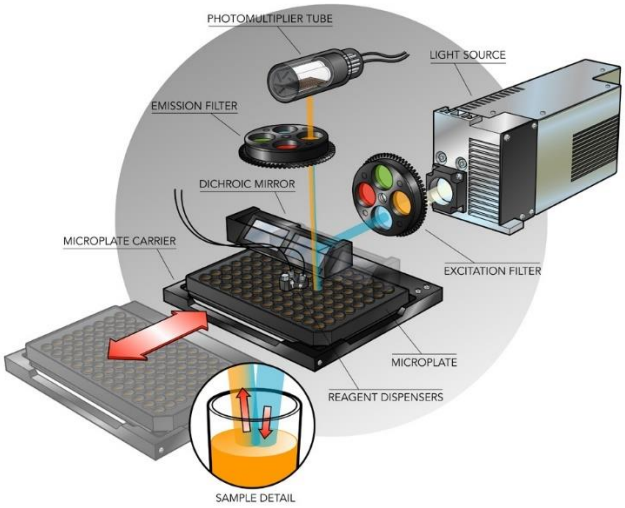

Figure 23: Scheme of a fluorescence microplate reader[156]

First, a dilution series of calcein was made in HEPES-buffer (20 mM, pH = 7,2) with concentrations ranging from 100 mM to 0,001 mM. Then, 50 µL of each calcein dilution was transferred to a black 96-well plate with plastic flat cover (Microplates for Life Science Research, PerkinElmer, Waltham, MA). To take into account the background fluorescence, the fluorescence of 50 µL HEPES buffer (20 mM, pH =7,2) was also measured. Each condition was measured in triplicate.

After positioning the appropriate excitation filter (λ_{exc} = 480 nm) and emission filter (λ_{em}= 515 nm), the 96 well-plate was inserted into the microplate reader without coverslip. The 96 well plate is shaken before the measurement for 5 seconds at 900 rpm following a 5 seconds delay.

4.2.8.2 *Calcein encapsulation efficiency*

To determine the percentage of encapsulated calcein inside both types of liposomes, calcein was fluorimetrically determined with a fluorimeter. To completely destroy the

liposomes, and thus release calcein out of the liposomes, Triton X-100 was added to the sample. Triton X-100 is a detergent which is often used as positive control in liposome release studies. Detergents can dissolve the phospholipid bilayer due to their amphiphilic structure[157,158] leading to leakage of calcein. AN-CAL-lipo, AN-HEP-lipo, CAT-CAL-lipo and CAT-HEP-lipo were prepared as shown in *Table 2*. A working solution was made by adding 500 µL HEPES-buffer to 100 µL of purified liposomal suspension (both for calcein-loaded liposomes and HEPES-buffer loaded liposomes). 50 µL of each working solution was solubilized with 10 µL of 10% Triton X-100. After incubation at room temperature for 15 minutes, 50 µL of the solubilized liposomes were transferred into a black 96 well-plate (PerkinElmer). The fluorescence intensity (λ_{exc} = 480 nm, λ_{em} = 515 nm) before and after solubilisation was measured via the Envision plate reader with the optimized protocol (*4.2.8.1 Calcein calibration curve*). For each type of liposome, the fluorescence was measured in triplicate. The background fluorescence was taken into account when calculating the encapsulation efficiency by measuring the fluorescence of the following controls: 50 µL of each type of "empty" liposome (without calcein) as well as 50 µL HEPES-buffer (20 mM, pH 7,2). The encapsulation efficiency can be calculated as follows:

$$E = 100\ \% - \frac{Fi - Fb}{Ft - Fbt} * 100\%$$

E= encapsulated calcein
F_i= initial fluorescence of purified liposomes
F_b= background fluorescence
F_t= fluorescence after addition of 10 µL Triton X-100
F_{bt}= background fluorescence after addition of 10 µL Triton X-100

Equation 4: Calculation of the encapsulation efficiency of calcein in nanoparticles[61]

4.2.8.3 Spontaneous calcein leakage

We also investigated if calcein could spontaneously diffuse out of the liposomes, hence if the fluorophore could leak out of the liposomes. Therefore, the fluorescence intensity of both CAT-CAL-lipo and AN-CAL-lipo was monitored over time with the fluorescence plate reader (Envision). The fluorescence intensity was measured every 10 minutes for 12 hours. The background fluorescence was taken into account by measuring fluorescence intensities of empty liposomes (without calcein) and HEPES-buffer. As positive control, liposomes solubilized with Triton X-100 were also measured.

4.2.9 Calcein release via pulsed laser trigger

As mentioned in *4.2.6.1 Functionalization of liposomes with Au-NPs*, two series of Au-NP-functionalized liposomes were synthesized for VNB-mediated calcein release. In the first batch, small Au-NPs of 10 nm and 100 mM calcein solution were entrapped inside the lumen of DOPC/DPPG liposomes. Next, two working solutions were made for further experiments: (1) 10 µL AN-CAL-Au-lipo and 9990 µL 20 mM HEPES buffer

(pH=7,2) and (2) 10 µL AN-HEP-Au-lipo and 9990 µL 20 mM HEPES buffer (pH=7,2). 50 µL of each working solution was irradiated once with a single laser pulse (561 nm, 100 µJ, pulse duration 7 ns, stage speed: 3000 µm/s)) as explained in *4.2.7.1 Generation and detection of VNBs around liposomes* and transferred into a Black 96-wellplate (PerkinElmer). As positive control, both working solutions were treated with 10 µL of 10 % Triton X-100 and after 15 min incubation time 50 µL were transferred into a Black 96-wellplate (PerkinElmer).

Pulsed laser treatment can damage the liposomal integrity. Therefore, the calcein release of 50 µL laser treated liposomes without Au-NPs (AN-CAL-lipo and AN-HEP-lipo) is measured in a 96 well plate. As calcein is sensitive to light, it might be bleached during the experiment. Therefore, the fluorescence intensity of 50 µL calcein solution (100 mM) after pulsed laser treatment was measured and taken into account as bleaching factor. The fluorescence intensity of released calcein was measured at (λ_{exc} = 480 nm, λ_{em} = 515 nm) via EnVision (PerkinElmer).

A second batch of liposomes consisted of DOPC/DPPG liposomes functionalized with 40 nm Au-NPs in the high coverage surface ratio. Prior to fluorescent imaging, eight different working solutions, as enlisted in *Table 7*, were prepared.

Working solution	Dilution
CAL WS 1	50 µL calcein 100 mM + 4950 µL HEPES buffer
CAL WS 2	10 µL CAL WS 1 + 990 µL HEPES buffer
HEPES WS 1	50 µL HEPES buffer + 4950 µL HEPES buffer
HEPES WS 2	10 µL HEPES WS 1 + 990 µL HEPES buffer
AN-CAL-lipo WS 1	50 µL AN-CAL-lipo + 4950 µL HEPES buffer
AN-CAL-lipo WS 2	10 µL AN-CAL-lipo WS 1 + 990 µL HEPES buffer
AN-HEP-lipo WS 1	50 µL AN-HEP-lipo + 4950 µL HEPES buffer
AN-HEP-lipo WS 2	10 µL AN-HEP-lipo WS 1 + 990 µL HEPES buffer

Table 7: Volumes of the working solutions used in the liposomal calcein release experiment

For each working solution, the fluorescence intensities were measured, as well as the fluorescence intensities of the corresponding controls with treatments as follows:

- 30 µL Triton 10 %
- 30 µL 40 nm Au-NPs
- 30 µL 40 nm Au-NPs + laser (561 nm, 80 µJ)
- 30 µL 40 nm Au-NPs+ 30 µL Triton 10 %
- 30 µL 10 nm Au-NPs
- 30 µL 10 nm Au-NPs+ laser (561 nm, 80 µJ)
- 30 µL 10 nm Au-NPs+ 30 µL Triton 10%
- Laser (561 nm, 80 µJ)

Therefore, 50 µL of all samples have been transferred to a black 96-wellplate (PerkinElmer). The fluorescence intensity of calcein was measured at (λ_{exc} = 480 nm,

λ_{em} = 515 nm) via the EnVision fluorescence microplate reader (PerkinElmer). All fluorimetric measurements have been performed in triplicates.

4.2.10 Determination of tobramycin encapsulation efficiency

4.2.10.1 *Tobramycin calibration curve*

To determine the efficiency of tobramycin encapsulation in liposomes, an agar diffusion test with *Bacillus subtilis* (ATCC 6633) was performed. A spore suspension of *B. subtilis* was grown for 7 days at 35 - 37 °C on antibiotic medium 1 supplemented with 0,001 g/L manganese sulphate ($MnSO_4$ x H_2O) according to European Pharmacopoeia. *B. subtilis* growth (mainly spores) was washed off using sterile water and the resulting suspension was heated at 70 °C for 30 min. The resulting suspension was then diluted in order to obtain a concentration of spores of 10^7 - 10^8 spores / mL and stored at 4 °C until further use. Afterwards, agar plates were prepared by making a 1 % suspension of spores (4 mL / 400 mL) in AM11 agar at 48 °C. 30 mL of the agar was poured into Petri dishes and left to solidify at room temperature for 20 minutes. Wells of 6 mm were cut into the agar and filled with 100 µL of sample or control. After incubating for 24 hours at 37 °C, inhibition zones were measured using a ruler.

To determine the encapsulation efficiency of tobramycin, the inhibition zones of different concentrations of tobramycin (80 mg/mL → 1 µg/mL) were measured according to this agar diffusion test. A calibration curve was set up by plotting inhibition zones against tobramycin concentrations.

4.2.10.2 *Tobramycin encapsulation efficiency*

To determine the amount of tobramycin inside liposomes, the inhibition zones of AN-TOBRA-lipo and NEU-TOBRA-lipo were measured via the above-mentioned agar diffusion method. To completely release tobramycin from the liposomes, 10% Triton X-100 was added to the liposomal samples. The inhibition zones of the following samples were taken into account: AN-HEP-lipo, NEU-HEP-lipo and 0,9% NaCl.

Also the potential detrimental effect of the used concentration of Triton X-100 on the survival of *Bacillus* subtilis was taken into account by measuring the inhibition zones of Triton X-100 control.

Liposomes have been prepared as previously described via TFH method. *Table 3* enlists the composition of liposomes used. For each batch the hydrodynamic size and the zeta potential were measured via DLS.

4.2.11 Bioactivity of liposome-encapsulated tobramycin against *Pseudomonas aeruginosa* biofilms

To test the antimicrobial activity of tobramycin loaded liposomes against bacterial biofilms, a *Pseudomonas aeruginosa* biofilm was cultured. A pure culture of *Pseudomonas aeruginosa* LESB58 was grown on Lysogeny Agar. After an incubation period of 24 hours at 37 °C, an overnight suspension was made by suspending the bacteria into 9 mL Lysogeny Broth. After another 24 hours during incubation at 37 °C in an orbital shaking incubator, the inoculum was standardized at 5 x 10^7 colony forming units/ mL. Biofilms were formed by filling 100 µL of each bacterial suspension in 96-well plates with microscopy bottom. After 4 hours of incubation at 37 °C, the adhered biofilm cells were washed with 100 µL 0,9 % NaCl (w/v) to remove the planktonic bacteria. The biofilm was covered with 100 µL medium and incubated at 37 °C. After 24 hours of biofilm formation, the media was removed and the biofilm was covered with 100 µL sample:

- 0,9 % NaCl (w/v)
- 16 µg/mL tobramycin
- AN-TOBRA-lipo (1:50 diluted)
- AN-TOBRA-lipo (1:50 diluted) + 10 nm Au-NPs
- HEPES buffer 20 mM
- Diluted 10 nm Au-NPs (2:1)
- AN-HEP-lipo (1:50 diluted)

Liposomes (AN-TOBRA-lipo, AN-HEP-lipo) have been prepared as previously described via TFH method. *Table 3* enlists the composition of liposomes used.

Next, laser treatment was performed (wavelength: 561 nm, laser energy: 120 µJ, stage speed: 3000 µm / s) in order to create vapour nanobubbles. After incubation at 37 °C for 24 hours, the amount of colony forming units was determined by plate counting, depicted in *Figure 24*.

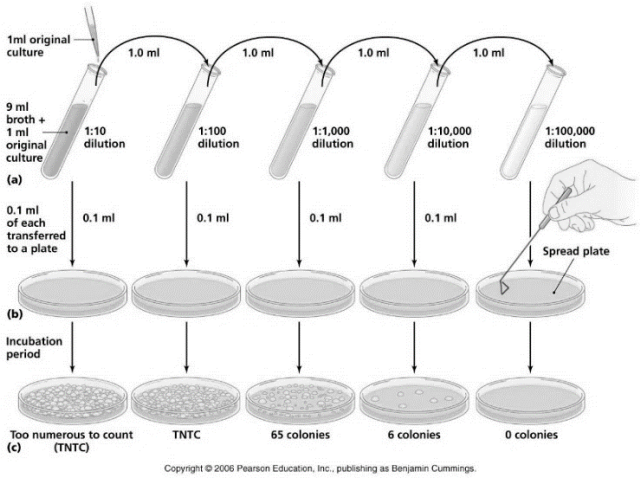

Figure 24: Scheme of plate counting

For the next experiment, the protocol mentioned above was optimized in terms of incubation time. After washing with 0,9 % NaCl (w/v), a *P.aeruginosa* biofilm was treated with 100 µL of following samples:

- 0,9 % NaCl (w/v)
- 16 µg/mL tobramycin
- NEU-TOBRA-lipo (1:50 diluted))
- NEU-TOBRA-lipo (1:50 diluted) + 40 nm Au-NPs
- HEPES buffer 20 mM
- Diluted 40 nm Au-NPs (2:1)
- NEU-HEP-lipo (1:50 diluted)

Liposomes (NEU-TOBRA-lipo, NEU-HEP-lipo) have been prepared as previously described via TFH method. *Table 3* enlists the composition of liposomes used. However, instead of 24 hours, biofilms were only incubated for 15 minutes with the different samples. Afterwards, a laser treatment was performed (wavelength: 561 nm, laser energy: 120 µJ, stage speed: 3000 µm / s) in order to create vapour nanobubbles. After incubation at 37 °C for 24 hours, the amount of colony forming units was determined by plate counting, depicted in *Figure 24*.

5 Results and Discussion

5.1 Localization of liposomes inside biofilms

The aim of this experiment was to determine the effect of surface charge and the presence of PEG-chains in the liposomal composition on the localization of liposomes inside bacterial biofilms.

5.1.1 Characterisaton of liposomes

5.1.1.1 *Non-pegylated liposomes*

First of all, CAT-lipo and NEU-lipo were prepared. After preparation, the liposomes were diluted (1:100) in HEPES-buffer and measured via DLS. The average intensity-based diameter of CAT-lipo was 126,5 nm. In case of NEU-lipo, the samples became more polydisperse, as depicted by the higher Polydispersity Index (PDI) of 0,443.

	z-average (nm)	Intensity (%)	PDI	Average of size (nm) ± standard deviation (nm)
CAT-lipo	125,5	95,7	0,358	126,5 ± 1
	128,0	100	0,332	
	126,0	100	0,329	
NEU-lipo	198,1	92,3	0,358	210,6 ± 11,1
	225,1	81,3	0,473	
	208,5	84,7	0,499	

Table 8: DLS results of positively CAT-lipo and slightly negatively charged NEU-lipo. The z-average and the PDI were measured after preparation of the liposomes**.**

This could also be observed in the distribution of the liposomal sizes (*Figure 25*) by the emergence of a small population of bigger sized particles. Also, the mean intensity-based diameter increased to 210,6 nm.

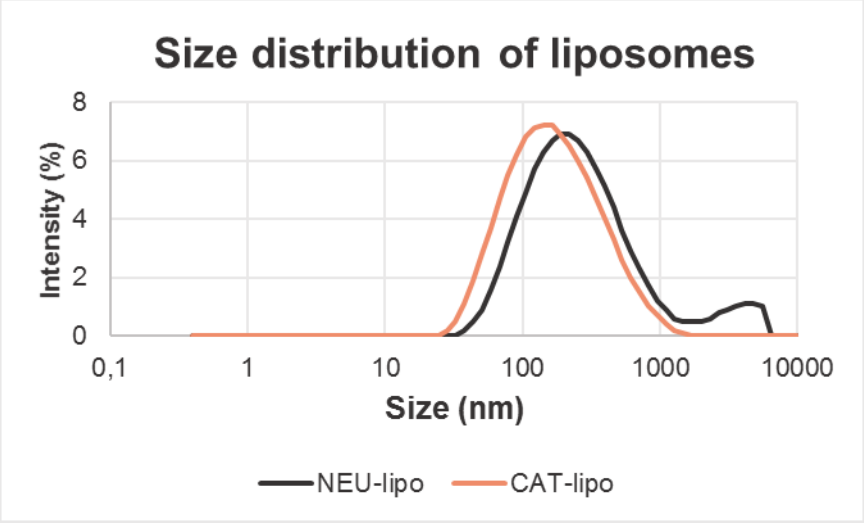

Figure 25: Comparison of the size distribution of NEU-lipo and CAT-lipo

The surface charge is represented by the zeta potential and is measured via DLS (*Figure 26*). For the preparation of positively charged liposomes, the cationic lipid DOTAP was included in the liposomal formulation.

	Zeta potential (mV)	Average of zeta potential (mV) ± standard deviation
CAT-lipo	33,2	29,5 ± 2,6
	27,2	
	28,0	
NEU-lipo	-3,70	-1,6 ± 1,5
	-0,85	
	-0,23	

Table 9: DLS results of CAT-lipo and NEU-lipo. The zeta potential was measured after preparation of the liposomes.

The measured zeta potential of CAT-lipo was 29,5 mV proving the presence of DOTAP in the liposomal bilayer. The presence of cholesterol accounts for the slightly negative zeta-potential of the NEU-lipo. The results of the zeta potential measurements can be found in *Table 9.*

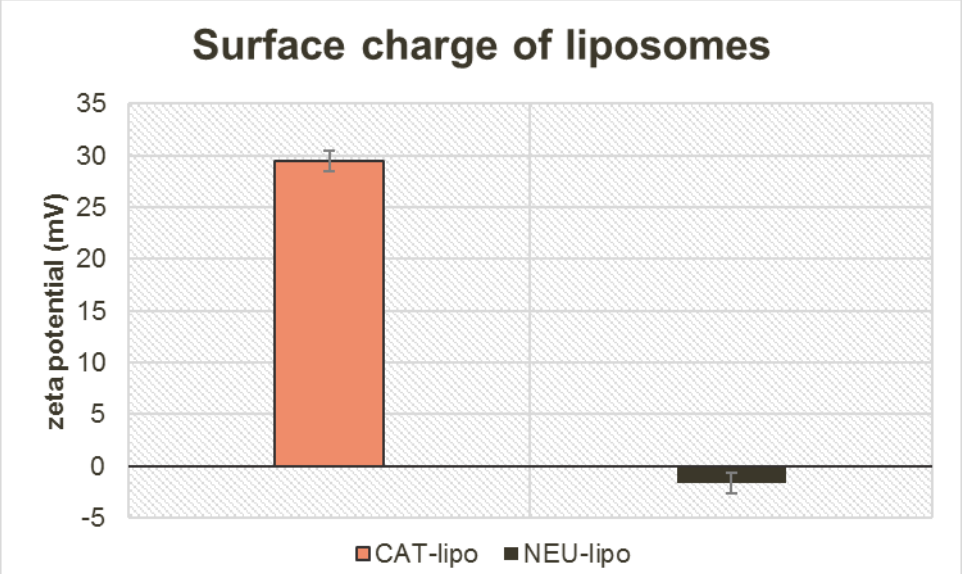

Figure 26: Comparison of zeta potential of positively (CAT-lipo) and slightly negatively (NEU-lipo) charged liposomes.

5.1.1.2 *Pegylated liposomes*

Inclusion of PEG-chains causes steric hindrance between the liposomes as well as shielding of surface charge.[5] The aim of this experiment was to investigate if the penetration of liposomes through biofilms could be improved if their outer surface was decorated with PEG-chains. Therefore, two different types of pegylated lipids were added to the formulation. The exact amounts are given in *Table 1*.The size and the zeta potential of the liposomes have been measured via DLS.

	Ø z-average (nm)	Ø Intensity (%)	Ø PDI
CAT-lipo	126,5	98,6	0,339
CAT-PEG-lipo	147,4	87,0	0,564
CAT-Cer-PEG-lipo	65,6	85,8	0,856
NEU-lipo	210,3	86,1	0,443
NEU-PEG-lipo	174,0	92,0	0,335
NEU-Cer-PEG.lipo	148,0	93,9	0,627

Table 10: DLS results of positively and slightly negatively charged liposomes with or without different PEG-chains. PEG= DSPE-PEG 2000, Cer-PEG= C8 PEG2000 ceramide

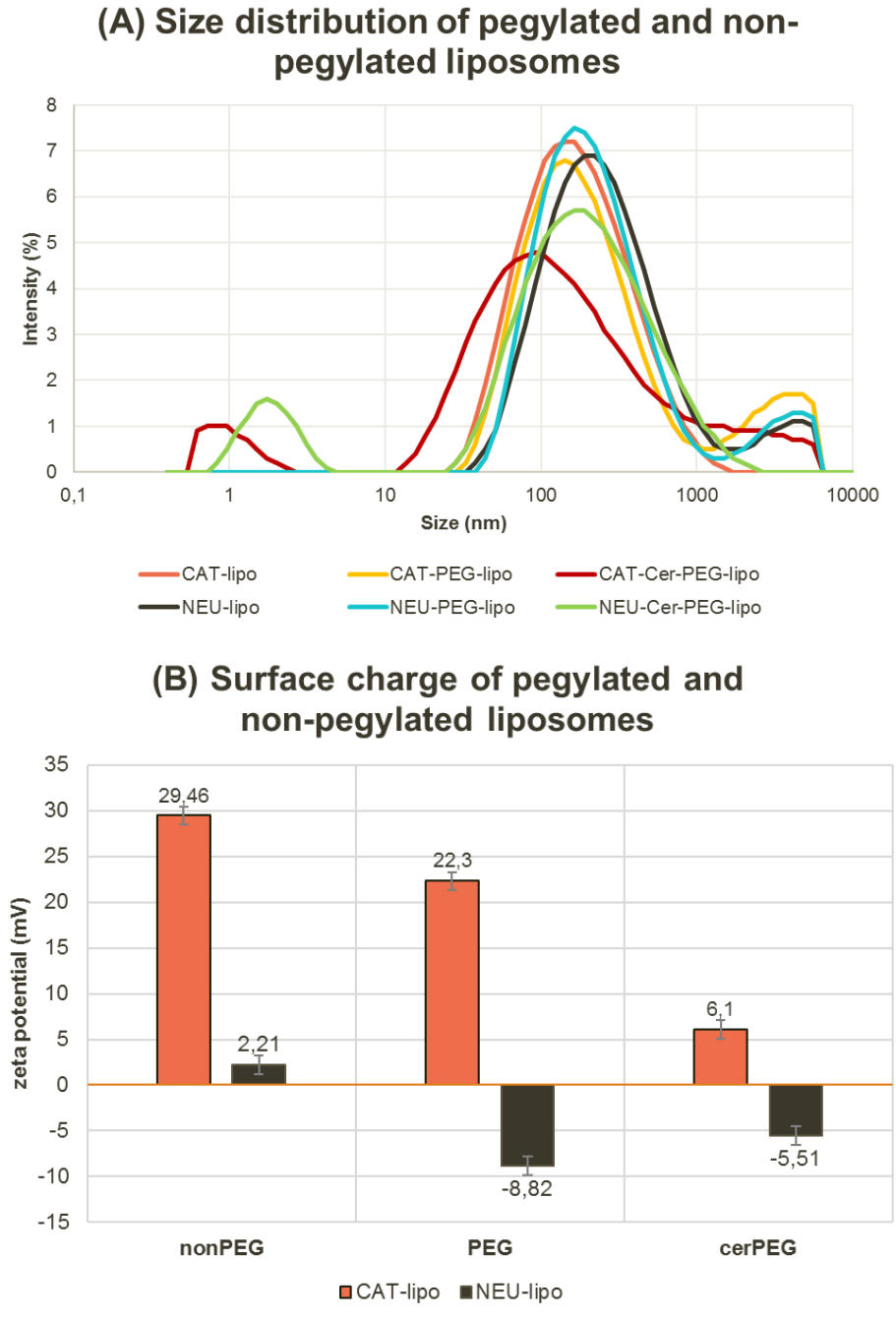

Figure 27: Comparison of the size distribution (A) and the surface charge (B) of positively and slightly negatively charged liposomes with and without Pegylation.

Figure 27 shows the size distribution of pegylated and non-pegylated liposomes as well as their surface charge. As already discussed above, in case of PEGylation, one can observe the emergence of a small population of bigger sized particles, as depicted by higher PDI values. This can be related to agglomeration of particles or insufficient pegylation.

The surface charge of positively and negatively charged liposomes are represented in *Figure 27*. CAT-lipo have a zeta potential around 29,5 mV. Inclusion of PEG-chains shows a decrease of surface charges depicted by the zeta potential values of 22,3 mV for CAT-PEG-lipo and 6,1 mV for CAT-Cer-PEG-lipo. This could also be observed for slightly negatively charged liposomes. NEU-lipo have a zeta potential of 2,21 mV, whereas NEU-PEG and NEU-Cer-PEG have values of -8,82 mV and -5,51 mV. The decreasing surface charge is attributed to the negative surface charge of PEG-chains.

5.1.1.3 *Determination of liposomal concentration*

To determine the liposomal concentration fluorescence single particle tracking (fSPT) was used. The experiment was performed as described *in 4.2.3.2 Fluorescence Single Particle Tracking* In order to calculate the liposomal concentration, following parameters were required:

Parameter	Value
Max step	34
Min track	3
Pix size (µm)	0,079
Frames/s	20,69
Diameter (nm)	60
Temperature (°C)	22,5
Viscosity (kg/m.s)	0,94

Table 11 Required parameters for the SPT analysis; max.step was calculated with the max step advisor prior to analysis

The final liposomal concentration is 3,50 x 10^{12} liposomes per mL (±2,50 x 10^{11} liposomes / mL).

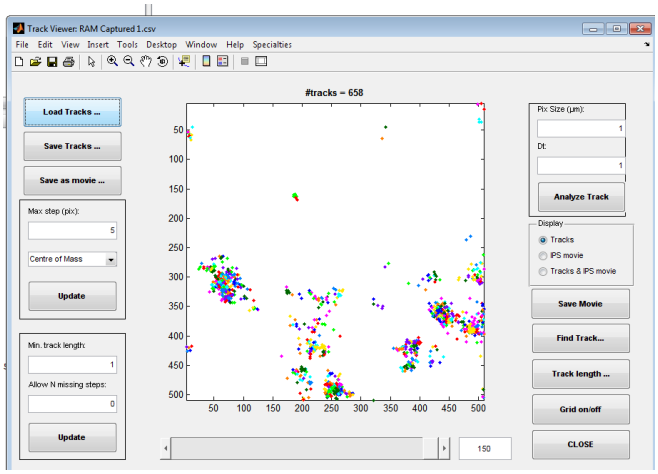

Figure 28: Calculation of the trajectories during SPT analysis

5.1.2 Localization inside biofilms

In *Figure 29* CAT-lipo, CAT-PEG-lipo and CAT-Cer-PEG-lipo were added to a biofilm of *B. multivorans* whereas in *Figure 30* they were added to a *P. aeruginosa* biofilm. The biofilm was prepared as described in *4.2.5 Experimental set-up for visualization experiment*. Bacteria are green due to the SYTO dye (488 nm) and liposomes are displayed in red (647 nm) due to the added DiD.

In *Figure 31* NEU-lipo, NEU-PEG-lipo and NEU-Cer-PEG-lipo were added to a biofilm of *B. multivorans***.** *Figure 32* displays these liposomes in a biofilm of *P. aeruginosa*. Red (647 nm) represents the liposomes and green (488 nm) shows the bacterial clusters. All experiments were performed in triplicate.

Different pictures were taken for each combination of liposomes and biofilms with a confocal microscope. Pictures were taken at different positions in the biofilm to see whether the liposomes were able to penetrate the bacterial biofilms and pass through the biofilm matrix. Because a biofilm is a complex 3D architecture composed of dense cell aggregates of 10 - 100 µm in size surrounded by a sticky biofilm matrix, it was not sufficient to make an image at only 1 z-position per x/y-location. To make a valid conclusion, extensive z-stacks were taken per x/y-location at different z-layers from the bottom to the top of the biofilm.

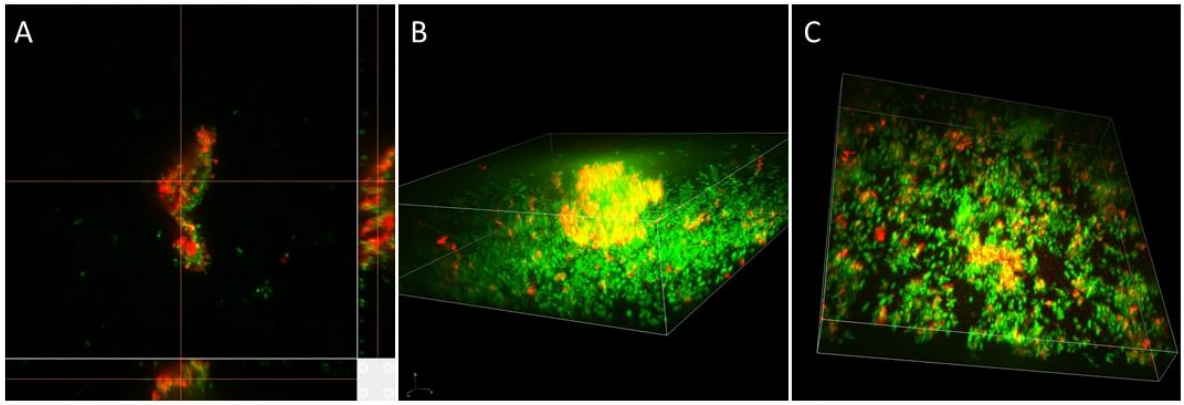

Figure 29: (A) CAT-lipo in *B. multivorans*: ø Liposomal size = 126,5 nm, ø liposomal zeta potential = 29,5 mV, Z- range = 10,55 µm, Z-step = 0,3 µm **(B) CAT-PEG-lipo**: Ø liposomal size=147,4 nm, ø liposomal zeta potential = 22,3 mV, Z-range= 25,50 µm, z-step= 0,300 µm, Width= 93,70 µm, Height= 93,70 µm, Depth= 25,50 µm **(C) CAT-Cer-PEG-lipo**: ø Liposomal size= 65,57 nm, ø liposomal zeta potential= 6,11 mV, Z-range= 25,50 µm, z-step= 0,300 µm, Width= 93,70 µm, Height= 93,70 µm, Depth= 12,60 µm

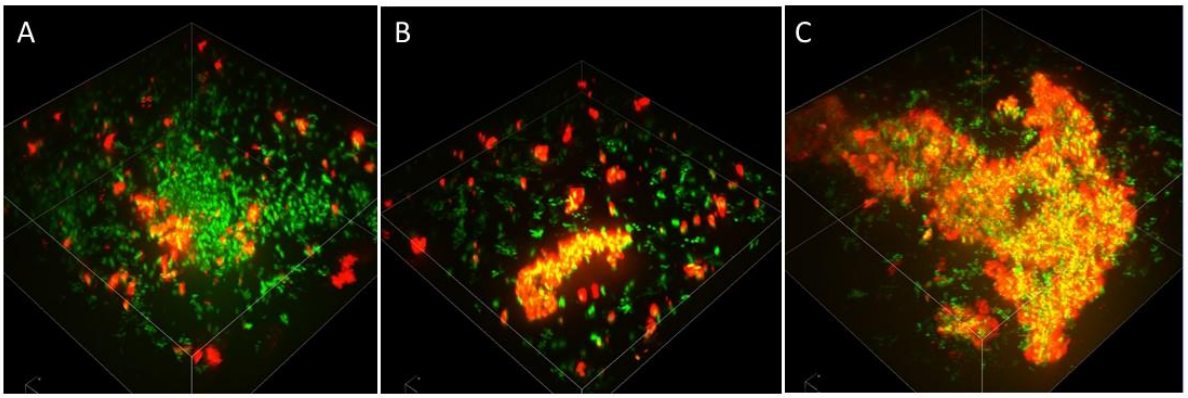

Figure 30: (A) CAT-lipo in *P. aeruginosa*: ø Liposomal size = 126,5 nm, ø liposomal zeta potential= 29,5 mV, Z-range= 40,03 µm, z-step= 0,300 µm, Width= 93,70 µm, Height= 93,70 µm, Depth= 40,20 µm, **(B) CAT-PEG-lipo in *P. aeruginosa:*** Ø liposomal size= 147,4 nm, ø liposomal zeta potential = 22,3 mV, Z-range= 12,95 µm, z-step= 0,300 µm, Width= 93,70 µm, Height= 93,70 µm, Depth= 13,20 µm, **(C) CAT-Cer-PEG lipo in *P. aeruginosa***: ø Liposomal size= 65,57 nm, ø liposomal zeta potential = 6,11 mV, Z-range= 50,32 µm, z-step= 0,300 µm, Width= 93,70 µm, Height= 93,70 µm, Depth= 50,40 µm

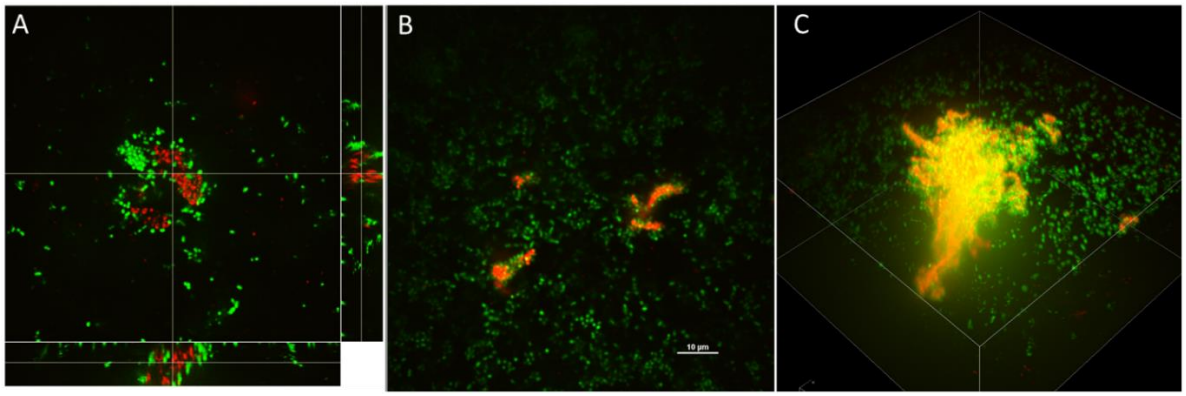

Figure 31: (A) NEU-lipo in *B. multivorans*: ø Liposomal size = 210,6 nm, ø liposomal zeta potential = -2,20 mV, Z-range= 11,78 µm, z-step= 0,300 µm, **(B) NEU-PEG-lipo in *B. multivorans***: ø Liposomal size= 173,96 nm, ø liposomal zeta potential = -8,81 mV, Z-range= 10,90 µm, z-step= 0,300 µm, **(C) NEU-Cer-PEG lipo in *B. multivorans***: ø Liposomal size = 106,2 nm, ø liposomal zeta potential = -5,51 mV, Z-range= 49,40 µm, z-step= 0,300 µm, Width= 93,70 µm, Height= 93,70 µm, Depth= 49,50 µm

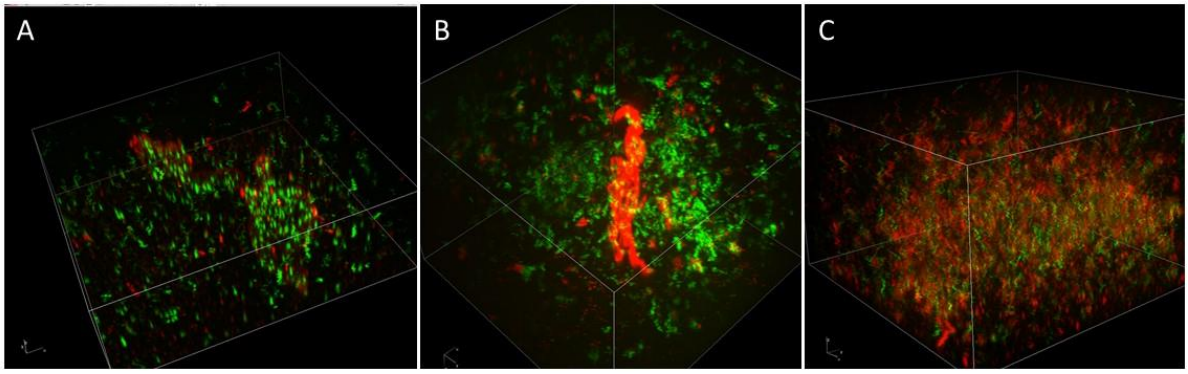

Figure 32: (A) NEU-lipo in *P. aeruginosa*: ø Liposomal size = 259,3 nm, ø liposomal zeta potential = -1,59 mV, Z-range= 28,88 µm, z-step= 0,300 µm, Width= 93,70 µm, Height= 93,70 µm, Depth= 29,10 µm, **(B) NEU-PEG-lipo *in P. aeruginosa***: ø Liposomal size= 173,96 nm, ø liposomal zeta potential = -8,81 mV, Z-range= 67,85 µm, z-step= 0,300 µm, Width= 93,70 µm, Height= 93,70 µm, Depth= 68,10 µm, **(C) NEU-Cer-PEG lipo in *P. aeruginosa***: ø Liposomal size = 148 nm, ø liposomal zeta potential = -4,04 mV, Z-range= 54,85 µm, Z-step= 0,300 µm, Width= 93,70 µm, Height= 93,70 µm, Depth= 54,90 µm

Different z-stacks were evaluated visually. *Figure 29 (A)* shows highly positively charged liposomes stuck on the top of a *B. multivorans* biofilm. A similar trend was observed for CAT-lipo in a *P. aeruginosa* as depicted by *Figure 30***.** Both unpegylated positively charged liposomes got stuck on top of the bacterial-produced polymer matrix. By shielding the surface charge of liposomes via PEG-chains, liposomes should be able to penetrate deeper into the biofilm. As depicted by the bright red channel in *Figure 29 (B)* and *Figure 30 (C)* the penetration of pegylated liposomes (CAT-PEG-lipo and CAT-Cer-PEG-lipo) is enhanced. Surprisingly, liposomes including C8-PEG2000 Ceramide showed more association as well as agglomeration close to bacterial clusters. This might be due to the fact, that Ceramide can diffuse out of the liposomal bilayer after interaction with biological membranes leaving more liposomes close to bacterial cells.

Figure 31 (A) and *Figure 32 (A)* show the penetration of slightly negatively charged liposomes (NEU-lipo) through above mentioned biofilms. Similar to CAT-lipo, NEU-lipo are stuck on the surface of biofilm bacteria (*Figure 32 (A)*). While the inclusion of PEG-chains decreases the zeta potential, NEU-PEG-lipo show more penetration through the biofilms of *P. aeruginosa* and *B. multivorans* compared to NEU-lipo (*Figure 31 (B), Figure 32 (B)).* Interestingly, the inclusion of Cer-PEG-chains into the liposomal formulation (NEU-Cer-PEG-lipo) improved the interaction between liposomes and bacteria more than NEU-PEG-lipo (*Figure 31 (C), Figure 32 (C)*), which might be due to the sheddable coat as explained earlier. This trend was similar for the other investigated samples.

Unpegylated liposomes (CAT-lipo and NEU-lipo) showed no penetration through biofilms, whereas pegylated liposomes improved the penetration of liposomes through biofilms. A possible explanation for this trend might be an interaction of unpegylated liposomes with the extracellular matrix produced by bacteria in biofilms. Due to its

multiple components, not only positively but also negatively charged molecules are prone to show interaction. Extracellular DNA is often found in the extracellular matrix of different types of biofilms such as *P. aeruginosa* biofilms. eDNA is a negatively charged component because of the presence of phosphate groups, and could therefore electrostatically bind to positively charged liposomes, hence be responsible for entrapment of liposomes and their hindered diffusion. Extracellular matrix of biofilms often contains amino acids, that are positively charged. Due to electrostatical interaction, negatively charged liposomes could be entrapped hence their diffusion hindered.

Another reason for the limited penetration might be the liposomal size, as the size is a crucial parameter for penetration. Forier et al.[19] have proven, that particles bigger than 200 nm show less penetration than particles less than 200 nm. Intensity based diameters of 210,6 nm might outrun the penetration limit in terms of size. In further experiments, a reduction of liposomal sizes could be tested to investigate the penetration limit.

5.2 Use of VNBs as trigger for liposomal calcein release

The aim of this experiment was to investigate if calcein can be released from liposomes by closely associated vapour nanobubbles. By decorating the surface of calcein loaded liposomes with Au-NPs, vapour nanobubbles were created nearby the liposomes upon pulsed laser irradiation. The capability of VNBs to trigger the release of calcein was investigated by measuring calcein fluorescence before and after pulsed laser irradiation.

5.2.1 Characterization of liposomes

We evaluated the potential of two different types of liposomes in their capability to encapsulate calcein. Positively charged liposomes were made by incorporating the lipids DOTAP and DOPE in the formulation, while DOPC/DPPG liposomes were made to represent negatively charged liposomes. As a control, also ‘empty’ liposomes containing HEPES-buffer were included in the assay. The exact composition is given in *Table 2***.** The hydrodynamic diameter and zeta potential of all formulations were measured by DLS (*Table 12*) before and after gel filtration included as a purification step. In case of positively charged liposomes, a polydisperse sample was obtained, which is evidenced by a PDI = 0,753. The size distribution, displayed in *Figure 34 and Figure 35*, also shows the emergence of big aggregates in case of positively charged calcein-encapsulating liposomes. These results could be expected as extensive aggregation could be observed in the round bottomed flask during liposome preparation. This is probably due to electrostatic interaction as the positive charge of

DOTAP interacted with the negatively charged calcein. This led to irreversible aggregation, which is shown at *Figure 33*.

Figure 33: Round bottomed flask during preparation of CAT-CAL-lipo. Aggregation on the side wall is clearly visible.

A PDI value of 0,753 also depicts the aggregation. AN-CAL-lipo, as well as CAT-HEP-lipo and AN-HEP-lipo, whose size measurements are concluded in *Table 12***,** were further examined.

	Ø z-average (nm)	Ø Intensity (%)	Ø PDI	Zeta potential (mV)
CAT-CAL-lipo	1532	56,6	0,753	-10,1
CAT-HEP-lipo	104,9	96,2	0,295	40,4
AN-CAL-lipo	312,4	68,6	0,437	-56,8
AN-HEP-lipo	103,3	95,9	0,309	-33,8

Table 12: DLS results of positively and negatively charged liposomes encapsulated with 100 mM calcein solution or HEPES-buffer.

On the other hand, in case of negatively charged liposomes, the average intensity-based diameter of calcein loaded and control liposomes were 312 nm (PDI = 0.4) and 100 nm (PDI = 0.3) respectively. We can conclude that DOPC/DPPG liposomes loaded with calcein/HEPES-buffer are more monodisperse and have more desirable sizes (range of 100 to 300 nm) than the DOTAP/DOPE liposome counterparts.

The surface charge is represented by the zeta potential and is measured via DLS before and after the gel filtration, which is used to purify liposomes (*Figure 36*). For the preparation of positively charged liposomes, the cationic lipid DOTAP was included in the liposomal formulation. The measured zeta-potential of CAT-HEP-lipo was 40,4 mV, proving the presence of DOTAP in the liposomal bilayer. However, CAT-CAL-lipo showed a zeta potential of -10,1 mV. As described earlier, the combination of positively charged liposomes and negatively charged calcein led to aggregation. As there is no intact liposomal bilayer, the zeta potential is influenced by the negatively charged calcein. For the preparation of negatively charged liposomes, the anionic lipid DPPG

is used. The measured zeta potential of calcein-loaded and control liposomes was -56,8 mV and -33,8 mV.

The zeta potential of AN-CAL-lipo is more negative than the zeta potential of AN-HEP-lipo because calcein is highly negatively charged and has an impact on the liposomal bilayer. As stated earlier, calcein is difficult to encapsulate. To conclude, negatively charged liposomes loaded with calcein or HEPES-buffer are more favourable due to their more desirable sizes and surface charges than the DOTAP/DOPE liposome counterparts.

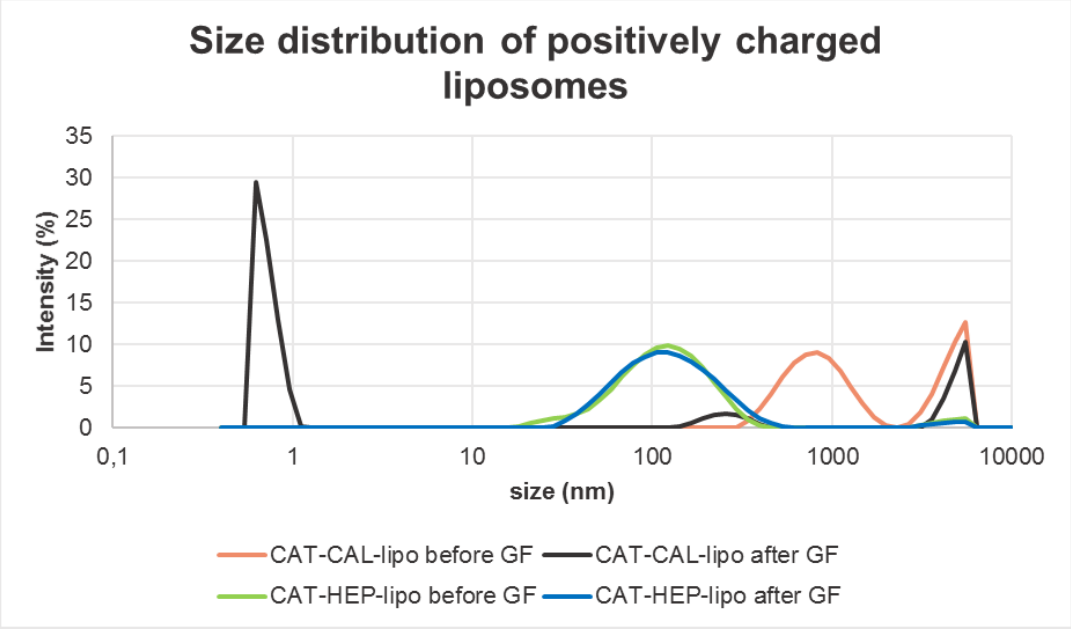

Figure 34: Size distribution of positively charged liposomes with calcein or HEPES-buffer encapsulated; before and after Gelfiltration (GF)

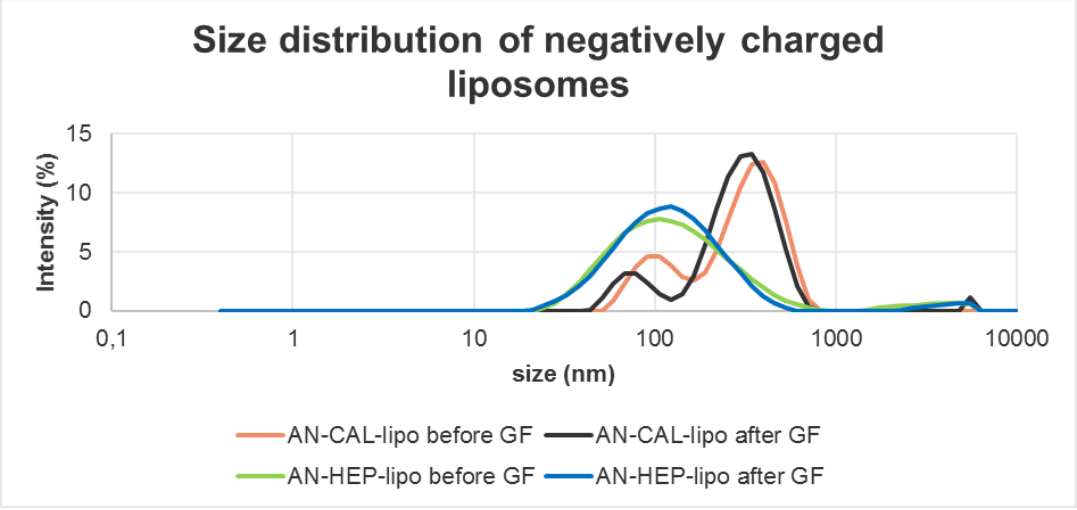

Figure 35: Size distribution of negatively charged liposomes with calcein or HEPES-buffer encapsulated; before and after Gelfiltration (GF)

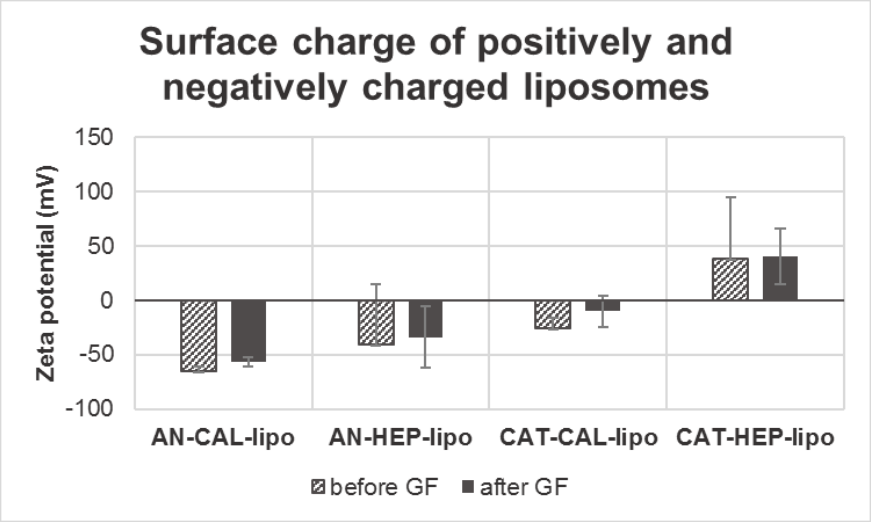

Figure 36: Comparison of the zeta potential of positively and negatively charged liposomes; before and after Gelfiltration (GF)

5.2.2 Functionalization of liposomes with Au-NPs

To render liposomes light-sensitive, noble metals like gold can be introduced to the construct. Surface plasmon resonance might increase local temperatures that might lead to leakage of liposomes hence to calcein release. In this diploma thesis, two types of Au-NP functionalized liposomes were synthesized. The first batch of liposomes consisted of DOPC/DPPG liposomes with calcein and 10 nm Au-NPs encapsulated inside the core.

	Ø z-average (nm)	Ø Intensity (%)	Ø PDI	Zeta potential (mV)
AN-CAL- low Au-lipo	194,2	89,4	0,404	-57,8
AN-CAL-high Au-lipo	162,1	93	0,346	-53,5
AN-CAL-lipo	169,4	98,5	0,26	-68,5

Table 13: DLS results of negatively charged liposomes encapsulated with a low (2,4% (v/v)) and a high (25% (v/v)) number of golden NPs

The hydrodynamic diameter of AN-CAL-low Au-lipo was 194,2 nm (PDI 0,404). AN-CAL-high Au-lipo had an intensity based diameter of 162,1 nm (PDI 0,346). Both kinds of liposomes were highly negatively charged due to the addition of DPPG to the liposomal bilayer. The zeta potential for AN-CAL-low Au-lipo was -57,8 mV and for the AN-CAL-high Au-lipo -53,5 mV. Due to the increased amount of positively charged golden NPs incorporated in AN-CAL-high Au-lipo the zeta potential is more positive.

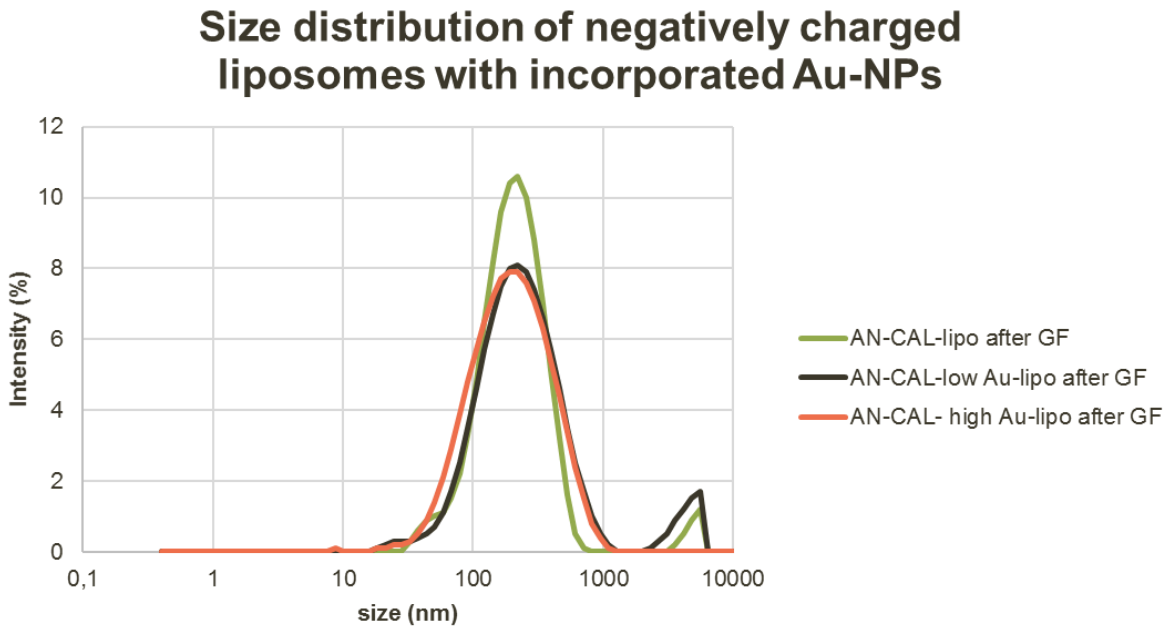

Figure 37: Comparison of the size distribution of liposomes with a low and a high amount of gold encapsulated

Comparing Au-NPs containing liposomes to blank liposomes (AN-CAL-lipo), we can distinguish no difference in the intensity based diameters and the zeta potentials, which are all highly negative.

The second batch of liposomes consisted of DOPC/DPPG liposomes of which the surface was decorated with different ratios of gold. Golden nanoparticles were synthesized as described in *4.1 Materials*. 40 nm Au-NPs used had a concentration of 2,6 x 10^{10} NPs/mL, whereas 10 nm Au-NPs had a concentration of 1,9 x 10^{14} NPs/mL (1:10 dilution). Both were positively charged.

The surface charge and hydrodynamic size of all functionalized liposomes was measured via DLS. Due to positively charged golden nanoparticles, the initial highly negative charge of liposomes was expected to become more positive as the number of golden nanoparticles attached to the surface increased. Two distinct sizes of Au-NPs were measured: 10 nm and 40 nm. *Figure 38* and *Figure 39* show the surface charge conversion of the liposomal constructs from a negative zeta potential (naked liposomes without Au-NPs) to a more and more positive zeta potential as more and more positive Au-NPs were attached.

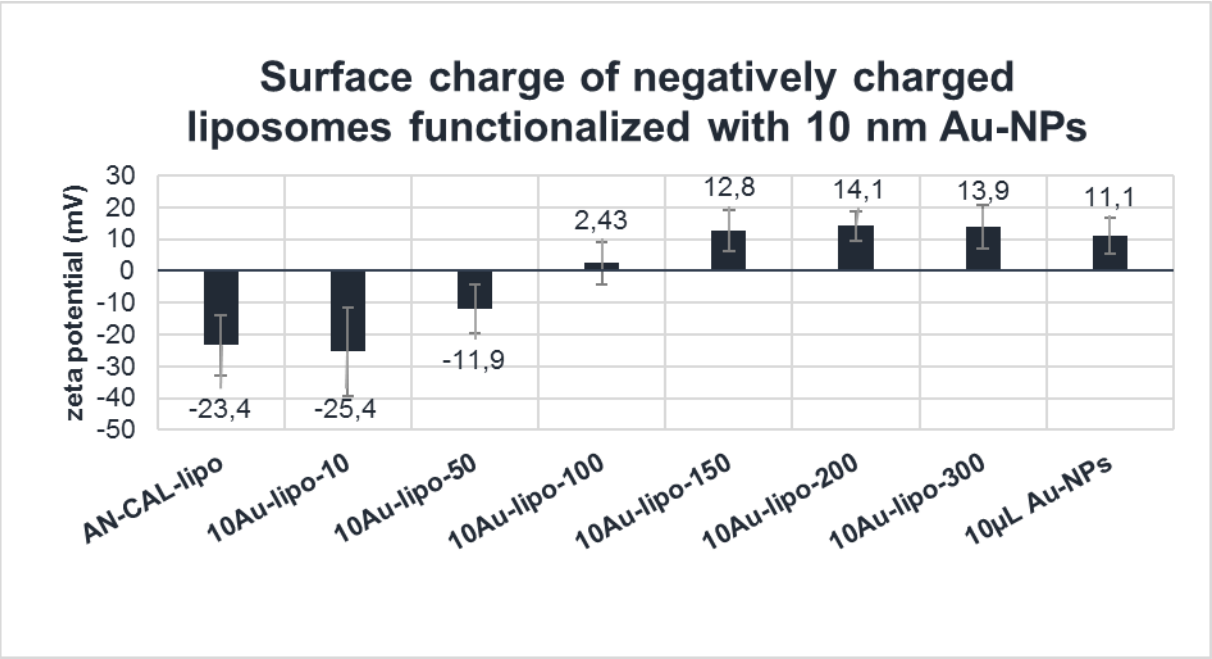

Figure 38: Surface charge inversion of AN-CAL-lipo with different ratios of 10 nm Au-NPs

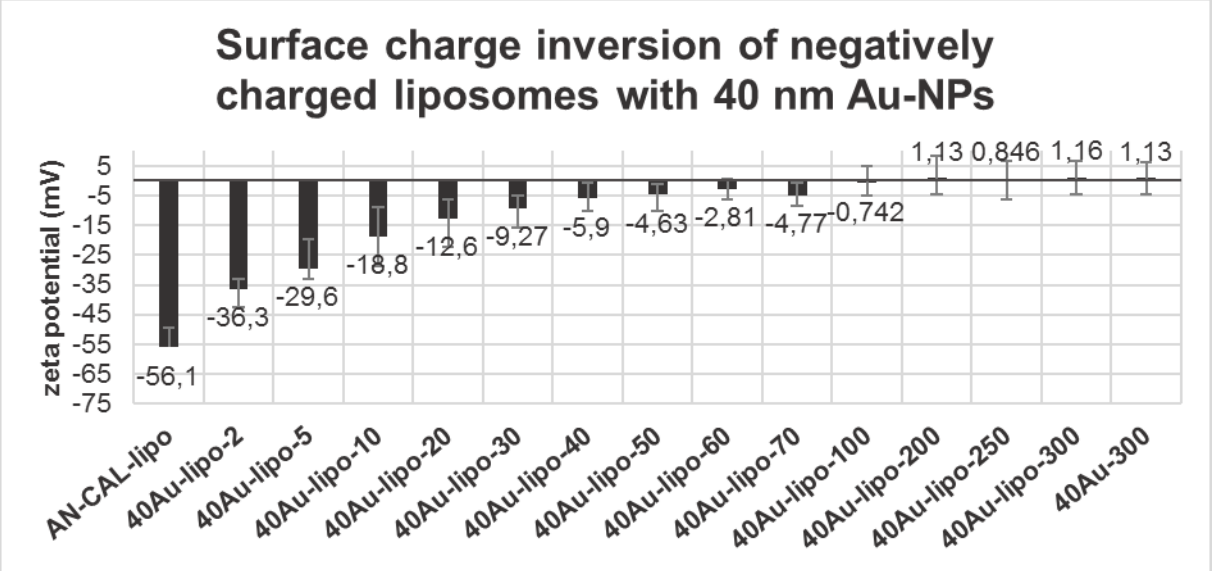

Figure 39: Surface charge inversion of AN-CAL-lipo with different ratios of 40 nm Au-NPs

5.2.3 Determination of VNB generation threshold

Based upon the previous experiment, distinct ratios of 10 nm and 40 nm Au-NPs to liposomes were chosen for determining the VNB generation threshold energies. VNBs were generated as described in *4.2.7.1. Generation and detection of VNBs around liposomes*, whereas the VNB formation has been confirmed visually as depicted in *Figure 40*.

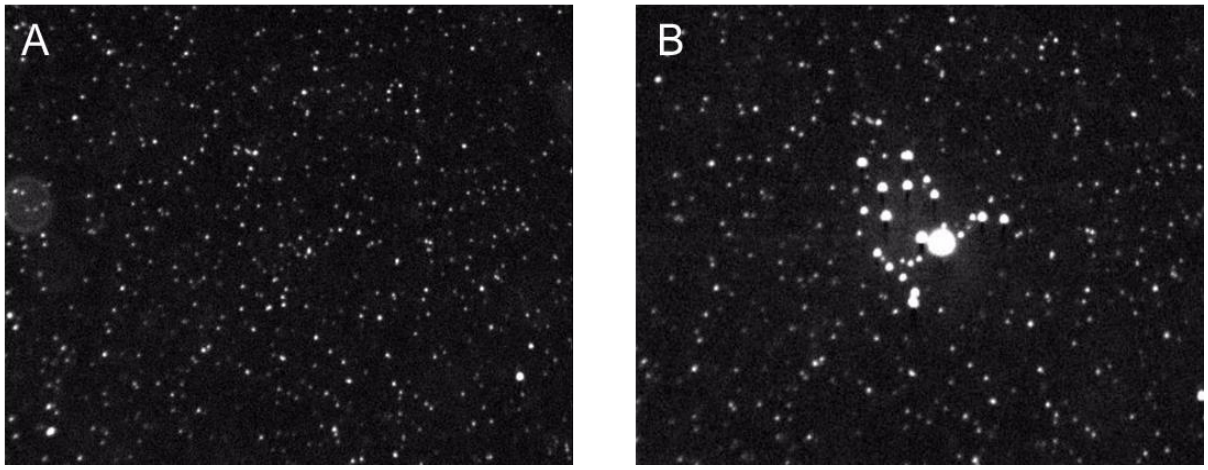

Figure 40: Darkfield microscopy image confirming the formation of a VNB. A) before the laser pulse, B) after the laser pulse

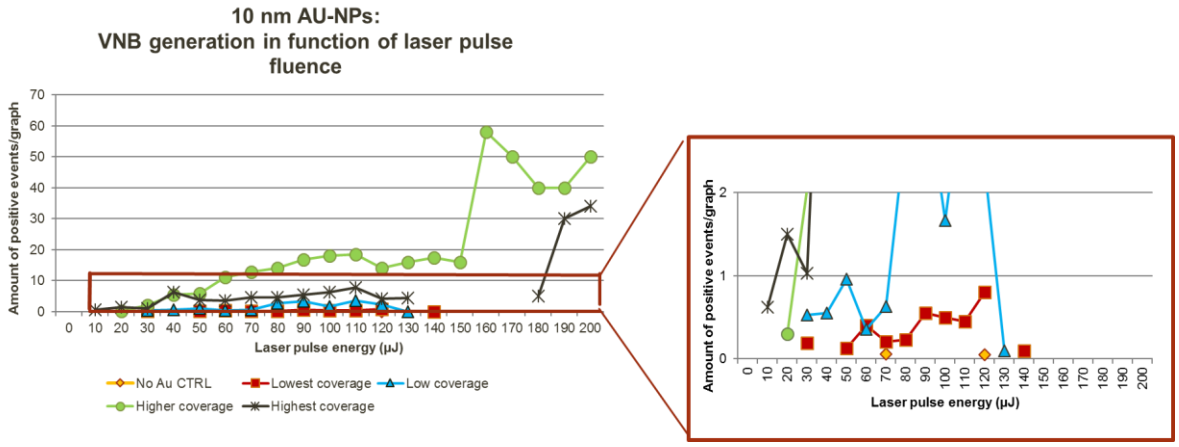

Figure 41: VNB generation in function of laser pulse fluence. 10 nm Au-NP functionalized liposomes

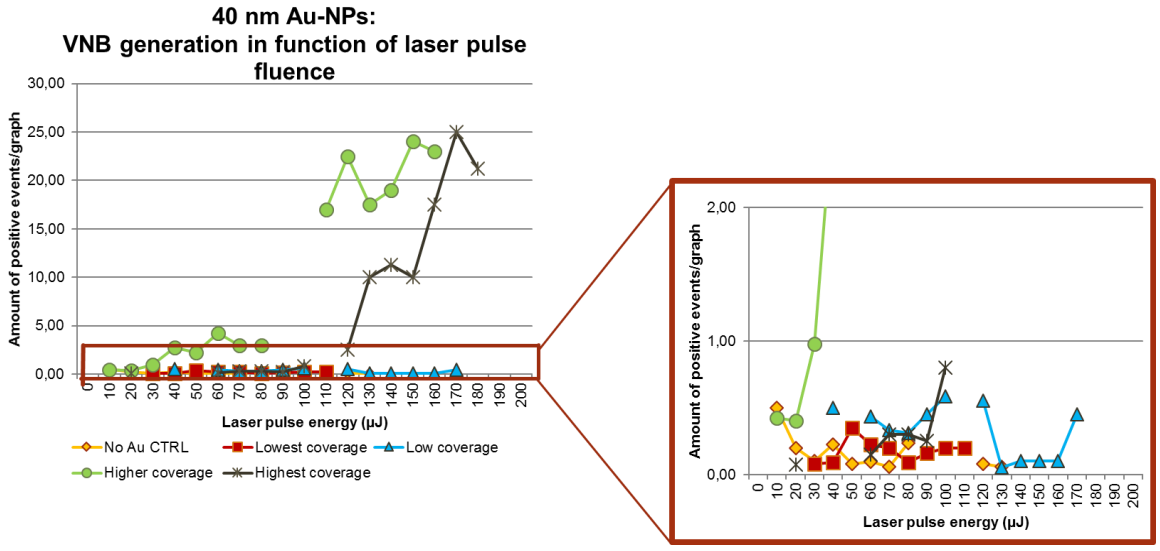

Figure 42: VNB generation in function of laser pulse fluence 40 nm Au-NPs functionalized liposomes

Analysing the movies in terms of required energy to create bubbles, a diagram, shown in *Figure 41 and Figure 42*, was designed. These diagrams show the number of bubbles that are formed for every laser pulse energy.

As expected, no bubbles occur without addition of golden nanoparticles. So, no VNBs occur in the CTRL samples. In the lowest surface coverage samples, no bubbles are created in both the samples with 10 nm as well as 40 nm Au-NPs. For both 10 nm and 40 nm functionalized liposomes, high surface coverage resulted in emergence of VNBs starting from laser pulse energy 30 µJ. Moreover, the amount of VNBs increased with increasing laser pulse energies. However, due to technical difficulties, not all energy levels could be tested for VNB generation in the previous experiment.

Therefore, the experiment should be repeated in order to fully cover all energy levels, so that the threshold laser fluence for VNB generation can be calculated. Because the highest amount of vapour nanobubbles was seen in the dark field microscopy videos of the high coverage samples, those samples were chosen for further testing in the calcein release studies.

5.2.4 Determination of calcein encapsulation efficiency

5.2.4.1 *Calcein calibration curve*

Low concentrated calcein is strongly fluorescent, whereas in higher concentration it shows self-quenching due to short range interactions between the fluorophore and its environment.[130] The fluorescence of different dilutions of calcein (both above and below the self-quenching concentration) was measured with a fluorimeter. In *Figure 43*, calcein fluorescence is plotted against different concentrations of calcein. The graph shows a plateau in lower concentrations of calcein. However, at higher concentrations there is a gradual drop in fluorescence.

Therefore, we optimized different parameters in the settings of the Envision multi plate fluorescence reader in order to increase the sensitivity and decrease the illumination. The amount of flashes per measurement was reduced from 10 to 4, the detector gain was diminished from 150 to 100 and only 60% excitation light was used instead of 100 %. With these new optimized parameters, the fluorescence of the aforementioned dilutions of calcein were again measured with the fluorescence microplate reader. As depicted by *Figure 44*, the classic shape of self-quenching calcein fluorescence was now obtained. High concentrations of calcein showed low fluorescence hence self-quenching, while by diluting the fluorophore, the fluorescence intensity was gradually augmenting, with the highest value of fluorescence at the concentration of 1 mM calcein.

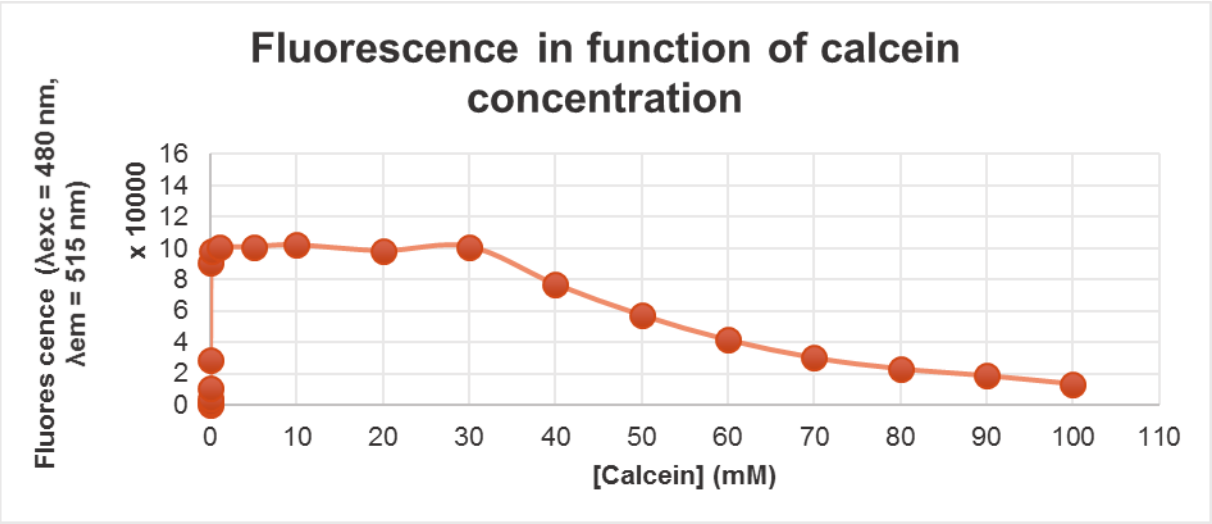

Figure 43: Calibration curve of the fluorescence of calcein in function of its concentration : 0,001 mM to 100 mM before optimization.

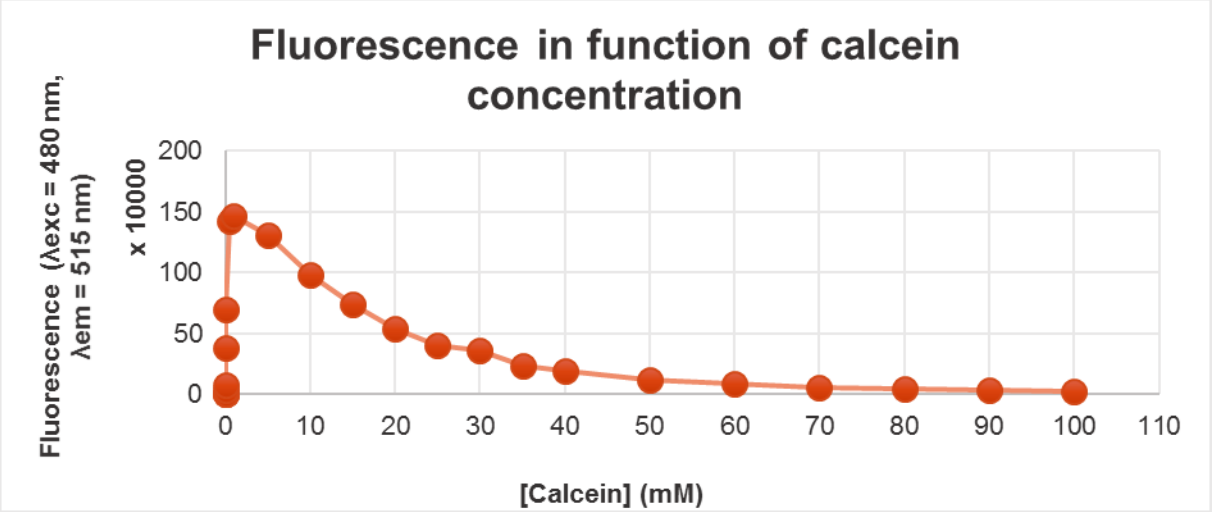

Figure 44: Calibration curve of the fluorescence of calcein in function of its concentration : 0,001 mM to 100 mM after optimizing the protocol

5.2.4.2 *Calcein encapsulation efficiency*

Calcein loaded liposomes, depicted in *Figure 35* were treated with 10 % Triton X-100 in order to completely break down the liposomes, hence obtain a complete release of the encapsulated calcein molecules. After 15 min incubation, calcein fluorescence was measured, which is displayed in *Figure 45*. To calculate the calcein encapsulation efficiency, *Equation 4* was used. As expected from the physicochemical characterization of calcein-encapsulating DOTAP/DOPE liposomes, only little calcein (25 %) was encapsulated inside those types of liposomes. The encapsulation efficiency of calcein inside DOPC/DPPG liposomes was 79 %. Other research groups also achieved high calcein encapsulation efficiencies (>70 %) by using *Equation 4*.[159,160]

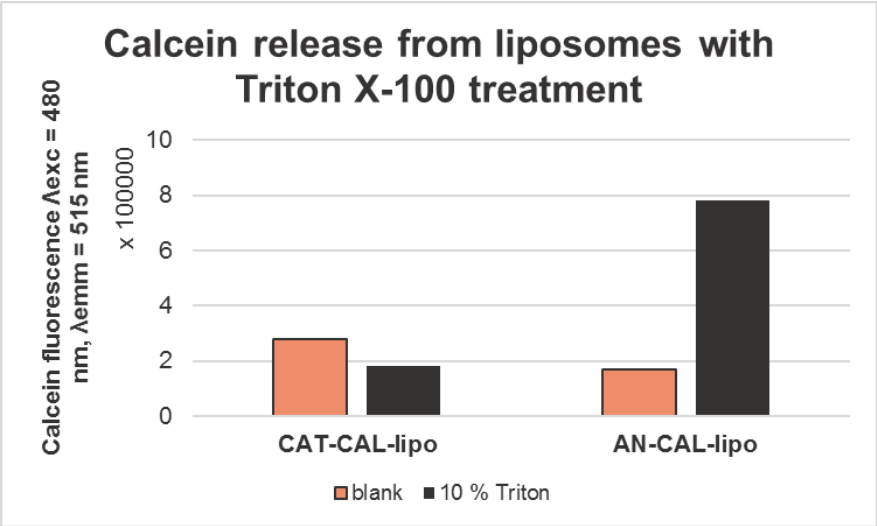

Figure 45: Fluorescence of CAT-CAL-lipo and AN-CAL-lipo after treatment with Triton X-100

5.2.4.3 *Spontaneous calcein leakage*

To investigate if and to what extent calcein leaks out of the liposomes, the fluorescence was monitored every 10 minutes for 12 hours.We expected calcein to show leakage in function of time, hence an increase in fluorescence intensity until the fluorescence reaches the positive control value. CAT-CAL-lipo showed generally a higher fluorescence intensity of calcein than AN-CAL-lipo. This can be attributed to the insufficient encapsulation of calcein inside positively charged liposomes. However, the experiment showed that fluorescence intensity decreased rapidly for positively as well as negatively charged liposomes as depicted in *Figure 46.*

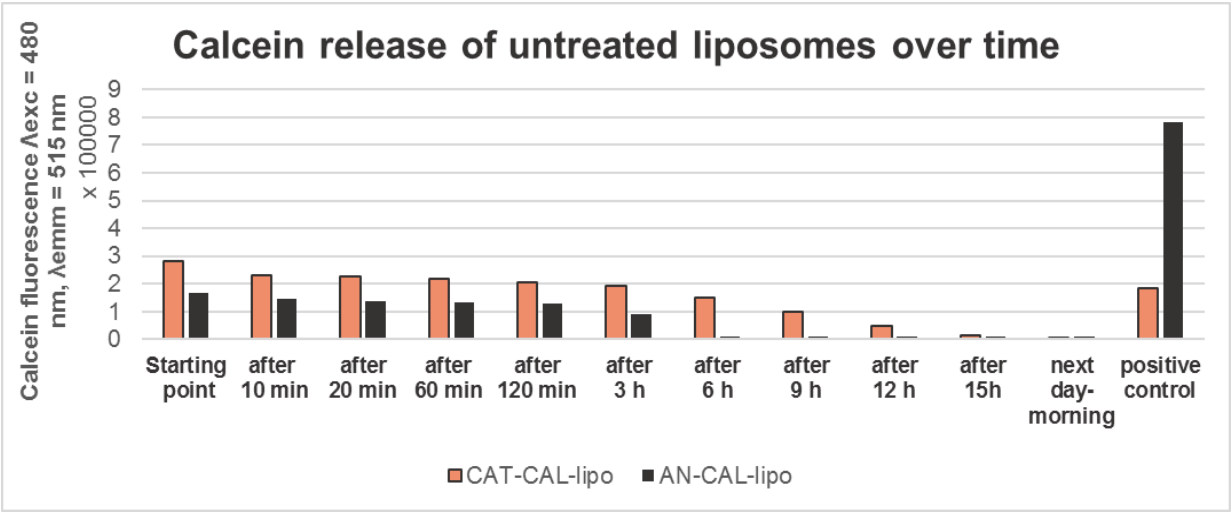

Figure 46: Spontaneous calcein leakage over time of positively and negatively charged liposomes; positive control: Triton X-100 treated liposomes

In order to check this, we also measured the fluorescence of Triton X-100 control over time on the same timepoints as the first experiment as depicted in *Figure 47*. We expected the positive control to remain the same over time. In reality the fluorescence intensities decreased over time. A possible explanation is that calcein was photo-

bleached by the frequent laser light irradiation during the experiment. As explained earlier, calcein is a light-sensitive fluorophore that is prone to show photobleaching, hence a decrease in fluorescence intensity.[161] In further experiments, photo-bleaching should be avoided by less frequent laser illuminations (e.g. every hour instead of every 10 minutes) or by including an internal standard such as calcein solution. Furthermore, negatively charged liposomes should be used for further release studies as the physicochemical parameters as well as the calcein release outperform positively charged liposomes.

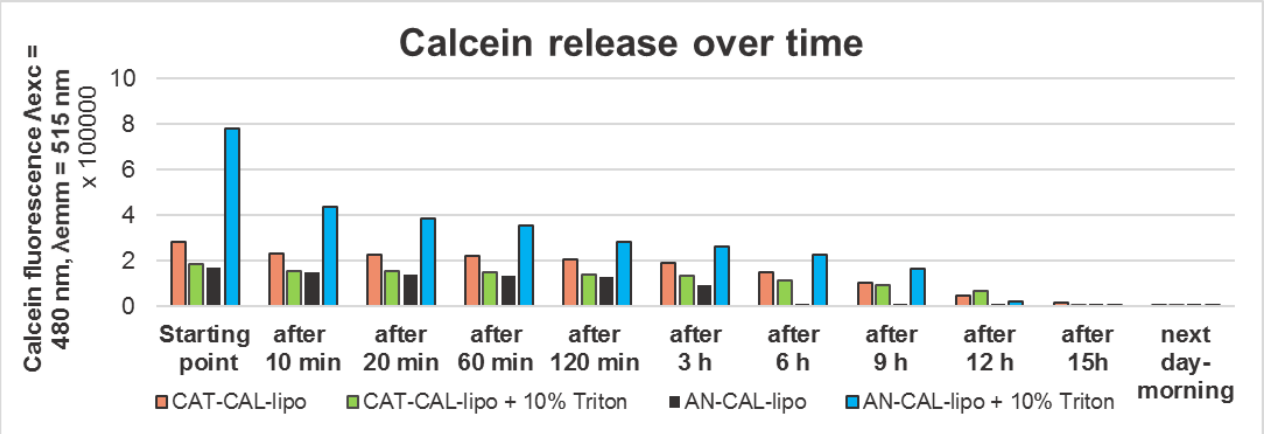

Figure 47: Spontaneous calcein leakage over time of positively and negatively charged liposomes; positive control for each time point: Triton X-100 treated liposomes

5.2.5 Calcein release via pulsed laser trigger

To determine whether one single laser pulse is able to disrupt liposomes hence to release calcein, liposomes with encapsulated Au-NPs were investigated. Liposomes were prepared as stated in *Table 4.* We investigated the potential of a single laser pulse to generate VNBs around the Au-NPs, hence disrupt the liposomal membrane and release the entrapped calcein molecules. As positive control, calcein release was triggered with 10% Triton X-100. Afterwards, the fluorescence intensity was measured with the fluorescence plate reader.

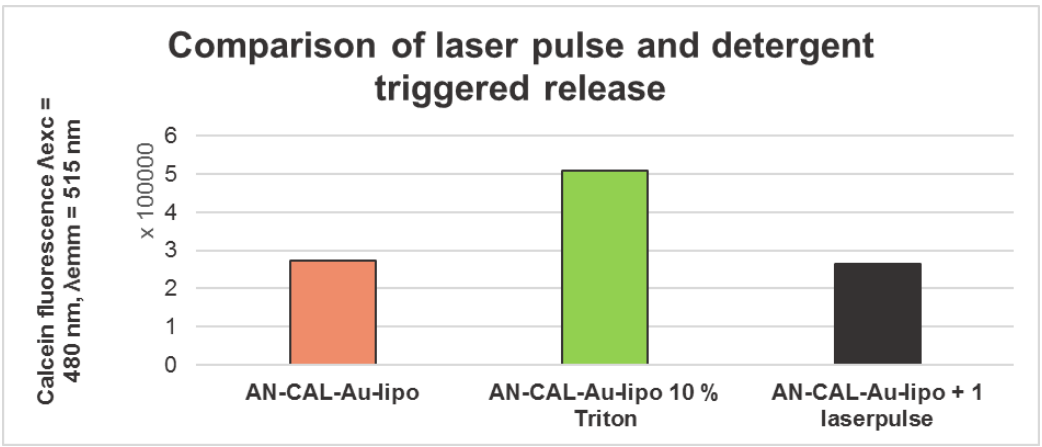

Figure 48: VNB mediated calcein release out of negatively charged liposomes

Triggered release via laser pulse hence VNB formation was tested for calcein loaded liposomes with Au-NPs encapsulated. The impact of background fluorescence, photobleaching as well as pulsed laser treatment hence the effect of the laser on the membrane integrity were taken into account.

We expected that the fluorescence intensity of the laser-treated sample would be as high as the positive control. However, there was no increase in fluorescence compared to the untreated AN-CAL-Au-lipo sample.

A possible explanation might be that either calcein was not properly encapsulated and therefore leaked out without any trigger or that the amount of encapsulated calcein was too low to provide a sufficient platform with broad dynamic range. What is more, the number of encapsulated gold was too low or VNBs emerging from encapsulated gold were not big enough to guarantee a sufficient leakage of calcein compared to VNBs of golden nanoparticles attached to liposomes' surfaces. Further experiments should consider a good encapsulation efficiency of calcein as well as a comparison of encapsulated and surface attached gold.

In the second experiment, calcein release from liposomes with Au-NPs attached to their surface was investigated, as stated in *4.2.6.1. Functionalization of liposomes with Au-NPs.* Several working solutions, enlisted in *Table 7***,** were prepared. After the laser treatment, the fluorescence of calcein was measured with a fluorescent microplate reader. The encapsulation efficiency was about 69% and was calculated with the *Equation 4*. Similar results were found in other research papers.[159,160]

First we measured the fluorescence intensity of NEU-CAL-lipo WS 1 functionalized with 10 nm Au-NPs. We expected an increase in fluorescence intensity for the laser treated sample similar to the positive control. However, there was no increase in fluorescence compared to before laser treatment. Next, NEU-CAL-lipo WS 1 functionalized with 40 nm Au-NPs was tested. An increase in fluorescence intensity for the laser treated working solution 1 was expected. In reality a decrease in fluorescence intensity compared to before laser treatment was observed. We were not able to provide proof of concept.

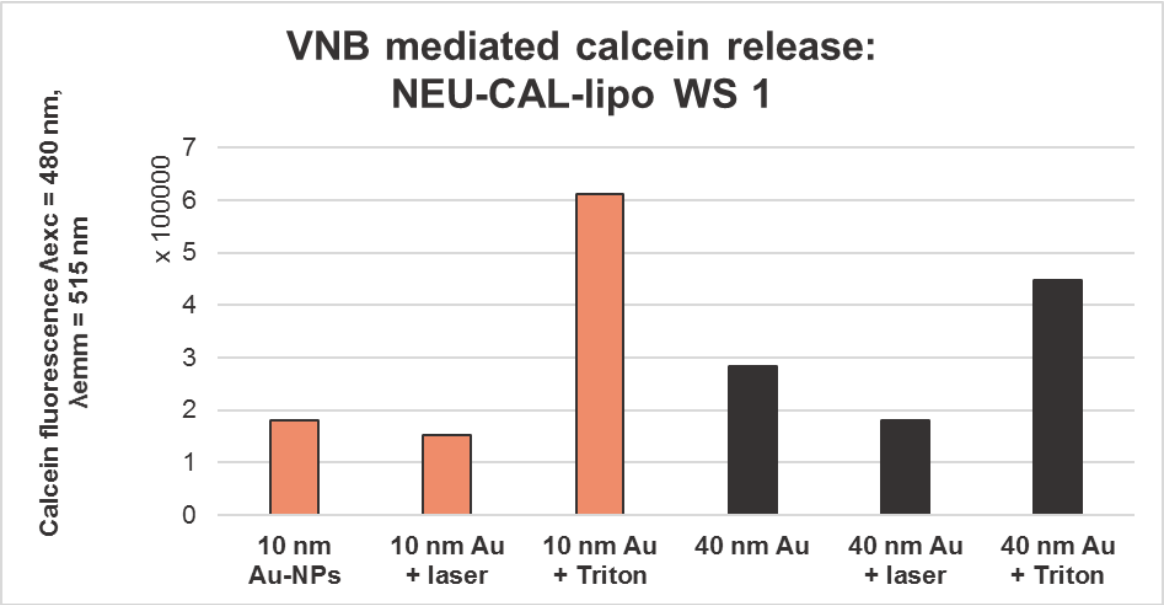

Figure 49: VNB triggered release of NEU-CAL-lipo WS 1 (liposomes with Au-NPs attached to their surface)

Next we tested the second working solution of NEU-CAL-lipo, which was either functionalized with 10 nm Au-NPs or 40 nm Au-NPs.

The laser treated 10 nm Au-NPs liposomal sample showed an enormous increase in fluorescence. However, the fluorescence was higher than the positive control. This suggests that the increase in fluorescence intensity is due to the pulsed laser effect. Further experiments should include the following positive control: Au-functionalized liposomes + laser treatment + Triton X-100.

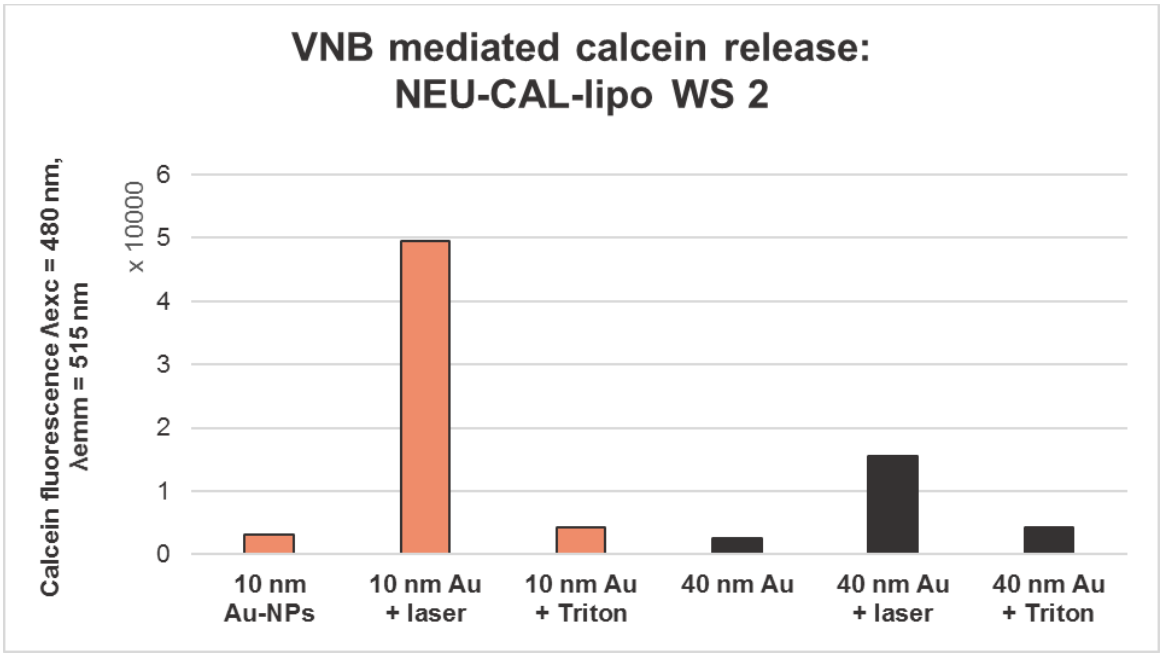

Figure 50: VNB triggered release of NEU-CAL-lipo WS 2 (diluted suspension of liposomes with Au-NPs attached to their surface)

The laser treatment for NEU-CAL-lipo WS 2 functionalized with 40 nm Au-NPs showed similar results as the sample functionalized with 10 nm Au-NPs. There was an increase in fluorescence of the laser treated sample compared to the non-laser treated. However, the fluorescence of the positive control was lower than the laser treated sample, which suggests that the laser itself impacts the membrane integrity. We were not able to provide proof of concept.

We can conclude that the pulsed laser effect on liposomes without golden NPs as well as the low encapsulation efficiency of calcein have a great impact on the results of these release studies. In further investigations, the aforementioned positive control should be included to rule out the pulsed laser effect. Furthermore, the encapsulation efficiency of calcein can be increased by using freeze-thaw prepared liposomes. It has been reported in many articles[162–164] that freeze-thawed liposomes show a higher encapsulation efficiency than liposomes prepared via TFH method.

What is more, a single laser pulse might not be sufficient to release fluorescent molecules from the liposomes. In further investigations, it should be tested if the amount of released calcein increases with the number of pulses. However, the light sensitivity of calcein should then be considered.

To provide the proof of concept, it might also be useful to change to a different fluorophore that is not prone to photo-bleach. The actual amount of VNB mediated fluorophore release might be high, but due to photo-bleaching only a small fraction is actually measured. Further experiments should rule out the effect of photo-bleaching by replacing calcein with a less light sensitive fluorophore.

5.3 Use of VNBs as trigger for antibiotic release

5.3.1 Characterisation of liposomes

First of all, tobramycin has been encapsulated in neutrally and negatively charged liposomes. *Table 3* enlists the exact volumes of lipids used to form liposomes. Next, for each batch, the hydrodynamic size and the zeta potential were measured via DLS.

	Ø z-average (nm)	**Ø Intensity (%)**	**Ø PDI**	**Zeta potential (mV)**
AN-TOBRA-lipo	101	97,7	0,251	-24,4
AN-HEP-lipo	105,9	95	0,326	-32,4
NEU-TOBRA-lipo	140,1	94,68	0,29	-8,07
NEU-HEP-lipo	140,3	97,3	0,22	-3,66

Table 14: DLS results of neutrally and negatively charged liposomes encapsulated with tobramycin or HEPES-buffer.

After purification, AN-TOBRA-lipo and AN-HEP-lipo showed an intensity based diameter of 101 nm and 105,9 nm. The low PDI of 0,251 as well as 0,326 show the presence of a monodisperse system. NEU-TOBRA-lipo and NEU-HEP-lipo are slightly increased in size with intensity based diameters of 140,1 nm and 140,3 nm. As there is a size limit for penetration inside biofilms, more specifically in *P.aeruginosa* biofilms, the intensity based diameter is of increased importance. The polydispersity index of neutrally charged liposomes is still low with 0,29 for NEU-TOBRA-lipo and 0,22 for NEU-HEP-lipo. *Table 14* depicts the difference of the surface charge as AN.-TOBRA-lipo and AN-HEP-lipo are highly negatively charged with a zeta potential of -24,4 mV and -32,4 mV whereas NEU-TOBRA-lipo and NEU-HEP-lipo have a zeta potential of -8,07 mV and -3,66 mV. *Figure 51* (A) and (B) present the DLS results of negatively and neutrally charged liposomes respectively. *Figure 51* (C) depicts the comparison of the zeta potential measured via DLS.

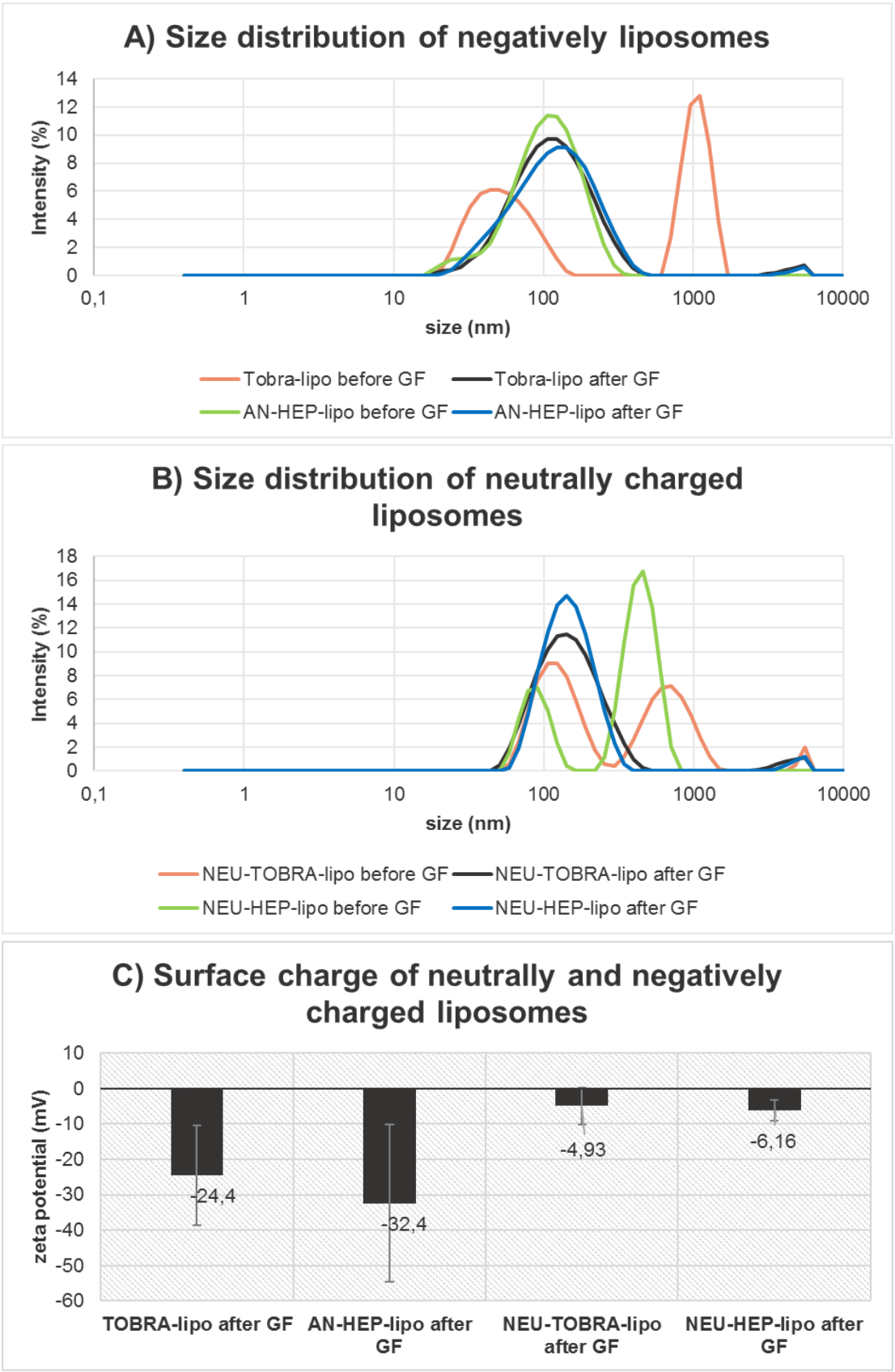

Figure 51: DLS results of neutrally and negatively charged liposomes: A) size distribution of negatively charged liposomes (tobramycin or HEPES loaded, before and after Gelfiltration (GF)), **B)** size distribution of neutrally charged liposomes (tobramycin or HEPES loaded, before and after Gelfiltration (GF)), **C)** comparison of the surface charge of neutrally and negatively charged liposomes after Gelfiltration

5.3.2 . Determination of tobramycin encapsulation efficiency

5.3.2.1 *Tobramycin calibration curve*

As previously described, the encapsulation efficiency was tested in an agar diffusion test. Therefore, liposomes were prepared as stated in *4.2.1 Preparation of liposomes*. After 24 hours of incubation with the tobramycin samples the inhibition zones were measured with a ruler.

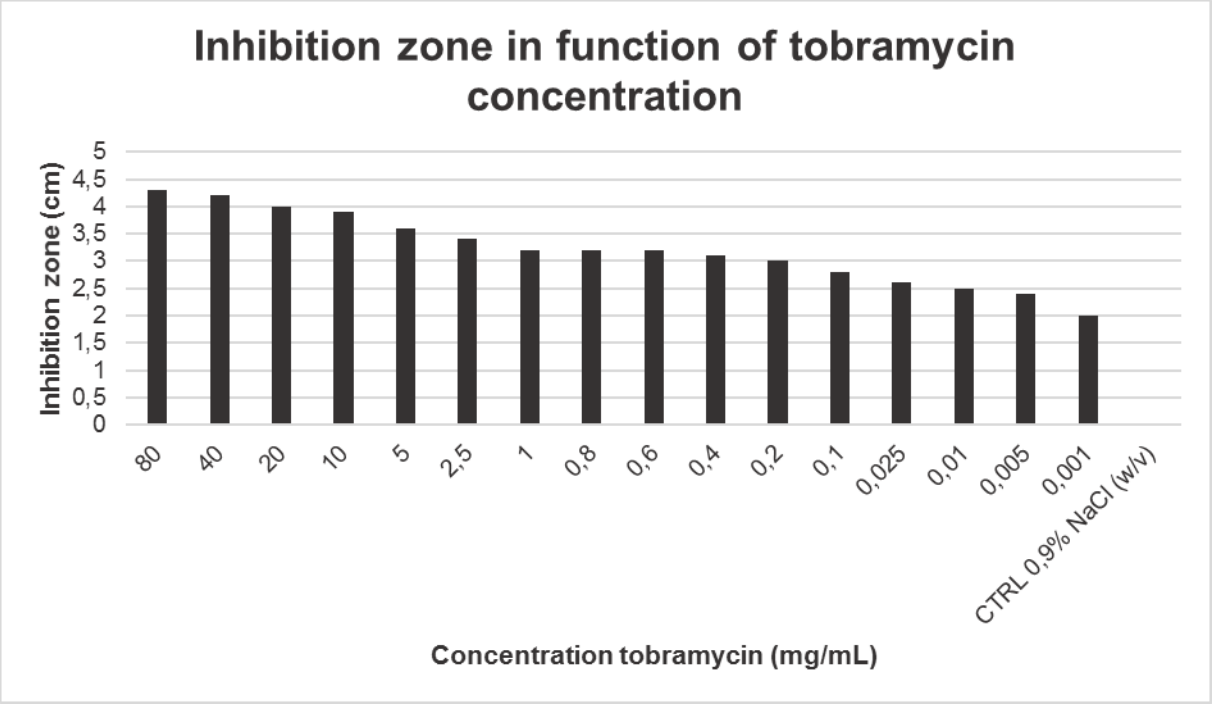

Figure 52 Inhibition zones of tobramycin treated *B. subtilis* cultures after 24 hours

As depicted by *Figure 52*, higher concentrations of tobramycin showed a larger inhibition zone than smaller concentrations. No inhibition was observed for 0,9 % NaCl control.

5.3.2.2 *Tobramycin encapsulation efficiency*

According to the calibration curve, the inhibition zones of the liposomal samples (AN-TOBRA-lipo and NEU-TOBRA-lipo) corresponded to a tobramycin concentration of 960 µg / mL (dilution factor taken into account). As the initial tobramycin concentration was 80 mg / mL, the encapsulation efficiency amounts to 1,2 %.

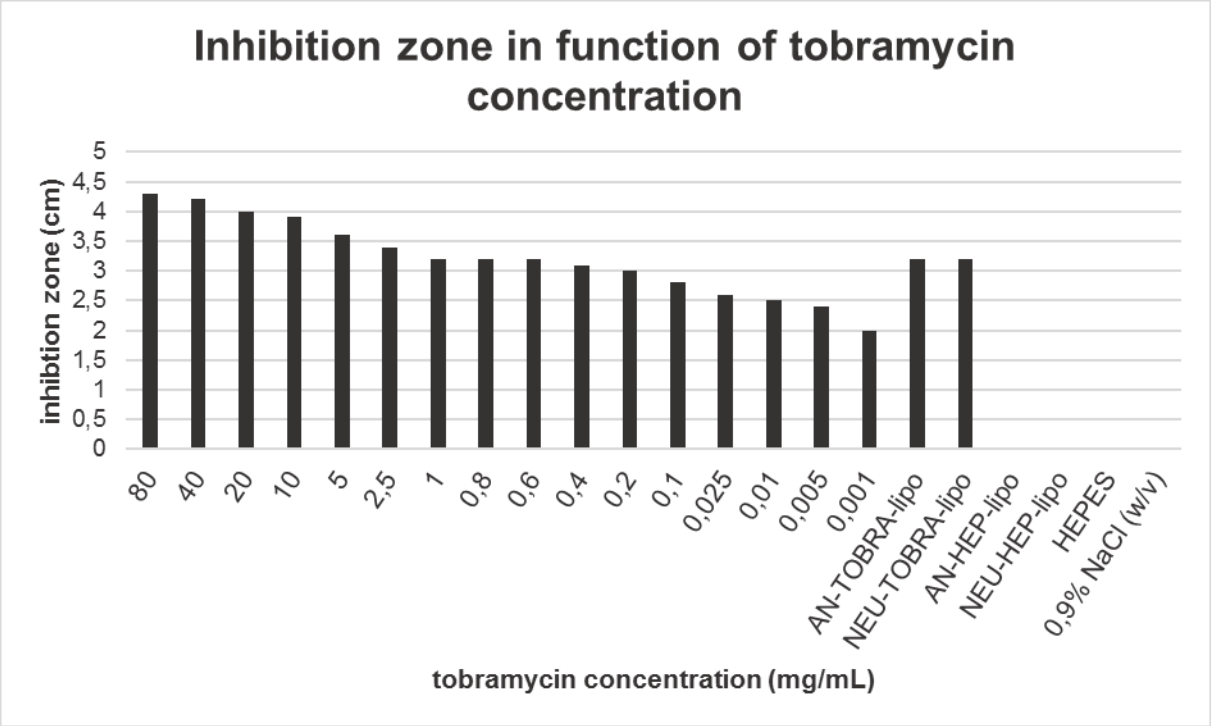

Figure 53: Inhibition zones of tobramycin treated *B. subtilis* cultures after 24 hours

5.3.3 Bioactivity of liposome-encapsulated tobramycin against *Pseudomonas aeruginosa* biofilms

To prove antimicrobial activity of liposome-encapsulated tobramycin a biofilm was grown as previously described**.** Next, the biofilm was treated with different samples stated in *4.2.11 Bioactivity of liposome-encapsulated tobramycin against Pseudomonas aeruginosa biofilms* incubated for 24 hours. Then, surviving bacteria were counted via plate counting**.** *Figure 54* shows the results of this experiment.

Control samples as 0,9 % NaCl (w/v) and HEPES buffer (with and without laser treatment) showed a high survival rate. All other samples showed a lower number of surviving bacteria. Especially all samples that contained golden NPs showed no survival of bacteria.

Although Au-NPs are known to be inert, bacteria were killed when incubated with 10 nm Au-NPs. One reason for the low survival rate might be the incubation with a high amount of Au-NPs for 24 hours. A 2:1 ratio of Au-NPs to liposomes was chosen to match the Au:liposome ratio of previous experiments, whereas 24 hours is the standard incubation time for antibiotic treatments of biofilms. In further investigations, the incubation time should be reduced to 15 minutes as the penetration of liposomes is sufficient in this time frame.

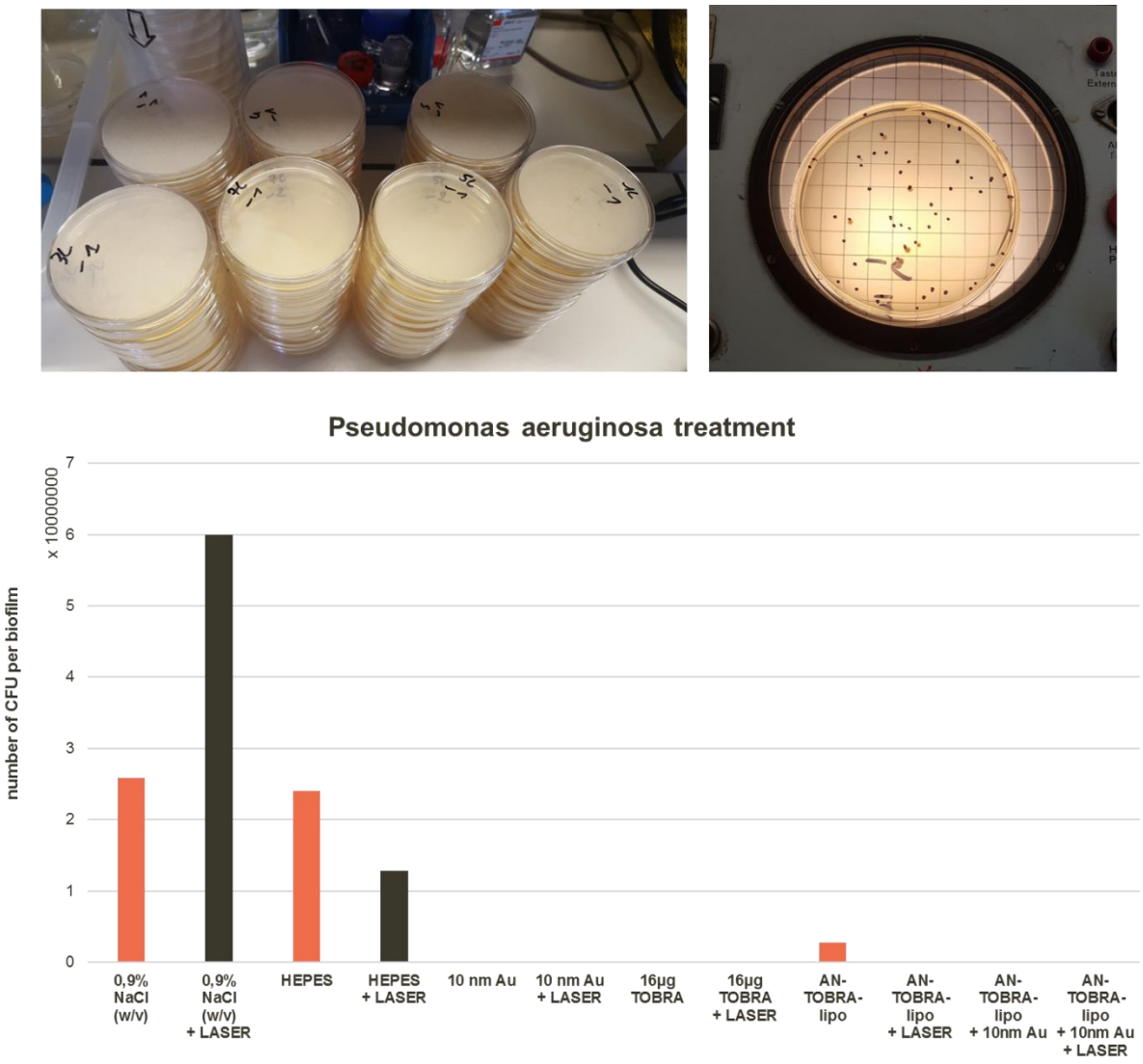

Figure 54: Top left: petri dishes with different dilutions of bacterial colonies. top right: **Petri dish displaying the individual colony forming units. bottom: Number of surviving CFU per biofilm after treatment with liposome-encapsulated tobramycin**

Another reason for the reduced survival rate might be the Au-NP suspension. In order to synthesize 10 nm Au-NPs, an auxiliary material (DMAP) was used to guarantee the particles' stability. It is possible that this auxiliary material has an impact on the surviving rate of bacteria. To exclude the auxiliary material's influence a control sample should be included in further experiments.

As the last experiment showed no surviving bacteria when treated with golden NPs, the protocol was optimized and the experiment was repeated. Instead of negatively charged liposomes, neutrally charged liposomes (NEU-TOBRA-lipo, NEU-HEP-lipo) were chosen due to practical issues, as the highly negatively charged lipid wasn't available at the time of experiment. Moreover, 40 nm Au-NPs were chosen to render liposomes light-triggerable as the use of 40 nm NPs required less auxiliary materials, that might influence the survival rate of bacteria. Results are shown in *Figure 55*.

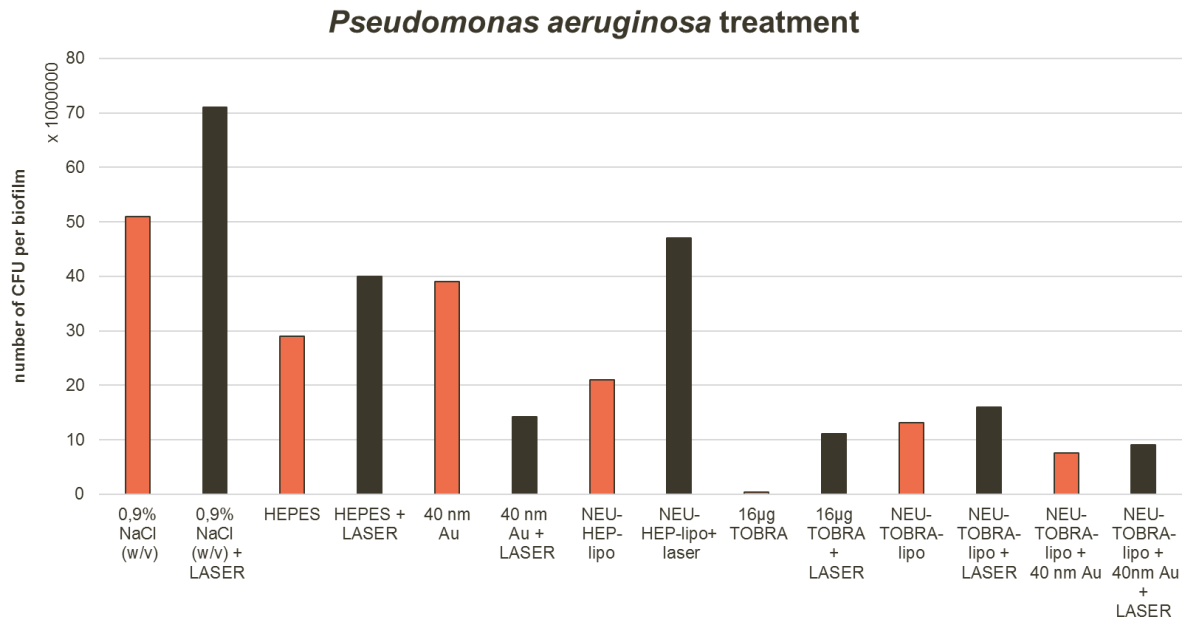

Figure 55: Plate counting result: after treatment of a biofilm with liposome-encapsulated tobramycin

There was an increase in the survival of bacteria treated with golden-NPs samples compared to the previous experiment. Decreasing the incubation time to 15 minutes was beneficial as there was a higher survival rate than previously. Comparing laser treated to non-laser treated, it seems that the pulsed laser effect as well as VNBs alone had an impact on the viability of bacteria.

The highest survival rates were observed when the biofilm was treated with 0,9 % (w/v) NaCl, HEPES-buffer and HEPES-loaded liposomes (negative controls). Bacteria treated with 16 µg TOBRA showed the lowest number of CFU per biofilm (positive control).

Tobramycin encapsulated in liposomes showed the second lowest number of CFU, only tobramycin control killed more bacteria. Combining NEU-TOBRA-lipo with golden NPs, there is even a lower number of surviving bacteria. This trend is also observed for the laser treated liposome-encapsulated tobramycin samples.

We can conclude that we were able to provide the proof of concept. Tobramycin - encapsulated liposomes showed the second lowest number of bacterial survival rate. However, the pulsed laser effect as well as the low encapsulation efficiency have a great impact on the release of the antibiotics. We expected that the laser treated conditions would show a lower bacterial survival rate than before laser treatment. However, bacteria with laser treated samples were more likely to survive. To be completely sure that the drug release is VNB mediated and not due to the laser pulsed effect, this experiment should be repeated in further investigations and darkfield microscopy should be included to visually confirm the generation of VNBs.

To overcome the low encapsulation efficiency of 1,2 %, freeze-thawed liposomes could be used instead of liposomes prepared via TFH method. As explained earlier, it is possible to encapsulate more drug inside liposomes by using another preparation technique. Upon pulsed laser trigger, more drug can then be released leaving a greater antimicrobial effect. In further investigations, a different liposomal preparation technique should be considered to enhance the amount of delivered antibiotics.

6 Conclusion

Increased antibiotic drug resistance and therapy failures hence chronic, long-lasting infections are an emerging problem in modern society. Due to different resistance mechanisms biofilm-related infections remain hard to eradicate. That is why modern medicine is left with an urgent need for novel ways of drug delivery to overcome severe bacterial infections.

The main aim of this diploma thesis was to investigate the use of vapour nanobubbles to highly-controllably trigger drug release out of liposomes and subsequently enhance bacteria's susceptibility towards antibiotics.

First of all, we evaluated the location of differently charged liposomes in two cystic fibrosis-derived biofilms, *P. aeruginosa* and *B. multivorans*. We can conclude that unpegylated liposomes, either positively or negatively charged, got stuck on the surface of the biofilm whereas pegylated liposomes penetrated deeper inside the liposomes. The best penetration results, hence the deepest penetration into the biofilm was achieved by C8 PEG2000 ceramide.

Next, we prepared different types of calcein-loaded liposomes in terms of liposomal surface charge. As negatively charged liposomes outperformed positively charged nanoparticles in terms of calcein encapsulation efficiency, further investigations were conducted with NEU-lipo and AN-lipo.

To functionalize the liposomes with either 10 nm or 40 nm Au-NPs, different Au:liposome ratios were investigated in terms of zeta potential inversion. Afterwards, we determined for each ratio, which laser pulse fluence should be applied to create VNBs around the liposomes. The highest surface coverage for both Au-NP sizes showed most VNB formations.

Calcein release out of liposomes after a trigger was measured via fluorimetry. Also the spontaneous calcein leakage out of liposomes was investigated. We observed a decreasing calcein fluorescence over time, which might be related to increased photobleaching because of the subsequent laser illuminations. To trigger calcein release, we first encapsulated golden NPs inside the lumen of liposomes. However, we did not observe an increased calcein fluorescence, hence no VNB-mediated calcein release could be shown.

Next, we decorated the liposomes' surfaces with Au-NPs and measured the calcein release. There was also no increased release of the fluorophore, which might be due to the low encapsulation efficiency achieved by TFH method.

Nonetheless, we investigated antibiotic loaded liposomes hence antibiotic release mediated by VNBs. Therefore, we encapsulated tobramycin in negatively charged liposomes with an efficiency of 1,2 %. Next, we functionalized them with golden NPs and treated a *Pseudomonas aeruginosa* biofilm with aforementioned liposomes. We can conclude that antibiotic release hence decreased bacterial cell viability could be measured after laser treatment.

7 Zusammenfassung

Steigende Antibiotikaresistenz einhergehend mit Therapiefehlschlägen und daraus resultierenden lang andauernden, chronischen Infektionen stellen die moderne Gesellschaft vor eine Herausforderung. Durch verschiedene spezifische Mechanismen sind biofilm-basierte Infektionen schwer zu beseitigen. Aus diesem Grund werden neue Wege gesucht, um Wirkstoffmoleküle direkt zum Wirkort zu transportieren.

Das Hauptziel meiner Diplomarbeit war es, Nanodampfblasen als Auslöser für gezielte Antibiotikafreisetzung aus Liposomen zu verwenden und somit die Empfindlichkeit von Bakterien gegenüber Antibiotika zu erhöhen.

Zuerst wurden verschieden geladene Liposomen hinsichtlich ihrer Penetration und ihrer Lage in zwei Biofilmen, *P. aeruginosa* und *B. multivorans* untersucht. Beide Stämme sind beteiligt am Krankheitsbild der Cystischen Fibrose. Unpegylierte Liposomen, entweder positiv oder negativ geladen, waren allesamt auf der Oberfläche zu finden. Pegylierte Liposomen hingegen penetrierten tiefer in den Biofilm und standen so in engerem Kontakt zu den Bakterienzellen. Die beste Penetration wurde durch die Pegylierung mit C8 PEG2000 Ceramid erreicht.

Als nächstes wurden unterschiedlich geladene Liposomen, die mit Calcein beladen waren, hergestellt. Da negativ geladene Liposomen sowohl bessere physikochemische Eigenschaften als auch eine bessere Calceinbeladungseffizienz zeigten, wurden NEU-lipo und AN-lipo weiterverwendet. Um das beste Au:Liposom-Verhältnis zu finden, wurden verschiedene Mengen an Goldnanopartikel, entweder 10 oder 40 nm groß, mit den Liposomen funktionalisiert und in Bezug auf die Inversion des Zetapotenzials untersucht. Danach wurde für jedes Au:Liposom-Verhältnis der Schwellenwert der Energie, die für die Formation von Dampfnanoblasen benötigt wird, festgestellt. Das höchste Au:Liposom-Verhältnis zeigte in beiden Fällen die meisten Dampfnanoblasen.

Die Calceinfreisetzung wurde mittels Fluorimetrie gemessen. Zuerst untersuchten wir die spontane Freisetzung von Calcein aus Liposomen. Wir stellten dabei mit der Zeit eine verminderte Fluoreszenz fest, welches auf das Ausbleichen des Fluorophores nach mehrmaliger Laserbestrahlung zurückzuführen ist. Als nächstes untersuchten wir Liposomen, die in ihrem Inneren sowohl Calcein als auch Goldnanopartikel hatten. Wir beobachteten aber keine gesteigerte Calceinfluoreszenz und somit keine dampfnanoblasenvermittelte Freisetzung. Daher funktionalisierten wir die Goldnanopartikel an die Oberfläche der Liposomen und untersuchten erneut die dampfnanoblasenvermittelte Freisetzung von Calcein. Auch in diesem Experiment wurde keine gesteigerte Calceinfreisetzung gemessen, was auf die geringe Menge an Calcein in den Liposomen zurückzuführen sein könnte.

Nichtsdestotrotz untersuchten wir mit Tobramycin beladene negative Liposomen in Bezug auf die dampfnanoblasenvermittelte Freisetzung des Antibiotikums. Zuvor wurde eine Antibiotikabeladungseffizienz von 1,2 % festgestellt. Als nächstes behandelten wir einen *Pseudomonas aeruginosa* Biofilm mit den negativ geladenen Tobramycin Liposomen, die zusätzlich noch Goldnanopartikel an ihrer Oberfläche trugen. Nach der Laserbehandlung konnten wir aufgrund der geringeren Überlebensrate der Bakterien feststellen, dass das Antibiotikum aus den Liposomen mittels Dampfnanoblasen freigesetzt wurde.

8 Attachment

8.1 Abstract

Antibiotic drug resistance is an emerging problem in modern society due to the presence of difficult to treat biofilms that cause long-lasting, chronic infections. To improve the efficacy of antibiotics, drug delivery methods can be used that enhance the drug delivery of antibiotics close to the biofilm-enclosed bacteria. In this diploma thesis, a novel light-triggered liposomal system was investigated in its capacity to release encapsulated molecules. By irradiating Au-NP-functionalized liposomes, so-called vapour nanobubbles (VNB) emerged, which were investigated for their potential to destroy liposomes hence trigger the release of the drug load. In this diploma thesis, DOPC:DPPG and DPPC:Cholesterol liposomes were prepared incorporating self-quenched calcein to measure release out of liposomes. However, we were not able to provide the proof of concept as the fluorescence intensity after laser irradiation did not increase in comparison to the positive control.

Antibiotic release (tobramycin) out of DOPC:DPPG and DPPC:Cholesterol liposomes however, did increase in comparison to ‘empty’ liposomes.

8.2 Zusammenfassung

Steigende Antibiotikaresistenz ist ein Problem moderner Medizin, da sogenannte Biofilme häufig lang andauernde, chronische Infektionen hervorrufen. Um die Effizienz der verwendeten Antibiotika zu steigern, können spezielle Methoden verwendet werden, um Wirkstoffmoleküle direkt zu den Bakterien im Biofilm zu befördern. In dieser Diplomarbeit, wurde ein neues, licht-gesteuertes liposomales System untersucht, das die Fähigkeit hat, Wirkstoffmoleküle aus Liposomen zu befreien. Werden Liposomen, die mit Goldnanopartikel funktionalisiert wurden, mit Licht bestrahlt, entstehen sogenannte Nano-Dampfblasen. Das Potenzial solcher Nano-Dampfblasen Liposomen zu zerstören und somit gezielt Wirkstoffmoleküle aus Liposomen freizusetzen, wurde untersucht. Es wurden DOPC:DPPG und DPPC:Cholesterol Liposomen mit Calcein, dessen Konzentration über der Fluoreszenzlöschung lag, beladen. Leider waren wir nicht im Stande die vorliegende Methode zu bestätigen, da die Fluoreszenzintensität nach Laserbestrahlung nicht größer wurde im Vergleich zur Positiv-Probe.

Die Freisetzung von Antibiotika (Tobramycin) aus DOPC:DPPG und DPPC:Cholesterol hingegen war im Vergleich zu „leeren“ Kontrollliposomen erhöht.

8.3 Table of references

I used my best endeavours to seek all claim holders of the pictures and obtain their permission to use their pictures in my thesis. Still, if any copyright infringement should emerge, please inform me.

1. Brayden, D. J. Controlled release technologies for drug delivery. *Drug Discov. Today* **8,** 976–978 (2003).
2. Preiss, M. R. & Bothun, G. D. Stimuli-responsive liposome-nanoparticle assemblies. *Expert Opin. Drug Deliv.* **8,** 1025–1040 (2011).
3. Forier, K. *et al.* Lipid and polymer nanoparticles for drug delivery to bacterial biofilms. *J. Controlled Release* **190,** 607–623 (2014).
4. Strebhardt, K. & Ullrich, A. Paul Ehrlich's magic bullet concept: 100 years of progress. *Nat. Rev. Cancer* **8,** 473–480 (2008).
5. Puri, A. Phototriggerable Liposomes: Current Research and Future Perspectives. *Pharmaceutics* **6,** 1–25 (2013).
6. Liu, D., Yang, F., Xiong, F. & Gu, N. The Smart Drug Delivery System and Its Clinical Potential. *Theranostics* **6,** 1306–1323 (2016).
7. Ong, S. G. M., Ming, L. C., Lee, K. S. & Yuen, K. H. Influence of the Encapsulation Efficiency and Size of Liposome on the Oral Bioavailability of Griseofulvin-Loaded Liposomes. *Pharmaceutics* **8,** (2016).
8. Barenholz, Y. (Chezy). Doxil® — The first FDA-approved nano-drug: Lessons learned. *J. Controlled Release* **160,** 117–134 (2012).
9. Ma, P. & Mumper, R. J. Paclitaxel Nano-Delivery Systems: A Comprehensive Review. *J. Nanomedicine Nanotechnol.* **4,** 1000164 (2013).

10. Wang, G. *et al.* Controlled preparation and antitumor efficacy of vitamin E TPGS-functionalized PLGA nanoparticles for delivery of paclitaxel. *Int. J. Pharm.* **446,** 24–33 (2013).

11. Tiwari, S. B. & Amiji, M. M. Improved oral delivery of paclitaxel following administration in nanoemulsion formulations. *J. Nanosci. Nanotechnol.* **6,** 3215–3221 (2006).

12. Reddy, J. A. & Low, P. S. Folate-mediated targeting of therapeutic and imaging agents to cancers. *Crit. Rev. Ther. Drug Carrier Syst.* **15,** 587–627 (1998).

13. Jaracz, S., Chen, J., Kuznetsova, L. V. & Ojima, I. Recent advances in tumor-targeting anticancer drug conjugates. *Bioorg. Med. Chem.* **13,** 5043–5054 (2005).

14. Rzigalinski, B. A. & Strobl, J. S. Cadmium-containing nanoparticles: perspectives on pharmacology and toxicology of quantum dots. *Toxicol. Appl. Pharmacol.* **238,** 280–288 (2009).

15. Tomalia, D. A., Reyna, L. A. & Svenson, S. Dendrimers as multi-purpose nanodevices for oncology drug delivery and diagnostic imaging. *Biochem. Soc. Trans.* **35,** 61–67 (2007).

16. Liao, J. Y. Construction of nanogold hollow balls with dendritic surface as immobilized affinity support for protein adsorption. *Colloids Surf. B Biointerfaces* **57,** 75–80 (2007).

17. Grund, S., Bauer, M. & Fischer, D. Polymers in Drug Delivery—State of the Art and Future Trends. *Adv. Eng. Mater.* **13,** B61–B87 (2011).

18. Rao, J. P. & Geckeler, K. E. Polymer nanoparticles: Preparation techniques and size-control parameters. *Prog. Polym. Sci.* **36,** 887–913 (2011).

19. Forier, K. *et al.* Probing the size limit for nanomedicine penetration into Burkholderia multivorans and Pseudomonas aeruginosa biofilms. *J. Controlled Release* **195,** 21–28 (2014).

20. Siafaka, P. I., Üstündağ Okur, N., Karavas, E. & Bikiaris, D. N. Surface Modified Multifunctional and Stimuli Responsive Nanoparticles for Drug Targeting: Current Status and Uses. *Int. J. Mol. Sci.* **17,** 1440 (2016).

21. Hinde, E. *et al.* Pair correlation microscopy reveals the role of nanoparticle shape in intracellular transport and site of drug release. *Nat. Nanotechnol.* **12,** 81–89 (2017).

22. Acharya, S. & Sahoo, S. K. PLGA nanoparticles containing various anticancer agents and tumour delivery by EPR effect. *Adv. Drug Deliv. Rev.* **63,** 170–183 (2011).

23. Wang, A. Z. EPR or no EPR? The billion-dollar question. *Sci. Transl. Med.* **7,** 294ec112-294ec112 (2015).

24. Danhier, F. To exploit the tumor microenvironment: Since the EPR effect fails in the clinic, what is the future of nanomedicine? *J. Controlled Release* **244, Part A,** 108–121 (2016).

25. Ekdawi, S. N., Jaffray, D. A. & Allen, C. Nanomedicine and tumor heterogeneity: Concept and complex reality. *Nano Today* **11,** 402–414 (2016).

26. Barenholz, Y. *et al.* Stability of liposomal doxorubicin formulations: problems and prospects. *Med. Res. Rev.* **13,** 449–491 (1993).

27. Zanganeh, S., Spitler, R., Erfanzadeh, M., Alkilany, A. M. & Mahmoudi, M. Protein corona: Opportunities and challenges. *Int. J. Biochem. Cell Biol.* **75,** 143–147 (2016).

28. Bangham, A. D. & Horne, R. W. Negative staining of phospholipids and their structural modification by surface-active agents as observed in the electron microscope. *J. Mol. Biol.* **8,** 660–IN10 (1964).

29. Gregoriadis, G. Drug entrapment in liposomes. *FEBS Lett.* **36,** 292–296 (1973).

30. Torchilin, V. P. Recent advances with liposomes as pharmaceutical carriers. *Nat. Rev. Drug Discov.* **4,** 145–160 (2005).

31. Riaz, M. Liposomes preparation methods. *Pak. J. Pharm. Sci.* **9,** 65–77 (1996).

32. Bozzuto, G. & Molinari, A. Liposomes as nanomedical devices. *Int. J. Nanomedicine* **10,** 975–999 (2015).

33. Akbarzadeh, A. *et al.* Liposome: classification, preparation, and applications. *Nanoscale Res. Lett.* **8,** 102 (2013).

34. Briuglia, M.-L., Rotella, C., McFarlane, A. & Lamprou, D. A. Influence of cholesterol on liposome stability and on in vitro drug release. *Drug Deliv. Transl. Res.* **5,** 231–242 (2015).

35. Petros, R. A. & DeSimone, J. M. Strategies in the design of nanoparticles for therapeutic applications. *Nat. Rev. Drug Discov.* **9,** 615–627 (2010).

36. Ferrari, M. Frontiers in Cancer Nanomedicine: Directing Mass Transport through Biological Barriers. *Trends Biotechnol.* **28,** 181–188 (2010).

37. Kronberg, B., Dahlman, A., Carlfors, J., Karlsson, J. & Artursson, P. Preparation and evaluation of sterically stabilized liposomes: colloidal stability, serum stability, macrophage uptake, and toxicity. *J. Pharm. Sci.* **79,** 667–671 (1990).

38. Puri, A. *et al.* Lipid-based nanoparticles as pharmaceutical drug carriers: from concepts to clinic. *Crit. Rev. Ther. Drug Carrier Syst.* **26,** 523–580 (2009).

39. Samad, A., Sultana, Y. & Aqil, M. Liposomal drug delivery systems: an update review. *Curr. Drug Deliv.* **4,** 297–305 (2007).

40. Balaz, S. Does transbilayer diffusion have a role in membrane transport of drugs? *Drug Discov. Today* **17,** 1079–1087 (2012).

41. What Is The Transition Temperature Of The Lipid? | Avanti Polar Lipids.

42. Kojima, C., Hirano, Y., Yuba, E., Harada, A. & Kono, K. Preparation and characterization of complexes of liposomes with gold nanoparticles. *Colloids Surf. B Biointerfaces* **66,** 246–252 (2008).

43. Hoare, T. *et al.* A Magnetically-Triggered Composite Membrane for On-Demand Drug Delivery. *Nano Lett.* **9,** 3651–3657 (2009).

44. Hoare, T. *et al.* Magnetically-triggered Nanocomposite Membranes: a Versatile Platform for Triggered Drug Release. *Nano Lett.* **11,** 1395–1400 (2011).

45. Yudina, A. *et al.* Ultrasound-mediated intracellular drug delivery using microbubbles and temperature-sensitive liposomes. *J. Control. Release Off. J. Control. Release Soc.* **155,** 442–448 (2011).

46. Timko, B. P., Dvir, T. & Kohane, D. S. Remotely Triggerable Drug Delivery Systems. *Adv. Mater.* **22,** 4925–4943 (2010).

47. Yavlovich, A., Smith, B., Gupta, K., Blumenthal, R. & Puri, A. Light-sensitive lipid-based nanoparticles for drug delivery: design principles and future considerations for biological applications. *Mol. Membr. Biol.* **27,** 364–381 (2010).

48. Idris, N. M. *et al.* In vivo photodynamic therapy using upconversion nanoparticles as remote-controlled nanotransducers. *Nat. Med.* **18,** 1580–1585 (2012).

49. Liu, Q., Zhan, C. & Kohane, D. S. Phototriggered Drug Delivery Using Inorganic Nanomaterials. *Bioconjug. Chem.* (2016). doi:10.1021/acs.bioconjchem.6b00448

50. Rwei, A. Y., Wang, W. & Kohane, D. S. Photoresponsive nanoparticles for drug delivery. *Nano Today* **10,** 451–467 (2015).

51. Curcio, J. A. & Petty, C. C. The Near Infrared Absorption Spectrum of Liquid Water. *JOSA* **41,** 302–304 (1951).

52. Weissleder, R. & Ntziachristos, V. Shedding light onto live molecular targets. *Nat. Med.* **9,** 123–128 (2003).

53. Pissuwan, D., Valenzuela, S. M. & Cortie, M. B. Therapeutic possibilities of plasmonically heated gold nanoparticles. *Trends Biotechnol.* **24,** 62–67 (2006).

54. Chen, H. *et al.* In Vivo Study of Spherical Gold Nanoparticles: Inflammatory Effects and Distribution in Mice. *PLOS ONE* **8,** e58208 (2013).

55. Huang, X. & El-Sayed, M. A. Gold nanoparticles: Optical properties and implementations in cancer diagnosis and photothermal therapy. *J. Adv. Res.* **1,** 13–28 (2010).

56. Jana, N. R., Gearheart, L. & Murphy, C. J. Wet Chemical Synthesis of High Aspect Ratio Cylindrical Gold Nanorods. *J. Phys. Chem. B* **105,** 4065–4067 (2001).

57. Jain, P. K., Huang, X., El-Sayed, I. H. & El-Sayed, M. A. Review of Some Interesting Surface Plasmon Resonance-enhanced Properties of Noble Metal Nanoparticles and Their Applications to Biosystems. *Plasmonics* **2,** 107–118 (2007).

58. Pérez-Juste, J., Pastoriza-Santos, I., Liz-Marzán, L. M. & Mulvaney, P. Gold nanorods: Synthesis, characterization and applications. *Coord. Chem. Rev.* **249,** 1870–1901 (2005).

59. Paasonen, L. *et al.* Gold-embedded photosensitive liposomes for drug delivery: Triggering mechanism and intracellular release. *ResearchGate* **147,** 136–43 (2010).

60. Chithrani, D. B., Dunne, M., Stewart, J., Allen, C. & Jaffray, D. A. Cellular uptake and transport of gold nanoparticles incorporated in a liposomal carrier. *Nanomedicine Nanotechnol. Biol. Med.* **6,** 161–169 (2010).

61. Paasonen, L. *et al.* Gold nanoparticles enable selective light-induced contents release from liposomes. *J. Controlled Release* **122,** 86–93 (2007).

62. Lapotko, D. Optical excitation and detection of vapor bubbles around plasmonic nanoparticles. *Opt. Express* **17,** 2538–2556 (2009).

63. Huang, X., El-Sayed, I. H. & El-Sayed, M. A. Applications of gold nanorods for cancer imaging and photothermal therapy. *Methods Mol. Biol. Clifton NJ* **624,** 343–357 (2010).

64. Lukianova-Hleb, E. Y., Volkov, A. N. & Lapotko, D. O. Laser pulse duration is critical for the generation of plasmonic nanobubbles. *Langmuir ACS J. Surf. Colloids* **30,** 7425–7434 (2014).

65. Lapotko, D. Plasmonic nanoparticle-generated photothermal bubbles and their biomedical applications. *Nanomed.* **4,** 813–845 (2009).

66. Anderson, L., Hansen, E., Lukianova-Hleb, E. Y., Hafner, J. H. & Lapotko, D. O. Optically Guided Controlled Release from Liposomes With Tunable Plasmonic Nanobubbles. *J. Control. Release Off. J. Control. Release Soc.* **144,** 151–158 (2010).

67. Xiong, R. *et al.* Comparison of Gold Nanoparticle Mediated Photoporation: Vapor Nanobubbles Outperform Direct Heating for Delivering Macromolecules in Live Cells. *ACS Nano* **8,** 6288–6296 (2014).

68. Lukianova-Hleb, E. Y. *et al.* Plasmonic Nanobubbles Rapidly Detect and Destroy Drug-Resistant Tumors. *Theranostics* **2,** 976–987 (2012).

69. Lukianova-Hleb, E. Y., Wagner, D. S., Brenner, M. K. & Lapotko, D. O. Cell-specific transmembrane injection of molecular cargo with gold nanoparticle-generated transient plasmonic nanobubbles. *Biomaterials* **33,** 5441–5450 (2012).

70. Lukianova-Hleb, E. Y., Belyanin, A., Kashinath, S., Wu, X. & Lapotko, D. O. Plasmonic nanobubble-enhanced endosomal escape processes for selective and guided intracellular delivery of chemotherapy to drug-resistant cancer cells. *Biomaterials* **33,** 1821–1826 (2012).

71. Lukianova-Hleb, E. Y. *et al.* Tunable plasmonic nanoprobes for theranostics of prostate cancer. *Theranostics* **1,** 3–17 (2011).

72. Lukianova-Hleb, E. Y., Hanna, E. Y., Hafner, J. H. & Lapotko, D. O. Tunable plasmonic nanobubbles for cell theranostics. *Nanotechnology* **21,** 85102 (2010).

73. Wagner, D. S. *et al.* The in vivo performance of plasmonic nanobubbles as cell theranostic agents in zebrafish hosting prostate cancer xenografts. *Biomaterials* **31,** 7567–7574 (2010).

74. Lebeaux, D., Ghigo, J.-M. & Beloin, C. Biofilm-related infections: bridging the gap between clinical management and fundamental aspects of recalcitrance toward antibiotics. *Microbiol. Mol. Biol. Rev. MMBR* **78,** 510–543 (2014).

75. Friedman, N. D., Temkin, E. & Carmeli, Y. The negative impact of antibiotic resistance. *Clin. Microbiol. Infect.* **22,** 416–422 (2016).

76. Courvalin, P. Why is antibiotic resistance a deadly emerging disease? *Clin. Microbiol. Infect.* **22,** 405–407 (2016).

77. Ventola, C. L. The Antibiotic Resistance Crisis. *Pharm. Ther.* **40,** 277–283 (2015).

78. Arias, C. A. & Murray, B. E. Antibiotic-Resistant Bugs in the 21st Century — A Clinical Super-Challenge. *N. Engl. J. Med.* **360,** 439–443 (2009).

79. Livermore, D. M. Bacterial Resistance: Origins, Epidemiology, and Impact. *Clin. Infect. Dis.* **36,** S11–S23 (2003).

80. Read, A. F. & Woods, R. J. Antibiotic resistance management. *Evol. Med. Public Health* **2014,** 147 (2014).

81. Müller, F.-M. C., Seidler, M. & Beauvais, A. Aspergillus fumigatus biofilms in the clinical setting. *Med. Mycol.* **49 Suppl 1,** S96–S100 (2011).

82. Islam, M. S., Richards, J. P. & Ojha, A. K. Targeting drug tolerance in mycobacteria: a perspective from mycobacterial biofilms. *Expert Rev. Anti Infect. Ther.* **10,** 1055–1066 (2012).

83. Stewart, P. S. & Costerton, J. W. Antibiotic resistance of bacteria in biofilms. *Lancet Lond. Engl.* **358,** 135–138 (2001).

84. Greenberg, E. P. Bacterial communication and group behavior. *J. Clin. Invest.* **112,** 1288–1290 (2003).

85. Song, T., Duperthuy, M. & Wai, S. N. Sub-Optimal Treatment of Bacterial Biofilms. *Antibiotics* **5,** 23 (2016).

86. Henrici, A. T. Studies of Freshwater Bacteria I. A Direct Microscopic Technique. *J. Bacteriol.* **25,** 277–287 (1933).

87. Mack, W. N., Mack, J. P. & Ackerson, A. O. Microbial film development in a trickling filter. *Microb. Ecol.* **2,** 215–226 (1975).

88. Høiby, N. A personal history of research on microbial biofilms and biofilm infections. *Pathog. Dis.* **70,** 205–211 (2014).

89. Rukavina, Z. & Vanić, Ž. Current Trends in Development of Liposomes for Targeting Bacterial Biofilms. *Pharmaceutics* **8,** 18 (2016).

90. Stewart, P. S. Mechanisms of antibiotic resistance in bacterial biofilms. *Int. J. Med. Microbiol.* **292,** 107–113 (2002).

91. Hall-Stoodley, L., Costerton, J. W. & Stoodley, P. Bacterial biofilms: from the natural environment to infectious diseases. *Nat. Rev. Microbiol.* **2,** 95–108 (2004).

92. Gristina, A. G. & Costerton, J. W. Bacterial adherence to biomaterials and tissue. The significance of its role in clinical sepsis. *J Bone Jt. Surg Am* **67,** 264–273 (1985).

93. Bell, B. G., Schellevis, F., Stobberingh, E., Goossens, H. & Pringle, M. A systematic review and meta-analysis of the effects of antibiotic consumption on antibiotic resistance. *BMC Infect. Dis.* **14,** 13 (2014).

94. jw643. Biofilms — University of Leicester. Available at: http://www2.le.ac.uk/departments/genetics/vgec/schoolscolleges/topics/microbial-genetics-1/infection/biofilms. (Accessed: 8th December 2016)

95. Elder, M. J., Stapleton, F., Evans, E. & Dart, J. K. G. Biofilm-related infections in ophthalmology. *Eye* **9,** 102–109 (1995).

96. Høiby, N., Bjarnsholt, T., Givskov, M., Molin, S. & Ciofu, O. Antibiotic resistance of bacterial biofilms. *Int. J. Antimicrob. Agents* **35,** 322–332 (2010).

97. del Pozo, J. L. & Patel, R. The Challenge of Treating Biofilm-associated Bacterial Infections. *Clin. Pharmacol. Ther.* **82,** 204–209 (2007).

98. de Oliveira, A. *et al.* Antimicrobial Resistance Profile of Planktonic and Biofilm Cells of Staphylococcus aureus and Coagulase-Negative Staphylococci. *Int. J. Mol. Sci.* **17,** (2016).

99. Fux, C. A., Costerton, J. W., Stewart, P. S. & Stoodley, P. Survival strategies of infectious biofilms. *Trends Microbiol.* **13,** 34–40 (2005).

100. . P. aeruginosa biofilm resistance. Schematic representation of... - Figure 2 of 2. Available at: https://www.researchgate.net/figure/9004189_fig2_Fig-2-P-aeruginosa-biofilm-resistance-Schematic-representation-of-mechanisms. (Accessed: 23rd January 2017)

101. Brock, T. D. Microbial growth rates in nature. *Bacteriol. Rev.* **35,** 39–58 (1971).

102. Van Acker, H., Van Dijck, P. & Coenye, T. Molecular mechanisms of antimicrobial tolerance and resistance in bacterial and fungal biofilms. *Trends Microbiol.* **22,** 326–333 (2014).

103. Alipour, M., Suntres, Z. E. & Omri, A. Importance of DNase and alginate lyase for enhancing free and liposome encapsulated aminoglycoside activity against Pseudomonas aeruginosa. *J. Antimicrob. Chemother.* **64,** 317–325 (2009).

104. Tuomanen, E., Cozens, R., Tosch, W., Zak, O. & Tomasz, A. The rate of killing of Escherichia coli by beta-lactam antibiotics is strictly proportional to the rate of bacterial growth. *J. Gen. Microbiol.* **132,** 1297–1304 (1986).

105. Billings, N. *et al.* The Extracellular Matrix Component Psl Provides Fast-Acting Antibiotic Defense in Pseudomonas aeruginosa Biofilms. *PLOS Pathog.* **9,** e1003526 (2013).

106. Hughes, D. & Andersson, D. I. Selection of resistance at lethal and non-lethal antibiotic concentrations. *Curr. Opin. Microbiol.* **15,** 555–560 (2012).

107. Dwyer, D. J., Kohanski, M. A. & Collins, J. J. Role of Reactive Oxygen Species in Antibiotic Action and Resistance. *Curr. Opin. Microbiol.* **12,** 482–489 (2009).

108. Stephens, C. Microbiology: Breaking Down Biofilms. *Curr. Biol.* **12,** R132–R134 (2002).

109. Roche, D. M. *et al.* Communications blackout? Do N-acylhomoserine-lactone-degrading enzymes have any role in quorum sensing? *Microbiol. Read. Engl.* **150,** 2023–2028 (2004).

110. Bjarnsholt, T., Ciofu, O., Molin, S., Givskov, M. & Høiby, N. Applying insights from biofilm biology to drug development — can a new approach be developed? *Nat. Rev. Drug Discov.* **12,** 791–808 (2013).

111. Cochran, W. L., McFeters, G. A. & Stewart, P. S. Reduced susceptibility of thin Pseudomonas aeruginosa biofilms to hydrogen peroxide and monochloramine. *J. Appl. Microbiol.* **88,** 22–30 (2000).

112. Lebeaux, D., Ghigo, J.-M. & Beloin, C. Biofilm-Related Infections: Bridging the Gap between Clinical Management and Fundamental Aspects of Recalcitrance toward Antibiotics. *Microbiol. Mol. Biol. Rev.* **78,** 510–543 (2014).

113. Chambless, J. D., Hunt, S. M. & Stewart, P. S. A Three-Dimensional Computer Model of Four Hypothetical Mechanisms Protecting Biofilms from Antimicrobials. *Appl. Environ. Microbiol.* **72,** 2005–2013 (2006).

114. Messiaen, A.-S., Forier, K., Nelis, H., Braeckmans, K. & Coenye, T. Transport of nanoparticles and tobramycin-loaded liposomes in Burkholderia cepacia complex biofilms. *PloS One* **8,** e79220 (2013).

115. Nacucchio, M. C., Bellora, M. J., Sordelli, D. O. & D'Aquino, M. Enhanced liposome-mediated activity of piperacillin against staphylococci. *Antimicrob. Agents Chemother.* **27,** 137–139 (1985).

116. Mugabe, C., Azghani, A. O. & Omri, A. Liposome-mediated gentamicin delivery: development and activity against resistant strains of Pseudomonas aeruginosa isolated from cystic fibrosis patients. *J. Antimicrob. Chemother.* **55,** 269–271 (2005).

117. Hadinoto, K. & Cheow, W. S. Nano-antibiotics in chronic lung infection therapy against Pseudomonas aeruginosa. *Colloids Surf. B Biointerfaces* **116,** 772–785 (2014).

118. Beaulac, C., Clément-Major, S., Hawari, J. & Lagacé, J. Eradication of mucoid Pseudomonas aeruginosa with fluid liposome-encapsulated tobramycin in an animal model of chronic pulmonary infection. *Antimicrob. Agents Chemother.* **40,** 665–669 (1996).

119. Sachetelli, S. *et al.* Demonstration of a fusion mechanism between a fluid bactericidal liposomal formulation and bacterial cells. *Biochim. Biophys. Acta* **1463,** 254–266 (2000).

120. Alhajlan, M., Alhariri, M. & Omri, A. Efficacy and safety of liposomal clarithromycin and its effect on Pseudomonas aeruginosa virulence factors. *Antimicrob. Agents Chemother.* **57,** 2694–2704 (2013).

121. Omri, A. *et al.* Pulmonary retention of free and liposome-encapsulated tobramycin after intratracheal administration in uninfected rats and rats infected with Pseudomonas aeruginosa. *Antimicrob. Agents Chemother.* **38,** 1090–1095 (1994).

122. Jones, M. N. *et al.* The targeting of phospholipid liposomes to bacteria. *Biochim. Biophys. Acta* **1196,** 57–64 (1994).

123. Hill, K. J., Kaszuba, M., Creeth, J. E. & Jones, M. N. Reactive liposomes encapsulating a glucose oxidase-peroxidase system with antibacterial activity. *Biochim. Biophys. Acta* **1326,** 37–46 (1997).

124. Jones, M. N., Hill, K. J., Kaszuba, M. & Creeth, J. E. Antibacterial reactive liposomes encapsulating coupled enzyme systems. *Int. J. Pharm.* **162,** 107–117 (1998).

125. Jones, M. N., Francis, S. E., Hutchinson, F. J., Handley, P. S. & Lyle, I. G. Targeting and delivery of bactericide to adsorbed oral bacteria by use of proteoliposomes. *Biochim. Biophys. Acta* **1147,** 251–261 (1993).

126. Zhao, J., Seeluangsawat, P. & Wang, Q. Modeling antimicrobial tolerance and treatment of heterogeneous biofilms. *Math. Biosci.* **282,** 1–15 (2016).

127. Meers, P. *et al.* Biofilm penetration, triggered release and in vivo activity of inhaled liposomal amikacin in chronic Pseudomonas aeruginosa lung infections. *J. Antimicrob. Chemother.* **61,** 859–868 (2008).

128. Study to Evaluate Arikace™ in CF Patients With Chronic Infection Due to Pseudomonas Aeruginosa - Full Text View - ClinicalTrials.gov. Available at: https://clinicaltrials.gov/ct2/show/NCT01315691?term=arikace&rank=4. (Accessed: 7th November 2016)

129. DiD' solid; DiIC18(5) solid (1,1'-Dioctadecyl-3,3,3',3'-Tetramethylindodicarbocyanine, 4-Chlorobenzenesulfonate Salt). Available at:

https://www.thermofisher.com/order/catalog/product/D7757?ICID=search-product. (Accessed: 6th November 2016)

130. Fluorescence Fundamentals. Available at: https://www.thermofisher.com/uk/en/home/references/molecular-probes-the-handbook/introduction-to-fluorescence-techniques.html. (Accessed: 13th December 2016)

131. Hamann, S. *et al. Measurement of Cell Volume Changes by Fluorescence Self-Quenching*. **12,** (2002).

132. Calcein Used for the fluorometric determination of calcium and EDTA titration of calcium in the presence of magnesium. | Sigma-Aldrich. Available at: http://www.sigmaaldrich.com/catalog/product/sigma/c0875?lang=en&region=BE. (Accessed: 6th December 2016)

133. Turkevich, J., Stevenson, P. C. & Hillier, J. A study of the nucleation and growth processes in the synthesis of colloidal gold. *Discuss. Faraday Soc.* **11,** 55–75 (1951).

134. Kimling, J. *et al.* Turkevich method for gold nanoparticle synthesis revisited. *J. Phys. Chem. B* **110,** 15700–15707 (2006).

135. Liposome Preparation | Avanti Polar Lipids. Available at: https://avantilipids.com/tech-support/liposome-preparation/. (Accessed: 12th December 2016)

136. Ultrasonication. Available at: http://www.rsc.org/publishing/journals/prospect/ontology.asp?id=CMO:0001708. (Accessed: 12th December 2016)

137. Romberg, B., Hennink, W. E. & Storm, G. Sheddable Coatings for Long-Circulating Nanoparticles. *Pharm. Res.* **25,** 55–71 (2008).

138. Centrifugation Basics. *Sigma-Aldrich* Available at: http://www.sigmaaldrich.com/technical-documents/articles/biofiles/centrifugation-basics.html. (Accessed: 13th October 2016)

139. Mori, S. & Barth, H. G. *Size Exclusion Chromatography*. (Springer Science & Business Media, 2013).

140. Sun, T., Chance, R. R., Graessley, W. W. & Lohse, D. J. A Study of the Separation Principle in Size Exclusion Chromatography. *Macromolecules* **37,** 4304–4312 (2004).

141. Kostanski, L. K., Keller, D. M. & Hamielec, A. E. Size-exclusion chromatography—a review of calibration methodologies. *J. Biochem. Biophys. Methods* **58,** 159–186 (2004).

142. Spin-columns for Liposome Purification. *liposomics.com* Available at: http://www.liposomics.com/catalog/item/8984969/10206254.htm. (Accessed: 26th October 2016)

143. Zetasizer Nano ZS zur Messung von Größe, Zetapotenzial, Proteinmobilität und für mikrorheologische Messungen. Available at: http://www.malvern.com/de/products/product-range/zetasizer-range/zetasizer-nano-range/zetasizer-nano-zs/. (Accessed: 5th December 2016)

144. Chu, B. Laser Light Scattering. *Annu. Rev. Phys. Chem.* **21,** 145–174 (1970).

145. Kholodenko, A. L. & Douglas, J. F. Generalized Stokes-Einstein equation for spherical particle suspensions. *Phys. Rev. E* **51,** 1081–1090 (1995).

146. Sathappa, M. & Alder, N. N. Ionization Properties of Phospholipids Determined by Zeta Potential Measurements. *Bio-Protoc.* **6,** (2016).

147. Kaszuba, M., Corbett, J., Watson, F. M. & Jones, A. High-concentration zeta potential measurements using light-scattering techniques. *Philos. Transact. A Math. Phys. Eng. Sci.* **368,** 4439–4451 (2010).

148. Braeckmans, K. *et al.* Sizing Nanomatter in Biological Fluids by Fluorescence Single Particle Tracking. *Nano Lett.* **10,** 4435–4442 (2010).

149. Braeckmans, K. Single particle tracking. (2010).

150. Röding, M., Deschout, H., Braeckmans, K. & Rudemo, M. Measuring absolute number concentrations of nanoparticles using single-particle tracking. *Phys. Rev. E* **84,** 31920 (2011).

151. Introduction to Fluorescence Microscopy. *Nikon's MicroscopyU* Available at: https://www.microscopyu.com/techniques/fluorescence/introduction-to-fluorescence-microscopy. (Accessed: 6th December 2016)

152. Introductory Confocal Concepts. *Nikon's MicroscopyU* Available at: https://www.microscopyu.com/techniques/confocal/introductory-confocal-concepts. (Accessed: 6th December 2016)

153. SYTO 9 Green Fluorescent Nucleic Acid Stain - Thermo Fisher Scientific. Available at: https://www.thermofisher.com/order/catalog/product/S34854. (Accessed: 20th October 2016)

154. Using a Dark Field Microscope - Its Uses in Microscopy and Advantages. *MicroscopeMaster* Available at: http://www.microscopemaster.com/dark-field-microscope.html. (Accessed: 14th December 2016)

155. Darkfield Illumination. *Nikon's MicroscopyU* Available at: https://www.microscopyu.com/techniques/stereomicroscopy/darkfield-illumination. (Accessed: 14th December 2016)

156. Assay: Hybrid Bridges the Microplate Reader Gap | GEN Genetic Engineering & Biotechnology News - Biotech from Bench to Business. *GEN* Available at: http://www.genengnews.com/gen-articles/assay-hybrid-bridges-the-microplate-reader-gap/2332. (Accessed: 15th May 2017)

157. Triton™ X-100 for electrophoresis | Sigma-Aldrich. Available at: http://www.sigmaaldrich.com/catalog/product/SIGMA/T8532?lang=en&region=BE. (Accessed: 14th December 2016)

158. Lichtenberg, D., Ahyayauch, H. & Goñi, F. M. The Mechanism of Detergent Solubilization of Lipid Bilayers. *Biophys. J.* **105,** 289–299 (2013).

159. Taylor, T. M., Gaysinsky, S., Davidson, P. M., Bruce, B. D. & Weiss, J. Characterization of Antimicrobial-bearing Liposomes by ζ-Potential, Vesicle Size, and Encapsulation Efficiency. *Food Biophys.* **2,** 1–9 (2007).

160. Were, L. M., Bruce, B. D., Davidson, P. M. & Weiss, J. Size, Stability, and Entrapment Efficiency of Phospholipid Nanocapsules Containing Polypeptide Antimicrobials. *J. Agric. Food Chem.* **51,** 8073–8079 (2003).

161. Roberts, K. E., O'Keeffe, A. K., Lloyd, C. J. & Clarke, D. J. Selective Dequenching by Photobleaching Increases Fluorescence Probe Visibility. *J. Fluoresc.* **13,** 513–517 (2003).

162. Colletier, J.-P., Chaize, B., Winterhalter, M. & Fournier, D. Protein encapsulation in liposomes: efficiency depends on interactions between protein and phospholipid bilayer. *BMC Biotechnol.* **2,** 9 (2002).

163. Kulkarni, S. B., Betageri, G. V. & Singh, M. Factors affecting microencapsulation of drugs in liposomes. *J. Microencapsul.* **12,** 229–246 (1995).

164. Costa, A. P., Xu, X. & Burgess, D. J. Freeze-anneal-thaw cycling of unilamellar liposomes: effect on encapsulation efficiency. *Pharm. Res.* **31,** 97–103 (2014).

8.4 Table of figures

8.5 Table of formulae

8.6 List of tables

8.7 Table of abbreviation

%	Percent
°	Degree
°C	Degree Celcius
µm	Micrometer
AN-CAL-high Au-lipo	DOPC/DPPG liposomes with Calcein and a high amount of Au-NPs encapsulated
AN-CAL-lipo	DOPC/DPPG liposomes with encapsulated calcein
AN-CAL-low Au-lipo	DOPC/DPPG liposomes with Calcein and a low amount of Au-NPs encapsulated
AN-HEP-Au-lipo	DOPC/DPPG rehydrated with HEPES and Au-NPs
AN-HEP-lipo	DOPC/DPPG rehydrated with HEPES
Au-C6SH	hexanethiol-coated gold nanoparticles
Au-MSA	mercaptosuccinic acid-coated gold nanoparticles
Au-NPs	Golden nanoparticles
bisSorbBPC	bis-sorbyl phosphatidylcholine
C8 PEG2000 ceramide	[N-octanoyl-sphingosine-1-[succinyl(methoxy(polyethylene glycol)2000)]
CAT-CAL-lipo-det	Calcein loaded DOTAP/DOPE liposomes for the detergent experiment
CAT-Cer-PEG-lipo	DOTAP/DOPE/DiD liposomes pegylated with C8 PEG2000 Ceramide
CAT-HEP-lipo-det	HEPES loaded DOTAP/DOPE liposomes for the detergent experiment
CAT-lipo	DOTAP/DOPE/DiD liposomes non pegylated
CAT-PEG-lipo	DOTAP/DOPE/DiD liposomes pegylated with DSPE-PEG2000
CFU	Colony forming unit
$CHCl_3$	Chloroform
Chol	Cholesterol
DC8,9,PC	1,2-bis(tricosa-10,12-diynoyl-sn-glycero-3-phosphocholine
DiD	1,1’ dioctadecyl-3,3,3’,3’-tetramethylindodicarbocyanine, 4-chlorobenzensulfonate salt
DLS	Dynamic Light Scattering
DMPG	1,2-dimyristoyl-sn-glycero-3-phospho-(1'-rac-glycerol) (sodium salt)
DOPC	1,2-dioleoyl-sn-glycero-3-phosphocholine
DOPE	1,2-dioleoyl-sn-glycero-3-phosphoethanolamine
DOTAP	1,2-dioleoyl-3-trimethylammonium-propane (chloride salt)]
DPPC	dipalmitoyl-sn-glycero-3-phosphocholine
DPPE-Nanogold®	1,4 nm golden nanoparticle attached to a dipalmitoyl-phosphatidyl-ethanolamine molecule
DPPG	1,2-dipalmitoyl-sn-glycero-3-phospho-(1'-rac-glycerol) (sodium salt)
DSPE-PEG 2000	,2-distearoyl-sn-glycero-3-phosphoethanolamine-N-[methoxy (polyethylene glycol)-2000](ammonium salt)
e.g.	Example given
EMCCD	electron multiplying charge coupled device
EPR-effect	Enhanced permeation and retention
HEPES	[N-(2-Hydroxyethyl)piperazine-N’-(2-ethanesulfonic acid)

LMV	large multilamellar vesicles
LNA-System	Liposomes-nanoparticle-assemble
LUV	large unilamellar vesicles
Max	Maximal
MBIC	Minimal biofilm inhibitory concentration
Min	Minutes
NEAR IR	Near infrared light
NEU-CAL-lip	Calcein loaded lDPPC/Chol liposomes
NEU-Cer-PEG-lipo	DPPC/Chol/DiD liposomes pegylated with C8 PEG2000 Ceramide
NEU-HEP-lipo	HEPES loaded DPPC/Chol liposomes
NEU-lipo	DPPC/Chol/DiD liposomes non pegylated
NEU-PEG-lipo	DPPC/Chol/DiD liposomes pegylated with DSPE-PEG 2000
NEU-TOBRA-lipo	Tobramycin loaded DPPC/Chol liposomes
Nm	Nanometer
NPs	Nanoparticles
Ns	Nanoseconds
PDI	Polydispersity Index
PEG	Polyetheylen glycole
PI	Phosphatidylinositol
polyNIPAM	poly-N-isopropylacrylamide
RES-System	Reticulo endothelial system
ROS	Reactive oxygen species
SPR	Surface-Plasmon- Resonance
SPT	Single particle tracking
SUV	small unilamellar vesicles
Tc	Gel-liquid crystal phase transition temperature
TEM	Transmission electron microscopy
TFH	Thin film hydration
TOBRA-lipo	DOPC/DPPG liposomes with Tobramycin encapsulated
VNB	Vapour nanobubble
VNBs	Vapour nanobubbles